Analysis of hippocampal inhibitory and excitatory neurons during sharp wave-associated ripple

Dissertation

zur Erlangung des akademischen Grades
doctor rerum naturalium
(Dr. rer. nat.)
im Fach Biologie
Spezialisierung: Neurobiologie

eingereicht an der
Lebenswissenschaftlichen Fakultät
der Humboldt-Universität zu Berlin

von
Frau M.Sc. Maria Pangalos

Präsidentin der Humboldt-Universität zu Berlin
Prof. Dr.-Ing. Dr. Sabine Kunst

Dekan der Lebenswissenschaftlichen Fakultät
Prof. Dr. Bernhard Grimm

Gutachter/innen:
1. Prof. Dr. Richard Kempter
2. Prof. Dr. Dietmar Schmitz
3. Prof. Dr. Nikolai Axmacher

Tag der mündlichen Prüfung: 20. Juli 2016

Abstract

In the hippocampus there are different patterns of activity also known as network oscillations. These oscillations express different frequencies, and one particularly fast oscillation is the ripple oscillation at around 200 Hz. It is associated with an activity wave called sharp wave and form a so-called sharp wave-ripple complex (SWR). SWRs are implicated in memory consolidation. In this thesis we investigate some of the mechanisms underlying sharp wave-ripple complexes.

In the first part of this thesis I examine one type of inhibitory interneurons in the region CA1 of the hippocampus during ripple oscillations. Oriens-lacunosum moleculare (O-LM) interneurons receive strong excitatory synaptic input during ripples. This input arrives after the ripple maximum and is phase locked with the ascending phase of ripple cycles. Around half of the probed O-LM neurons fire during the SWR and thereby show an active participation in this type of network activity (13 out of 22 tested cells). The magnitude of excitation in O-LM interneurons and the ratio between excitation and inhibition determine if an O-LM cell is active during the SWR. The action potentials in these cells occur late during the field oscillation and are phase locked.

In the second part of the thesis the synaptic input onto excitatory pyramidal cells were investigated during ripple oscillations. Previous work has identified two different types of pyramidal cells in area CA1. We recorded from deep and superficial pyramidal neurons whose locations are close to the stratum oriens, and close to the stratum radiatum, respectively. For both types of pyramidal neurons the inhibitory and excitatory synaptic inputs temporally associated with ripples express comparable strength.

In the last and third part, I recorded sharp wave-ripple complexes in the CA2 region of the hippocampus and showed incidence, frequency and amplitude of ripples and SWRs. Pyramidal cells in the CA2 region are integrated into the network during SWR. They receive SWR associated synaptic input during every SWR. The excitatory and inhibitory synaptic inputs in CA2 pyramidal neurons were investigated in detail. Phase analysis show phase locking of LFP ripples and synaptic inputs to the ascending phase of the ripple cycles.

Contents

Chapter 1

Introduction: The hippocampus, its cell types and hippocampal oscillations

1.1 The hippocampus

The hippocampus is a brain area that belongs to the hippocampal formation together with the dentate gyrus, subiculum, presubiculum, parasubiculum and entorhinal cortex. The hippocampus itself is also further subdivided in areas, the *cornu ammonis* (CA) CA1, CA2 and CA3 (Figure 1.1). These areas are connected with each other and also with the other parts of the hippocampal formation and other brain regions. The classical view of the connections is in parts under debate and is always changing with new studies and the development of new experimental methods. More or less established is that the entorhinal cortex (EC) projects via the perforant pathway to the dentate gyrus (DG) as well as to CA3 and CA1. Granule cells of the DG project via mossy fibers to the CA3 area, and CA3 sends its projections called "Schaffer collaterals" to CA1. Area CA1 projects to the subiculum and this is projecting back to the EC (Andersen et al., 2006).

The hippocampus can not only be subdivided along the transverse axis into CA1, CA2 and CA3, it also has a laminar structure. The cell bodies of the hippocampal principal cells are located in the pyramidal cell layer. The basal dendrites of the pyramidal cells in all areas extend in the stratum oriens (s.o.). In this layer there are also cell bodies, dendrites and axons of several interneuron classes. In all three areas of the cornu ammonis the apical dendrites of pyramidal cells extend over two strata containing also different interneurons. The proximal apical dendrites are in the stratum radiatum (s.r.) and the distal dendrites of pyramidal cells also reach the stratum lacunosum-moleculare (s.lm.). Stratum lacunosum-moleculare contains fibers that connect directly the EC and the hippocampus. Only in area CA3 there is an additional layer above the pyramidal cell layer called stratum lucidum (s.l.).

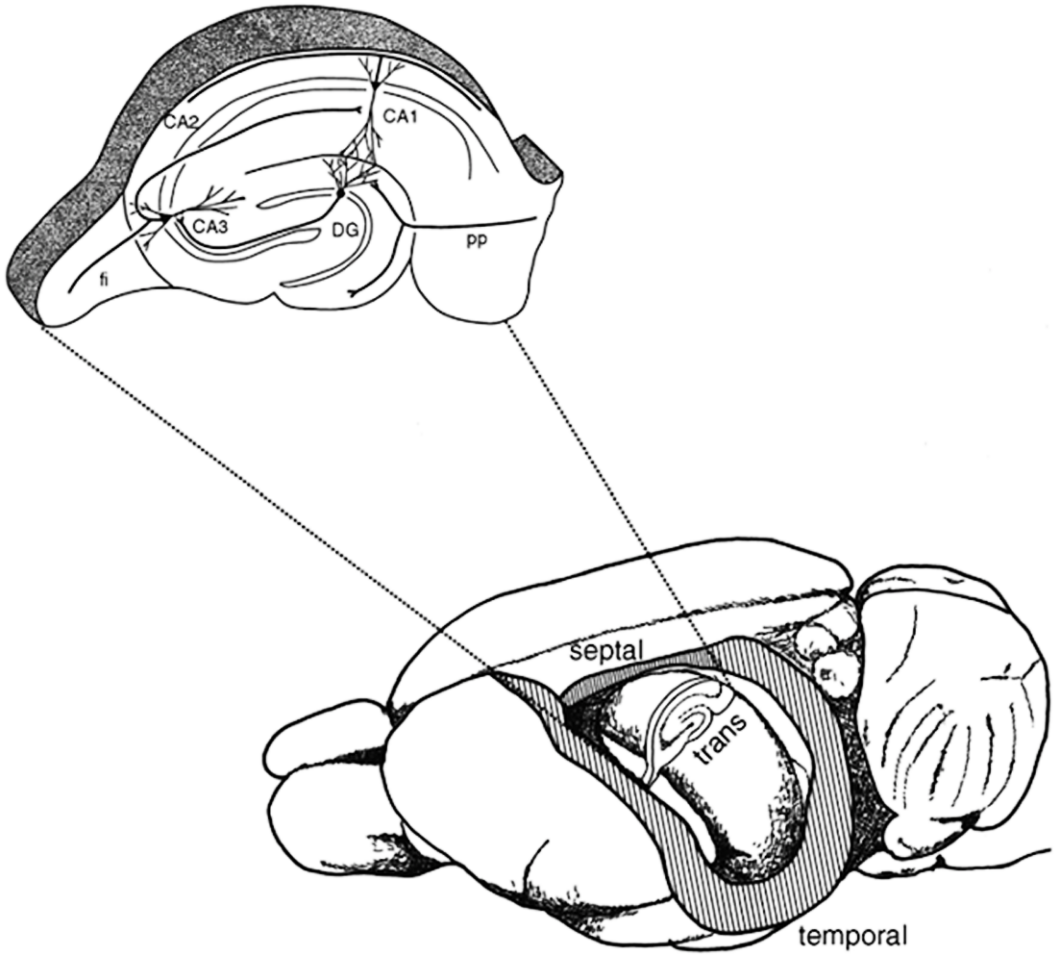

Figure 1.1 Line drawing of the rat brain shows the septotemporal and transvere axes of the hippocampal formation. (Figure and caption: Andersen et al., 2006)

In this layer there are mossy fibers from the dentate gyrus granule cells and mossy fiber-associated interneurons (Vida and Frotscher, 2000; Andersen et al., 2006).

1.2 Hippocampal cell types

The two main cells groups in the hippocampus proper are the principal cells and the interneurons. Pyramidal neurons are the principal cells in the hippocampus whose cell bodies are located mostly in the pyramidal cell layer. All pyramidal neurons provide glutamatergic output and they are subdivided into pyramidal cells of area CA1, CA2 and CA3. These pyramidal neurons differ in their anatomical and physiological properties and are differently integrated in the hippocampal network, receive different inputs and project to various different regions (see Chapter 4: Analysis of synaptic inputs in pyramidal neurons in area CA2 during SWRs). At least the CA1

pyramidal cells consist of further subclasses for example the superficial and deep CA1 pyramidal neurons (see Chapter 3: Comparison of synaptic input in deep and superficial CA1 pyramidal cells during ripple oscillations).

In comparison to the pyramidal neurons of the hippocampus the interneurons are divided in even more subclasses. In 1996 Freund and Buzsáki classified the different γ-aminobutyric acid-releasing (GABAergic) interneuron types by their innervation region. They differentiate (1) interneurons that innervate the axon initial segment of pyramidal neurons, (2) interneurons that innervate the cell bodies, (3) interneurons that innervate the apical and basal dendrites but not the cell body, (4) interneurons that innervate the more proximal apical dendrites with cell body and basal dendrites, (5) interneurons that innervate all parts of the pyramidal neuron in the stratum oriens, pyramidal cell layer and stratum radiatum or (6) interneurons innervating only the very distal apical dendrites in the stratum lacunosum moleculare (Freund and Buzsáki, 1996). Twelve years later, Klausberger and Somogyi summarized for the area CA1 at least 21 interneurons with a description of the location of the cell body and the innervation zone not only with regard to pyramidal neurons but also to other interneurons (Figure 1.2, Klausberger and Somogyi, 2008). Interneurons were classified by their anatomical properties and by their innervation areas. An additional property used for classification is the expression of different neuropeptides or calcium binding proteins in interneurons. Neuropeptides are stored in dense-core vesicles, can be released from axons or dendrites and can modulate neuronal activity (Baraban and Tallent, 2004). As calcium is an important factor in the signal transduction, calcium binding proteins can influence synaptic transmission and plasticity. Prominent examples for interneuronal neuropeptides are somatostatin (SOM), cholecystokinin (CCK), vasoactive intestinal polypeptide (VIP), neuropeptide Y (NPY), enkephalins and substance P (SP). Calcium binding proteins used for classifications are parvalbumin (PV), calbindin D28k (CB) and calretinin (CR) (Freund and Buzsáki, 1996). There are antibodies to the neuropeptides and calcium binding proteins which are used in immunostainings and help to classify the interneurons.

In the following, some types of important interneurons are described in detail. One type of hippocampal interneurons are the basket cells. Their cell body is located close to or in the pyramidal cell layer (McBain et al., 1994), the apical dendrites extend to the stratum radiatum and stratum lacunosum-moleculare and the basal dendrites to the stratum oriens reaching the alveus. The axon of basket cells ramifies in the entire depth of the pyramidal cell layer and proximal stratum oriens and contacts the soma and proximal dendrites of pyramidal cells. These synapses form complex arrays with a basket like shape (Freund and Buzsáki, 1996; Freund and Katona, 2007). In addition, one basket cell forms synapses with 1000-2000 pyramidal cells (Freund, 2003). Basket cells are divided into two types, one containing the calcium binding protein parvalbumin, the other type is immunoreactive for the neuropeptide CCK (Freund, 2003). Parvalbumin-positive basket cells (PVBCs) differ from CCK containing basket cells in their electrophysiological features. PVBCs are fast-spiking cells with firing frequencies above 100 Hz whereby CCK containing bas-

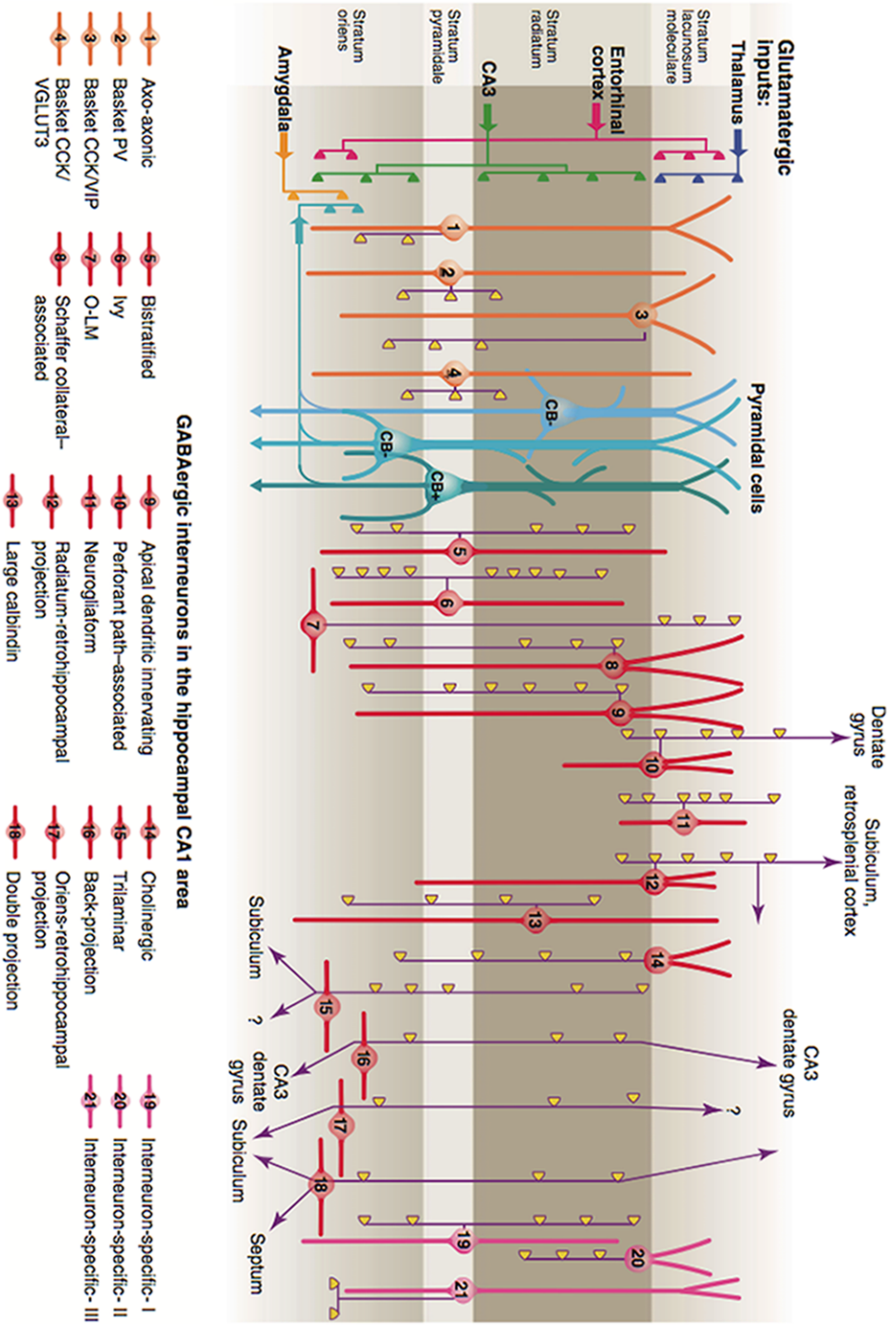

Figure 1.2 Three types of pyramidal cell are accompanied by at least 21 classes of interneuron in the hippocampal CA1 area. The main termination of five glutamatergic inputs are indicated on the left. The somata and dendrites of interneurons innervating pyramidal cells (blue) are orange, and those innervating mainly other interneurons are pink. Axons are purple; the main synaptic terminations are yellow. Note the association of the output synapses of different interneuron types with the perisomatic region (left) and either the Schaffer collateral/commissural or the entorhinal pathway termination zones (right), respectively. VIP, vasoactive intestinal polypeptide; VGLUT, vesicular glutamate transporter; O-LM, oriens lacunosum moleculare. (Figure and caption: Klausberger and Somogyi, 2008)

ket cells fire regular with much lower frequencies (Freund, 2003). PVBCs are highly active and fire phase locked to the hippocampal rhythms theta, gamma, epsilon and ripple oscillations (Varga et al., 2012). PVBCs have the function of an oscillator and are important for different oscillations involved in memory formation. However, the CCK containing basket cells carry information about motivation, emotions and the autonomic state of the animal (Freund and Katona, 2007). PVBCs are activated via Schaffer collaterals and provide feed-forward inhibition to CA1 pyramidal neurons. Whereas only summation of inputs from CA3 and CA1 pyramidal neurons but not inputs via Schaffer collaterals alone result in action potential firing of CCK containing basket cells. These cells thereby provide feed-back inhibition to CA1 pyramidal neurons (Glickfeld and Scanziani, 2006).

Another interneuron type in the hippocampus are the bistratified cells. Dendrites and cell body of this cell type is located in the stratum oriens. The axons build synapses with the basal and apical dendrites of pyramidal cells mainly in stratum oriens and stratum radiatum where also the input via Schaffer collaterals arrives. In addition, there is also very few axon in the pyramidal cell layer (Buhl et al., 1994; Maccaferri et al., 2000; Maccaferri, 2005). The neuropeptide somatostatin is expressed in bistratified cells but also in other interneurons in stratum oriens wherefore it can not act as an identification property alone (Maccaferri, 2005). Bistratified interneurons receive input by the Schaffer collaterals and therefore provide feed-forward inhibition to CA1 pyramidal neurons (Buhl et al., 1994). Bistratified cells are very active and fire phase locked during theta, gamma and ripple oscillations (Klausberger et al., 2003). There are at least two types of bistratified cells, the oriens-bistratified cells (O-BiCs) have dendrites which are located in the stratum oriens and alveus and have a horizontal orientation. The other type is only called bistratified cells and these cells differ in terms of their dendritic orientation. The dendrites of the bistratified cells have a radial orientation whereby the axons of both types of bistratified cells are comparable (Maccaferri et al., 2000).

An interneuron type in the hippocampus which innervates also the dendrites of pyramidal neurons but the very distal parts of the dendrites in stratum lacunosum moleculare are the oriens-lacunosum moleculare (O-LM) interneurons (McBain et al., 1994; Sik et al., 1995; Maccaferri and McBain, 1996; Ali and Thomson, 1998; Katona et al., 1999; Maccaferri et al., 2000; Martina et al., 2000). O-LM interneurons have a characteristic morphology: their cell bodies as well as their horizontally orientated dendrites are located in the stratum oriens and partially stratum alveus. The axon arises from the soma or from one of the dendrites, passes through the stratum pyramidale, the stratum radiatum and branches mainly in the stratum lacunosum moleculare (McBain et al., 1994; Sik et al., 1995; Maccaferri and McBain, 1996; Ali and Thomson, 1998; Katona et al., 1999; Maccaferri et al., 2000; Martina et al., 2000). O-LM interneurons belong to the group of somatostatin positive interneurons (Katona et al., 1999). Upon sufficient hyperpolarization they show a prominent sag potential and a saw tooth-like firing pattern upon depolarization (Maccaferri and McBain, 1996). O-LM cells receive the main excitatory input from surrounding CA1 pyramidal neurons (Sik et al., 1995). Inhibitory input to O-LM

neurons is provided by one type of a vasoactive intestinal polypeptide (VIP) expressing interneuron, by type I GABAergic septohippocampal neurons and also by O-LM cells themselves (Acsády et al., 1996; Gulyás et al., 1990; Kogo et al., 2004; Leão et al., 2012). Receiving excitatory inputs from CA1 pyramidal cells and also innervating distal dendrites of these pyramidal cells give O-LM cells a function to provide feed-back inhibition. High activity of surrounding pyramidal cells leads to a strong activation of O-LM neurons and results in the inhibition of distal dendrites and thereby in a reduced direct input from the entorhinal cortex to CA1 pyramidal neurons (Katona et al., 1999; Leão et al., 2012).

1.3 Hippocampal oscillations

In the hippocampus there are different rhythmic activity patterns called hippocampal oscillations depending on the behavioral state (Buzsáki, 1986; Buzsáki and Draguhn, 2004). These oscillations are classified due to their frequency into theta (4-10 Hz), gamma (30-100 Hz) and ripple oscillations (100-250 Hz). Theta oscillation occur during movement such as walking, rearing and jumping (Vanderwolf, 1969). Gamma oscillations can occur together with theta oscillations or alone (Csicsvari et al., 2003). Ripple oscillations occur together with sharp waves (SPWs), which last for 40-120 ms, and were first observed during network states where no theta was detected (Buzsáki, 1989; Buzsáki et al., 1992). SPWs occur during slow-wave sleep, motionless awake state, drinking, face washing, fur grooming and eating (Figure 1.3, Buzsáki, 1986).

SPWs recorded from stratum radiatum express a large negative amplitude. In the pyramidal cell layer and the stratum oriens the SPWs are of positive polarity. These different polarities can be explained by sinks and sources of underlying currents. The depolarization of the dendrites in stratum radiatum by the Schaffer collaterals form the sink, which is reflected by the negative polarity of the SPW in the local field potential. The related source in the pyramidal cell layer is the reason for the positive SPW polarity. SPWs probably originate in area CA3 and then propagate to CA1 (Buzsáki, 1986; Buzsáki et al., 1992). In the two hippocampi the SPWs and associated ripple (sharp wave-ripple complex, SWR) occur simultaneously but the ripple oscillation in area CA1 of both sides are not correlated, indicating the local generation of ripples in CA1 (Buzsáki et al., 1992; Maier et al., 2011).

The firing of CA1 pyramidal cells during SPW associated ripples is time locked to the ripple oscillation. The excitatory drive is provided by CA3 pyramidal cells and responsible for the timing of pyramidal cell firing in CA1 is rhythmic and coherent activity of interneurons in CA1 (Ylinen et al., 1995).

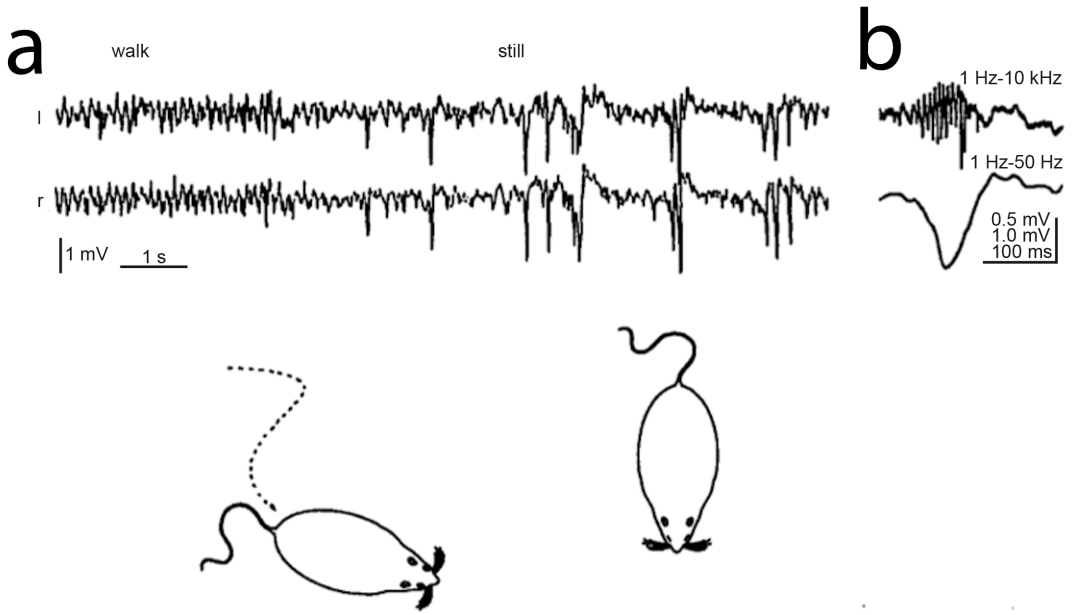

Figure 1.3 Bahavior-dependent macroscopic (EEG) states in the hippocampus. **(*a*)** Extracellular recordings from the CA1 stratum radiatum of the left (l) and right (r) hippocampus during the transition from exploration (walk) to being still (still). Note regular theta waves during walking and large, negative SPWs during immobility. Note also that SPWs are bilaterally synchronous. **(*b*)** A single SPW with simultaneously recorded fast field oscillation from the CA1 pyramidal layer at a faster time scale. (Adapted after Buzsáki, 1996).

1.3.1 Sharp wave-ripple complexes are implicated in memory consolidation

SWRs are thought to be implicated in the consolidation of memory. One theory described in a review by Buzsaki (1989) proposes a two-stage model of memory formation. In the first stage only a labile form of memory is produced due to weak and transient potentiation of CA3 pyramidal neurons during theta oscillations. During the second stage in which SWRs occur the formation of long lasting memory takes place. Due to the high spike frequency during population bursts in CA3 long term potentiation (LTP) is formed in some CA3 and CA1 pyramidal neurons (Buzsáki, 1989). This relatively vague theory was further strengthened and expanded. If an animal explores a room there are cells in the hippocampus firing only at a special place, the place cells (O'Keefe, 1976). If the place cells are active during a behavior task, these cells also fire during sleep and SWRs after the task (Wilson and McNaughton, 1994; Lee and Wilson, 2002). Furthermore, if several place cells are activated after each other during a behavior task then these cells fire in a temporally reversed order during ripple oscillations immediately after the task (Foster and Wilson, 2006; Diba and Buzsáki, 2007). During SWRs shortly before a run the place cells fire in a forward order (Diba and Buzsáki, 2007).

The consolidation of memory affects not only the hippocampus itself. Pyramidal cells in CA1 have several projections to other brain regions. It was shown that

during SPW in the hippocampus there is also an increase in activity in deep layer V-VI of the entorhinal cortex, the parasubiculum, presubiculum and subiculum indicating that information is transferred to these areas during SWRs (Chrobak and Buzsáki, 1994). Besides these structures also other brain regions like the ventral striatum (implicated in guidance of consummatory and conditioned behavior) and the medial prefrontal cortex (implicated in long-term memory consolidation of spatial and contextual information) are involved in the memory consolidation based on SWRs in the hippocampus (Pennartz et al., 2004; Lansink et al., 2009; Peyrache et al., 2009; O'Neill et al., 2010). There are also interneuron types with long-range projections from the hippocampus to other brain regions. And some of these interneurons are active during SWRs and therefore able to transfer information from the hippocampus to other brain regions (Jinno et al., 2007).

Besides the consolidation of memory regarding spatial memory SWRs, the hippocampus seems also to be implicated in the consolidation of reference or working memory and associative memory as the ripple magnitude increases following training tasks concerning these types of memory (Ponomarenko et al., 2008; Eschenko et al., 2008; Ramadan et al., 2009).

In humans, equivalents to SWRs could be identified (Bragin et al., 1999) and it was shown that rhinal ripple oscillations increase their incidence after a learning task (Axmacher et al., 2008).

In addition, in studies where the authors interrupted the SWRs after a behavioral learning session the learning was impaired if they interrupted SWRs during sleep and if they only interrupted awake SWRs (Ego-Stengel and Wilson, 2010; Girardeau et al., 2009; Jadhav et al., 2012).

1.3.2 Theoretical models of hippocampal ripple oscillations

There are different approaches to theoretically model the hippocampal network during ripple oscillations. One idea of hippocampal ripples is based on axonal gap junctions between pyramidal cells (Draguhn et al., 1998; Traub et al., 1999). In this model already very few gap junctions between pyramidal cell axons are sufficient to produce high-frequency synchronized oscillations in randomly connected networks with a frequency in the ripple band. Assumptions in this model are the spontaneous occurrence of ectopic spikes with a low frequency and the ability of gap junctions to transfer an action potential from one axon to the neighboring (Traub et al., 1999). The model was further developed and included also somatic firing at sparse frequencies additional to the high frequency axonal spiking durning SWRs. Also gamma oscillations could be induced by including phasic synaptic inhibition in the axonal region where also the gap junctions are located. Again somatic spikes are much less often observed in the pyramidal cells than axonal spikes. During the gamma oscillation and the ripple oscillation the same group of pyramidal neurons fire. This is consistent with the situation *in vivo* (Traub et al., 2012).

Another model is also based on pyramidal cells as the origin of the ripple oscillation

however, this model is based on supralinear dendritic integration in a recurrent pyramidal cell network. Supralinear dendritic amplification results in a depolarization of the soma with high temporal precision that allows synchronisation of pyramidal cells at ripple frequency (Memmesheimer, 2010).

Both, the first and second type of models described above are based on pyramidal cells as the generator of the ripple which secondarily recruit the interneuron network ('excitation first models'). An alternative group of models has been put forward that assume a network of inhibitory interneurons that is crucial for the generation of ripple oscillations. Stimulation of the interneurons leads to reciprocal inhibition and activity of the interneurons in the ripple frequency band, giving rise to rhythmic inhibition of target pyramidal cells. In these models, the interneurons are the pacemaker ('inhibition first models') (Buzsáki et al., 1992; Ylinen et al., 1995; Brunel and Wang, 2003; Schlingloff et al., 2014).

1.3.3 Role of interneurons during hippocampal oscillations

As already indicated, GABAergic interneurons are able to synchronize the pyramidal cell firing during network oscillations and there are several studies reinforcing this property of interneurons. Already a single interneuron is able to act as a pacemaker for many pyramidal neurons. Cobb et al. could show that an individual interneuron could affect the spiking of pyramidal neurons so that they fire at theta frequency (Cobb et al., 1995). Another study could show the dependence of pyramidal cell firing during theta oscillations on a special type of interneurons. Selective block of activity of parvalbumin positive interneurons resulted in a phase shift of population bursts of pyramidal neurons (Royer et al., 2012). Cortical activity at gamma frequencies is also shown to be synchronized by GABAergic interneurons (Tamás et al., 2000). Finally, in a modeling study that used realistic data regarding synaptic properties, network structure and electrical coupling collected in slice recordings, showed that it is possible to generate oscillatory activity in a large range of frequencies from 20 to 110 Hz (Bartos et al., 2002).

Different interneuron types are more or less active or silent during theta, gamma or ripple oscillations. During one type of oscillation different interneuron types fire at different phases, but all interneurons of the same type fire mainly at the same phase. Different regions of the pyramidal cell, the cell body and the different parts of the dendrites, are innervated by different interneurons (see above). Since different interneurons are active during different phases of an oscillation, they will provide inhibitory input in different pyramidal cell compartments at distinct time points. Consequently, during different types of oscillations, theta, gamma or ripple oscillations and different behavioral states, interneurons are able to determine the activity of pyramidal neurons both in a compartmentalized, and in a temporal manner. During ripple oscillations pyramidal cells increase their firing rate and they fire with the largest probability at the negative peaks of the field ripple (Csicsvari et al., 1999; Klausberger et al., 2003, 2004; Hájos et al., 2004; Klausberger et al., 2005; Oren et al., 2006; Wulff et al., 2009; Gulyás et al., 2010).

During SWRs the interneuron types which undergo the largest positive modulation are the parvalbumin positive basket cells and bistratified interneurons. Both types of interneurons increase their firing rate during ripple oscillations and both fire simultaneously during the early ascending phase of the ripple cycles. PVBCs as well as bistratified cells are also very active during theta oscillations whereas during this oscillation they do not increase their firing probability simultaneously. PVBCs fire with largest probability during the peak and early descending phase and bistratified interneurons fire mostly during the trough of the theta oscillation cycle (Klausberger et al., 2003, 2004; Lapray et al., 2012; Varga et al., 2012; Forro et al., 2013).

There are types of interneurons which are not modulated during ripple oscillations. For example ivy interneurons which build synapses with the basal and oblique dendrites of pyramidal cells do not change their firing rates during SWRs. They fire with a stable firing probability independent of the oscillation type (Lapray et al., 2012; Fuentealba et al., 2008). In addition, other interneuron types are negatively modulated with SWRs. Axo-axonic cells form synapses with and around the axon initial segment. These interneurons fire only before and after the ripple oscillation but they stop firing during the SWR (Klausberger et al., 2003; Forro et al., 2013; Viney et al., 2013).

1.4 Aims of this work

I am interested in the mechanisms underlying ripple oscillations and an *in vitro* model of SWRs was used to study the synaptic and suprathreshold involvement of different cell types in different areas in the hippocampus.

1.4.1 O-LM interneurons in area CA1

In Chapter 2 (Recruitment of oriens-lacunosum moleculare interneurons during hippocampal ripples) the integration of O-LM cells into the network during SWRs were investigated. I was interested if there are postsynaptic currents in the O-LM neurons associated with the ripple oscillation in the field, called compound postsynaptic current (cPSC). The analysis of this cPSCs would give an indication, if O-LM cells are integrated into the network during SWRs and the sub- and suprathreshold involvement of these interneurons were then investigated in detail.

1.4.2 Deep and superficial pyramidal cells in CA1

It is known that deep and superficial pyramidal cells receive different strength of inhibition at least from one type of interneurons. Parvalbumin positive basket cells inhibit deep pyramidal cells about three times stronger then pyramidal neurons of the superficial layer (Lee et al., 2014). In Chapter 3 (Comparison of synaptic input in deep and superficial CA1 pyramidal cells during ripple oscillations) the synaptic

involvement of deep and superficial pyramidal neurons during ripple oscillation were investigated. The *in vitro* model of SWRs allows to study the effects of different inhibitory inputs from PVBCs into the two types of pyramidal neurons in CA1 in a context where also the other inhibitory inputs from other GABAergic interneurons and also excitatory inputs are taken into account.

1.4.3 How are pyramidal cells in CA2 integrated in SWRs?

The area CA2 of the hippocampus is located between the CA1 and CA3 region. The afferent projections and inputs into this region differ from those in the CA1 area (see above). I was interested in SWRs in CA2. In Chapter 4 (Analysis of synaptic inputs in pyramidal neurons in area CA2 during SWRs) the SWRs recorded in area CA2 were investigated and furthermore the synaptic integration of CA2 pyramidal neurons during ripple oscillation was investigated.

1.5 The *in vitro* model of sharp wave-ripple complexes

All our work is based on the robust and reliable *in vitro* model of SWRs. Maier et al. established this model, which offers a simple tool to investigate many mechanisms of ripple oscillations in a targeted manner (Maier et al., 2009). The model can be used to study synaptic involvement of all different cell types during ripple oscillations in the hippocampus. The influence of different drugs on the SWRs and neurons underlying the oscillation can be studied since it is easy to add substances to the system and also to wash them out. In addition, several manipulations of the network are possible with electric stimulations or with optogenetic approaches. However, the slice is a reduced system lacking the inputs from other regions of the brain and without neuromodulating processes, and obviously, there is no correlated behavior influencing network states and brain activity.

On the other hand, several tested parameters of SWRs like the laminar profile, the reversal of the peak of the extracellular recorded SPW and the frequency of the ripple are comparable with SWRs recorded *in vivo*. Altogether, the in vitro model of SWRs has been found to be a useful tool to study mechanisms intrinsic to the hippocampus that give rise to the spontaneous generation of sharp waves and ripples.

Chapter 2

Recruitment of oriens-lacunosum moleculare interneurons during hippocampal ripples

2.1 O-LM interneurons receive excitatory input during SWR

The initial motivation to study and analyze inputs in O-LM cells during SWRs was based on previous observations by Klausberger and colleagues. In *in vivo* juxtacellular recordings from interneurons in CA1 in anesthetized rats they observed a reduction of spike probability of O-LM neurons during ripple oscillations (Klausberger et al., 2003). Since pyramidal neurons receive ripple-coherent excitation and fire phase locked to the recorded local field potential (LFP) ripple (Ylinen et al., 1995; Maier et al., 2011) we were interested in the underlying synaptic currents in O-LM cells in comparison to pyramidal neurons. The results presented in the following chapter are summerized in Pangalos et al., 2013[1].

We recorded from interneurons in stratum oriens and filled the cells with biocytin to be able to stain the cells post-hoc. We only included cells into the analysis that showed morphological characteristics of O-LM cells. A reconstructed O-LM cell is shown in Figure 2.1 (A), with the cell body and dendrites in stratum oriens and an axon arising from one of the dendrites and branches in the stratum lacunosum moleculare. This O-LM neuron shows also the characteristic physiological properties like the "saw-tooth" firing pattern upon depolarization and a sag potential upon hyperpolarization. Across recordings, the LFP was always recorded nearby the cell in the stratum pyramidale with a maximum distance of 146 µm between the tips of the LFP and the patch electrode.

Figure 2.1 (B) represents the simultaneous LFP and O-LM whole-cell recording. It shows the SWR events in the LFP and the ripple component in the band-pass

[1]In appendix A there is a statement of contribution regarding this and the following chapters

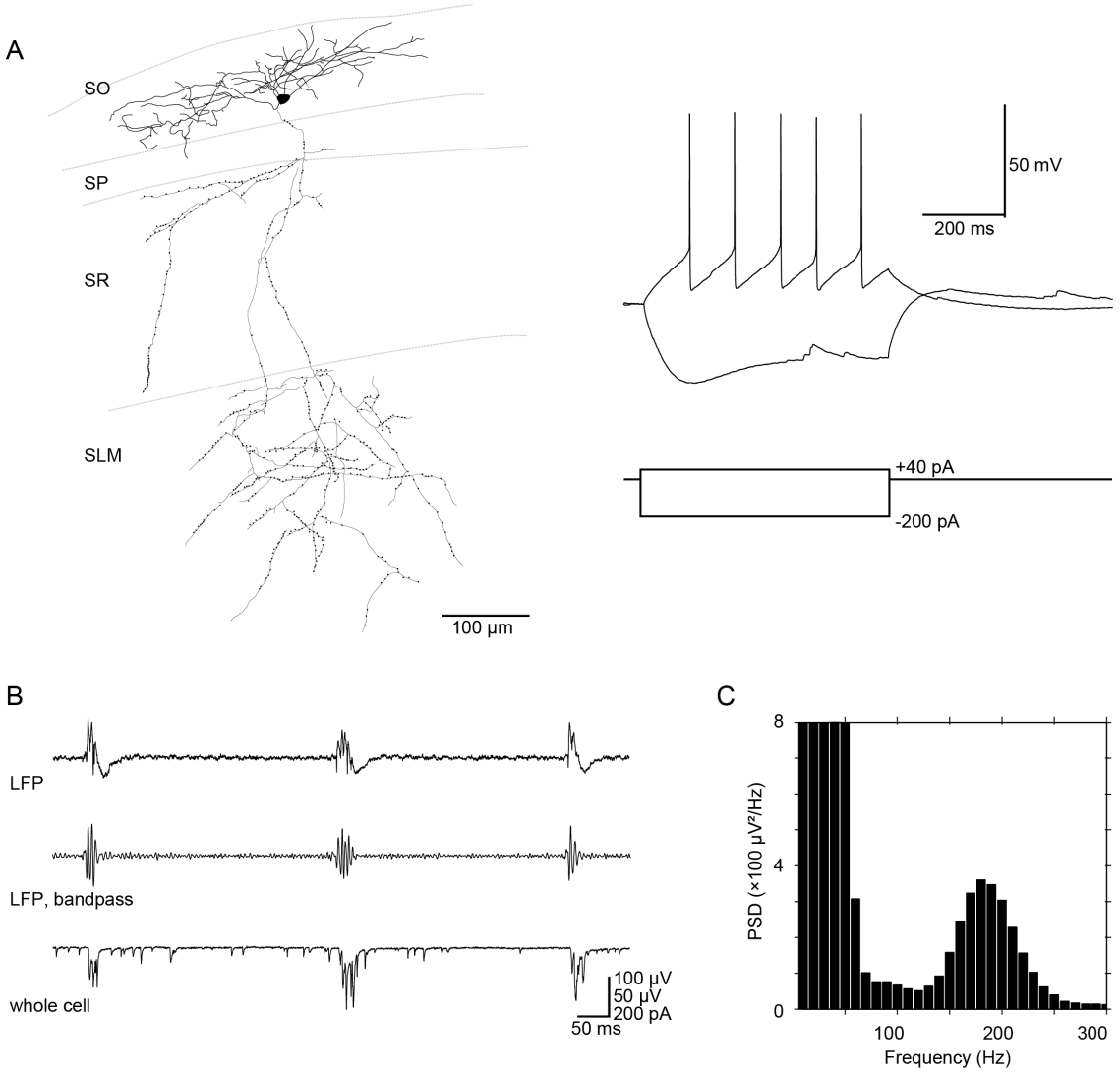

Figure 2.1 Ripple-associated synaptic input onto an O-LM neuron. **(*A*)** Reconstruction of an O-LM neuron recorded in area CA1. *Right*: Electrophysiological characterization of the depicted neuron; note the characteristic "sag potential" in response to hyperpolarization and the typical "saw-tooth" shape of action-potential afterhyperpolarizations. De- and hyperpolarizing current steps as indicated. SO: stratum oriens; SP: stratum pyramidale; SR: stratum radiatum; SLM: stratum lacunosum-moleculare. **(*B*)** Local field potential (LFP) recording in area CA1 demonstrating spontaneous occurrence of sharp waves (*top*) and associated ripples (*middle*, 127-300 Hz band-pass filtered version of the above). *Bottom*: voltage-clamp recording of an O-LM neuron (∼-60 mV) demonstrating compound postsynaptic currents associated with SWRs. **(*C*)** Power spectral density (PSD) of 57 LFP events from the recording presented in (*B*); frequency bin width: 10 Hz. Note the peak at ∼200 Hz indicating ripple frequency in the LFP signal.

filtered LFP. The O-LM cell shown in Figure 2.1 (A) receives complex synaptic input (compound postsynaptic currents, cPSCs) simultaneous to every SWR. This unexpected and strong modulation and integration in the network of O-LM neurons during the ripple oscillation is in contrast to the results by Klausberger (2003). The ripple frequency was around 200 Hz and also the spectral analysis of the SWRs recorded in the field showed a peak in this frequency range (Figure 2.1 (C)). To directly and simultaneously compare the cPSCs into pyramidal neurons and O-LM

cells, simultaneous dual whole-cell and LFP recordings were performed with a holding potential where the recording of excitatory as well as inhibitory currents in both types of neurons was feasible (∼-60 mV, all potentials are liquid junction corrected). Figure 2.2 (A) reveals the reconstruction and the spike pattern of a pyramidal and

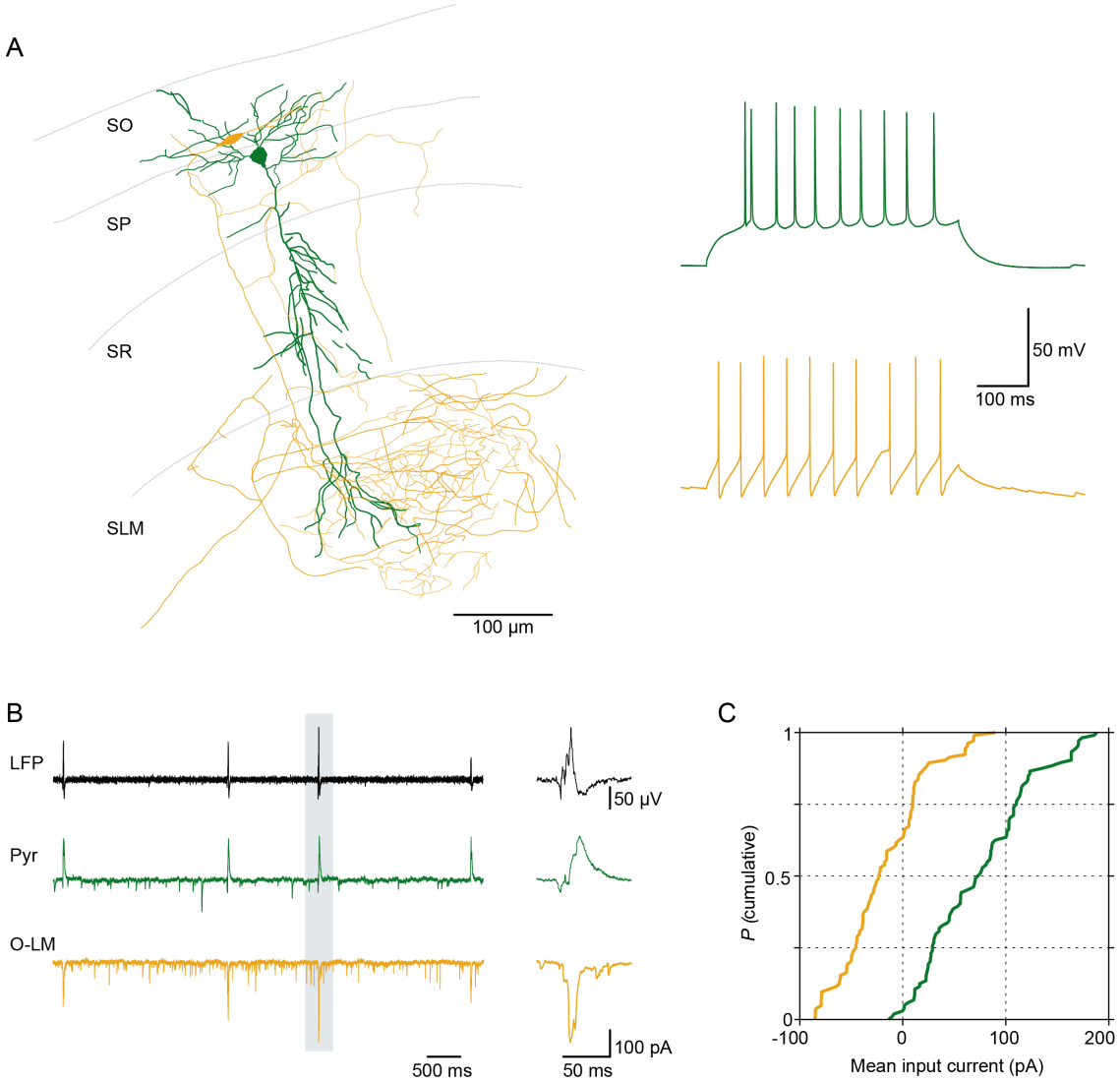

Figure 2.2 Ripple-associated synaptic input onto O-LM and pyramidal neurons. **(*A*)** *Left*: Reconstruction of an O-LM neuron (orange) and a principal cell (green) in area CA1 from a parallel recording. *Right*: Discharge patterns of the displayed cells. **(*B*)** Simultaneous LFP and whole-cell voltage-clamp recordings at a slightly depolarized potential (∼-60 mV) unmasks inhibitory (outward) currents in the pyramidal neuron while currents in the O-LM cell remain largely inward (excitatory). *Right*: magnification the indicated period. **(*C*)** Population analysis of average synaptic input current in pyramidal- and O-LM neurons (15 randomly picked events from seven pyramidal- and seven O-LM neurons). On average, O-LM neurons display consistently larger ripple-associated inward currents compared to pyramids ($P = 1.5\times10^{-26}$, K-S test). Quartiles for the distribution of input onto O-LM cells (orange): Median: -23.2 pA, P25: -47.6 pA, P75: +9.7 pA; for pyramidal cells (green): Median: +72.8 pA, P25: +28.8 pA, P75: +110.3 pA.

an O-LM cell recorded at the same time. The cPSCs recorded in the pyramidal cell mostly showed a small excitatory component followed by a larger inhibitory outward current. In contrast, the O-LM neuron received almost exclusively an excitatory in-

ward current (Figure 2.2 (B)). We calculated the input into seven O-LM and seven pyramidal cells (see 7.5 Data analysis) and Figure 2.2 (C) represents the cumulative distribution of both cell types, whereby 15 events from each cell were randomly picked. This direct comparison shows that O-LM cells compared with pyramidal cells receive stronger excitation ($P = 1.5\times10^{-26}$; Kolmogorov-Smirnov (K-S) test).

2.2 Analysis of excitatory input in O-LM cells

We observed that O-LM interneurons receive input associated with every SWR complex and that this input has a strong excitatory component. We therefore were interested to further investigate this input. To avoid the contribution of inhibitory currents to the cPSCs, we determined the reversal potential for chloride in CA1 O-LM cells and recorded these cells at -74 mV, because at this potential the net flow of chloride ions over the cell membrane is around zero as determined experimentally (7.5 Data analysis). We were interested to quantify the timing of the compound excitatory postsynaptic currents (cEPSCs) with respect to the field ripple. As the amplitude and polarity of the synaptic current does not matter for this analysis, we rectified the currents and did the further analysis on the resulting conductances. The LFP as well as the conductance were band-pass filtered (127-300 Hz) to isolate the ripple frequency component and with the Hilbert transformation the ripple envelope was calculated (Figure 2.3 (A1) and (A2)) (7.5 Data analysis). The LFP- and conductance ripple envelopes of the pooled data of all cells and events are shown in Figure 2.3 (B left). We observed that the mean envelope of the field ripple has its maximum 3.3 ± 0.3 ms prior to the maximum of the mean ripple envelope of the excitatory conductances in O-LM neurons. In all but one of the recorded O-LM neurons we noted that the field leads the conductance (Figure 2.3 (B Right), n = 27 parallel O-LM neurons and LFP recordings, 1791 events were analyzed).

Another relevant parameter of cPSCs besides the maximum of the ripple envelope is the phase, and therefore we analyzed the phase relationship between LFP ripple and the ripple of the synaptic input (7.5 Data analysis). We observed a strong phase locking of the conductance to the early ascending phase of the LFP ripple (Figure 2.3 (C), across cells, phases ranged between 152° and 284°, average: 209° ± 6°).

Due to variability in the estimated reversal potential for chloride between single cells and to exclude a possible contribution of inhibitory currents to the recorded ripple-associated cEPSCs (Figure 7.2), we decided to perform control experiments where we blocked chloride channels intracellularly with the Cl^- channel blocker disodium 4,4'-diisothio-cyanatostilbene-2,2'disulfonate (DIDS) in a cesium fluoride based intracellular solution (CsF-DIDS). First, to confirm that DIDS blocks inhibitory currents in O-LM cells, we patched O-LM neurons with a control intracellular solution and stimulated extracellularly to evoke inhibitory postsynaptic currents (IPSCs) in the O-LM cells. After this control recording we removed the patch pipette carefully from the cell so that the cell membrane resealed. This procedure was followed

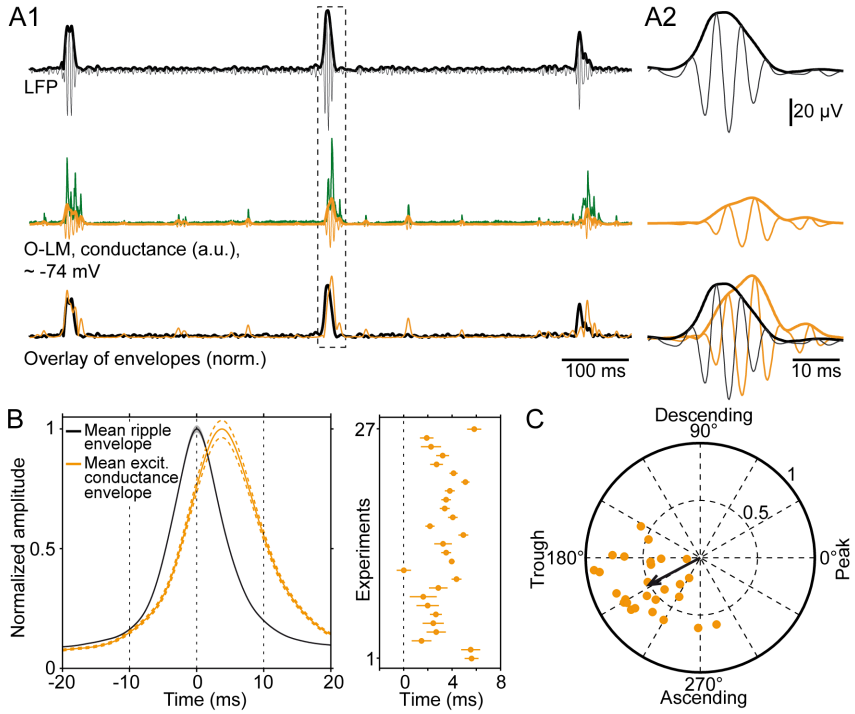

Figure 2.3 Synaptic input onto O-LM cells is coherent with ripples. **(*A*)** Illustration of the analysis. (*A1*) *Top*: ripple (127-300 Hz band-pass filtered LFP, black) overlaid with the envelope (black, bold) derived from the Hilbert transform. *Middle*: input conductance (green), its band-pass filtered version (orange) and the corresponding Hilbert envelope (orange, bold). *Bottom*: overlay of normalized envelopes of LFP and excitatory conductances. (*A2*) Magnification of the highlighted period. **(*B*)** *Left* Average envelopes of ripples (black) and excitatory conductances (orange) of 27 cells. The average excitatory input conductance in O-LM neurons lags behind the field ripples by 3.3 ± 0.3 ms. *Right* The orange dots represent the time points of conductance envelope peaks for all 27 cells (range: 0 ms to 5.8 ms). **(*C*)** Phases of excitatory conductances with respect to LFP ripples for 27 O-LM cells; orange dots represent the strength and phase of single-cell vectors (black circles and numbers, vector strength scaling; average vector: 208° with a vector strength of 0.51). Across cells, the analysis reveals a strong locking to early ascending ripple phases (mean phase estimation error: 27.1 ± 1.5°; see 7.5 Data analysis).

by a repatch of the same cell with a CsF-DIDS containing intracellular solution and recorded further stimulus evoked IPSCs. After 10 min the IPSCs were largely blocked (Figure 2.4 (A1) and (A2), IPSC reduction to 13.1 ± 3.6% P = 0.008, rank-sum test) confirming that we have minimized the impact of inhibitory conductances. We then applied this approach in recordings with SWR: we first recorded the LFP simultaneously with an O-LM cell. The O-LM cell was recorded with the control intracellular solution and the patch electrode was gently removed after at least 3 min of recordings. Then, a repatch of the cell with the DIDS containing solution was performed. We observed cEPSCs in the control condition as well as in the repatch with CsF-DIDS after 10 min perfusion (Figure 2.4 (B1) and (B2)). The delay of the conductance with respect to the field of around 3 ms could be observed both in the control and the CsF-DIDS condition (Figure 2.4 (C), n = 7). In addition, also the phase-locking of LFP ripple and the synaptic conductance was not different between the control and the CsF-DIDS repatch (Figure 2.4 (D), phases range between 158° and 223° in control condition and 157° and 301° in CsF-DIDS). These

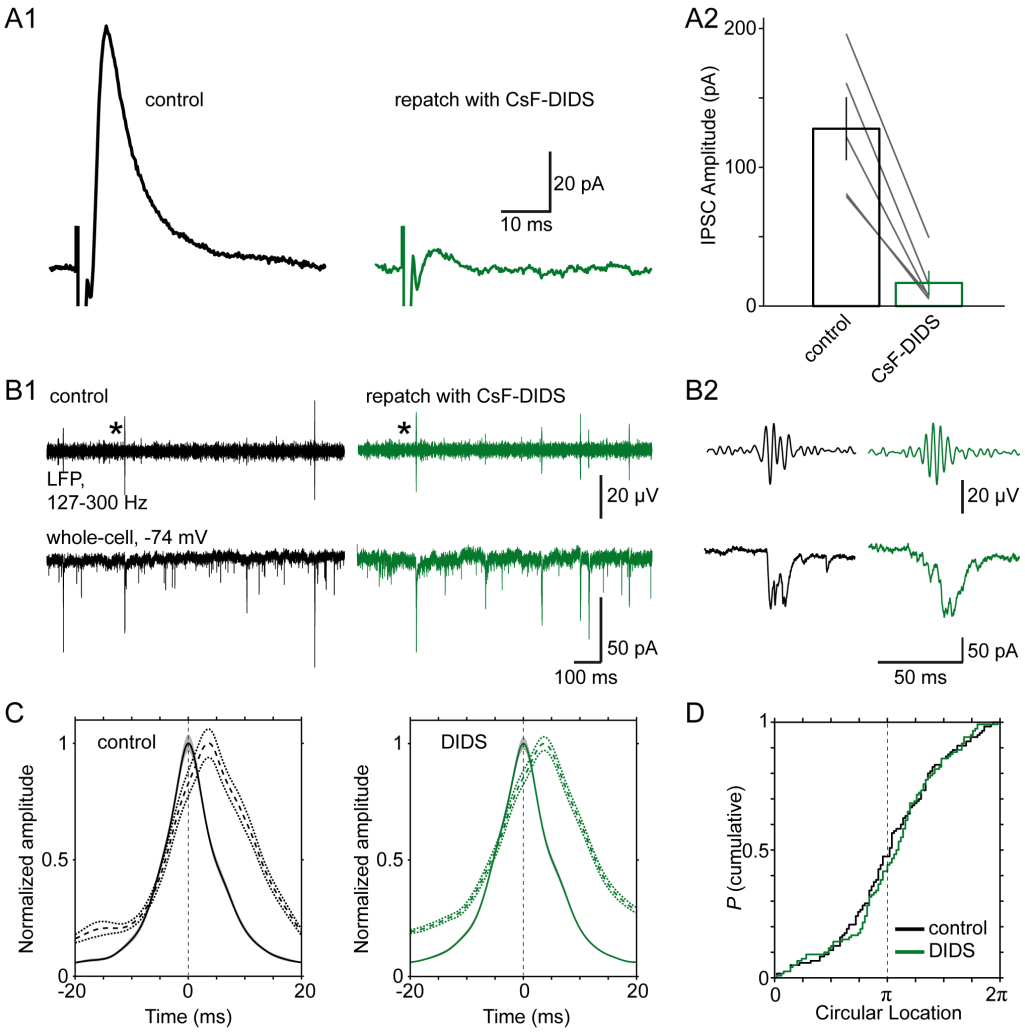

Figure 2.4 CsF-DIDS recordings confirm the excitatory nature of ripple-locked input to O-LM neurons. **(*A*)** (*A1*) *Left*: To demonstrate the intracellular block of postsynaptic inhibition, pharmacologically isolated, stimulus-evoked IPSCs were established (20 µM NBQX, 50 µM D-APV and 20 µM SCH50911 present in the extracellular medium, to block α-amino-3-hydroxy-5-methyl-4-isoxazolepropionic acid (AMPA)/kainate-, N-methyl-D-aspartate (NMDA)-, and γ-aminobutyric acid B (GABAB) receptors). *Right*: After repatch of the same O-LM cell with 1 mM CsF-DIDS, IPSCs were largely reduced. (*A2*) Summary plot demonstrating CsF-DIDS-mediated reduction of IPSCs (control: 127.8 ± 22.8 pA; CsF-DIDS: 16.7 ± 8.3 pA; 13% of control; P = 0.008; ranksum test; five cells). **(*B*)** Ripple-associated postsynaptic currents persisted upon repatch-perfusion of O-LM neurons with 1 mM CsF-DIDS (>10 min perfusion time) (*B1*) example traces for control and repatch conditions; (*B2*) magnification of the marked events. **(*C*)** Average envelopes of LFP ripples (continuous line) and conductances (dashed line) for control (*left*) and after perfusion with CsF-DIDS (*right*). Grey shades and dotted lines represent the standard estimation of the mean (SEM). Mean values of delay between peaks: 2.5 ± 0.4 ms and 3.0 ± 0.5 ms. **(*D*)** Cumulative probabilities plotted for cPSC-to-ripple phases before (black) and after CsF-DIDS perfusion (green; not different, P = 0.1, Kuiper's test). Mean vector angles and vector strengths: 189°; 0.43 (control), and 204°; 0.41 (DIDS).

results corroborate that the phasic character of the synaptic input is mainly based on excitation.

2.3 Timing of O-LM cell spikes and subthreshold membrane potential fluctuations during SWR

We saw that O-LM cells receive strong excitatory input during SWR and that this input is precisely timed and phase locked. We therefore were interested if this input is strong enough to lead to an active participation of the O-LM cells in SWR. To investigate this, we performed cell-attached recordings to avoid larger changes of the intracellular milieu. And indeed, in 13 out of 22 cells we observed action currents during the ripple oscillations. One example is shown in Figure 2.5 (A). Without in-depth analysis, we observed that the spikes occur late during the ripple, after the ripple maximum. This was confirmed in the analysis of all recorded 596 spikes in all cells which reveal the late occurring of spikes (Figure 2.5 (B), 6.5 ms, standard deviation (SD): 5.7 ms). In Figure 2.5 (C) in a phase plot it is shown that the spikes occur locked to the early ascending phase of the ripple (mean phase: 219 ± 9°; 350 spikes; 13 cells; range; 173° to 267°). In a subset of O-LM cells we recorded and

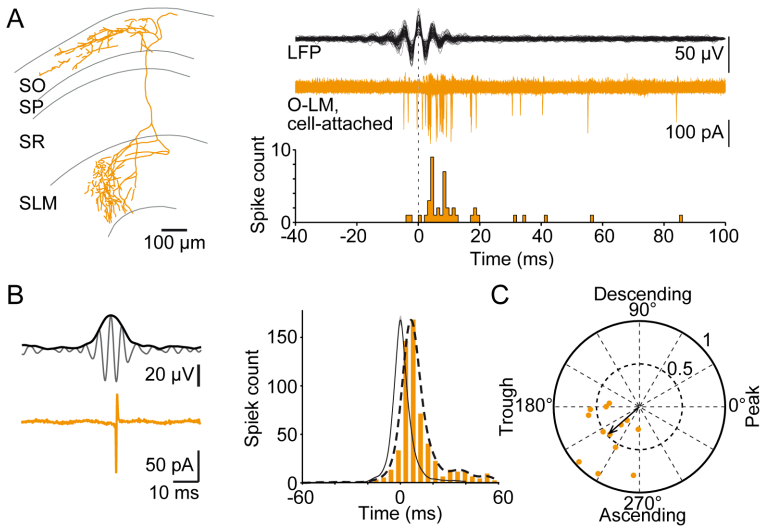

Figure 2.5 O-LM cells discharge during SWRs, and spikes are phase-locked to ripple oscillation cycles. **(*A*)** *Left*: reconstruction of an O-LM neuron. *Right*: overlaid traces of 87 band-pass filtered (127-300 Hz) ripple episodes (*top*, black) and respective cell-attached signals recorded from the displayed neuron (*middle*, orange); all traces were aligned to the ripple maximum (dotted line). *Bottom*: Spike time histogram of action-currents demonstrating delayed activation of the cell and ripple-locked discharge. **(*B*)** *Top left*: the 127-300 Hz band-pass filtered LFP overlaid with its envelope; *bottom left*: simultaneously recorded action-currents from the recording shown in (*A*). *Right*: the spike-time histogram (orange) includes all action currents obtained from 13 cell-attached recordings. Overlaid histogram profile (dashed line) represents the sum of Gaussians ($\sigma = 3.7$ ms) centered on the spike times. Spikes occur late during ripples. **(*C*)** Polar phase plot indicating average firing phases for the 13 cells recorded in the cell-attached mode (single-cell phase vector tips and vector strength, orange dots); the arrow represents the average vector (221° with a vector strength of 0.47). Note that spike phases cluster to the early ascending phase of ripples.

analyzed data in the current-clamp configuration (Figure 2.6 (A1) and (A2)). In ripple events that were not accompanied by spikes we observed voltage fluctuations with ripple frequency component. The phase locking of the LFP ripple with the voltage fluctuations in the O-LM cell recorded in the current-clamp configuration is shown in Figure 2.6 (B) by the coherence peak at 200 Hz. Comparable with

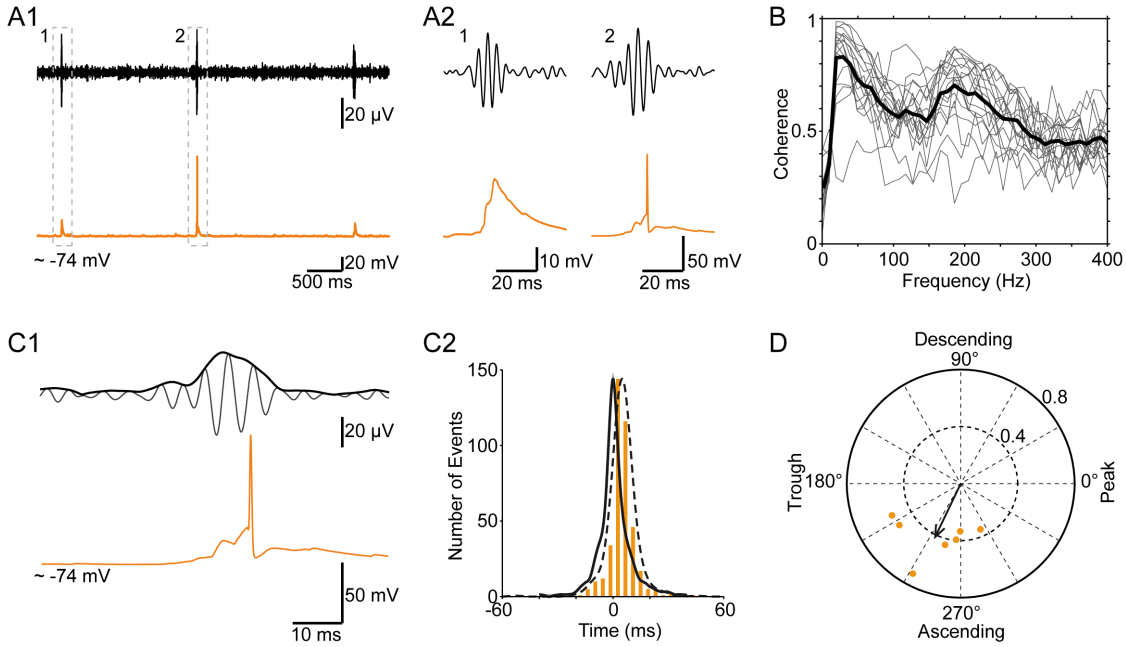

Figure 2.6 Current-clamp recordings in identified O-LM neurons reveal ripple-coherent postsynaptic voltage fluctuations. **(*A*)** (*A1*) The *upper* trace displays the 127-300 Hz band-pass filtered LFP (black); *bottom*: simultaneous current-clamp recording from an O-LM cell at resting membrane potential, as indicated. (*A2*) Magnification of the highlighted events shown in *A1*. **(*B*)** LFP ripples and their associated current-clamp equivalents are phase-locked, as indicated by a coherence peak at ∼200 Hz. The black line represents the average of 18 coherence functions (grey lines) each calculated for 20 randomly picked pairs of LFP and PSP events. **(*C*)** (*C1*) *Top*: ripple overlaid with its envelope; *bottom*: example of an action potential (magnified version of the data shown in *A2, right*). (*C2*) Histogram of spike times (orange) of seven O-LM neurons with respect to the peak of each corresponding ripple envelope (average, black; arbitrary units). Overlaid histogram profile (dashed line) represents the sum of Gaussians ($\sigma = 3.7$ ms) centered on the spike times (delay of spike times with respect to the ripple maximum: 5.2 ms; standard deviation: 6.2 ms; 401 spikes). Action potentials occur late during ripples. **(*D*)** Polar phase plot indicating average firing phases for seven cells. Note that spike phases cluster to the early ascending phase of ripples. Dots illustrate the degree of phase lock-ing (vector strength) of the phase distribution; circles and numbers in black indicate the calibration of vector strength; average vector: 244°, vector strength: 0.41.

the action currents in the cell-attached mode also the spikes recorded in current-clamp occur mainly after the ripple maximum (Figure 2.6 (C1) and (C2)) and were precisely time-locked with the LFP ripple with a preferred occurrence during the early ascending phase of ripples (Figure 2.6 (D)).

2.4 Strength of excitatory and inhibitory input determines recruitment of O-LM interneurons

So far we observed strong excitatory currents in the O-LM cells with a phase locking to the ascending phase of the LFP ripple oscillation waves. In addition we recorded action currents in the cell-attached recordings with a similar phase locking to the early ascending phase of the ripple in the LFP. However, we also found O-LM interneurons, that did not show ripple-associated spikes (9 out of 22 cells, ∼41%). To get insight into possible mechanisms between spiking and non-spiking O-LM cells

we analyzed further parameters of spiking and silent O-LM cells. First, we ruled out that experimental settings like the recording depth from the surface or intrinsic cellular parameters affect the spiking behavior of O-LM cells. The resting membrane potential (P = 0.68, K-S test) as well as the action potential threshold (P = 0.98, K-S test) and the input resistance (P = 0.68) were comparable in spiking and silent O-LM neurons (Figure 2.7). In addition, we analyzed the influence of the recording

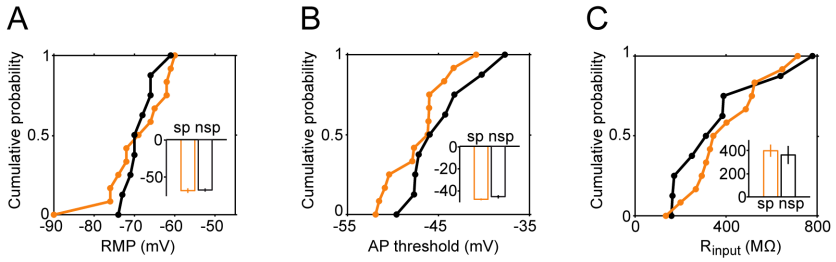

Figure 2.7 Ripple-activated and silent O-LM neurons are not different with respect to intrinsic cellular properties. **(*A*)** Distribution of resting membrane potentials (RMPs) for spiking (orange, median: -69 mV) and non-spiking O-LM neurons (black, median: -70 mV; not different, P = 0.75, K-S test). The bar graph (inset) represents the mean values -69.6 ± 2.3 mV and -68.8 ± 1.3 mV for spiking (sp) and silent (nsp) cells, respectively. **(*B*)** Distribution of action potential thresholds for spiking cells (orange, median: -46.2 mV, and silent cells (black), median: -46.0 mV; not different, P = 0.44, K-S test). Mean values are displayed in the bar plot (inset; -47.2 ± 0.3 mV vs. -44.8 ± 0.4 mV). **(*C*)** Distribution of input resistances (R_{input}) spiking vs. silent O-LM neurons (medians: 344 MΩ vs. 311 MΩ; not different, P = 0.68, K-S test). The inset displays the mean values (spiking vs. silent cells: 397 ± 47 MΩ vs. 361 ± 73 MΩ).

depth from the slice surface onto both the average input current and the percentage of SWR with spikes. Neither the input current nor the percentage of SWR with spikes are influenced by the recording depth (Figure 2.8). As we could exclude the

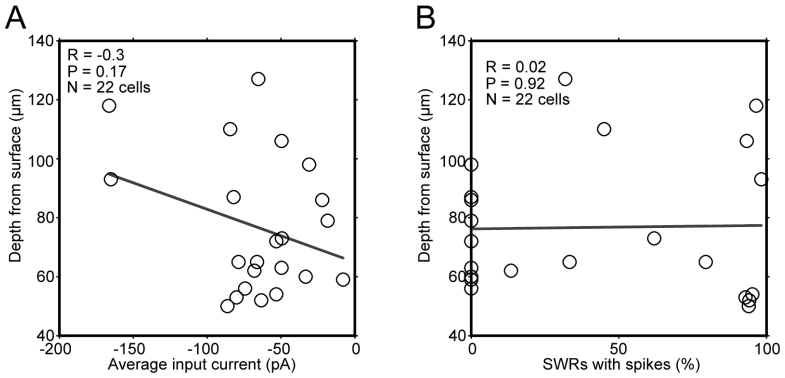

Figure 2.8 During SWRs, the average synaptic input current. **(*A*)** and the spiking probability of O-LM cells **(*B*)** are not correlated with the depth of the cell below the surface of the slice (n = 22 cells for both panels).

impact of intrinsic cellular parameters as well as the experimental setting, we next focused on the analysis of the synaptic inputs in O-LM interneurons. A plot of the percentage of SWRs with spikes in O-LM cells against the mean input current in these cells shows a correlation (R = -0.5, P = 0.017, holding potential: -74 mV) between these two parameters (Figure 2.9 (A)). Next, for spiking and silent O-LM cells separately, we analyzed the input currents, both at the reversal potential for

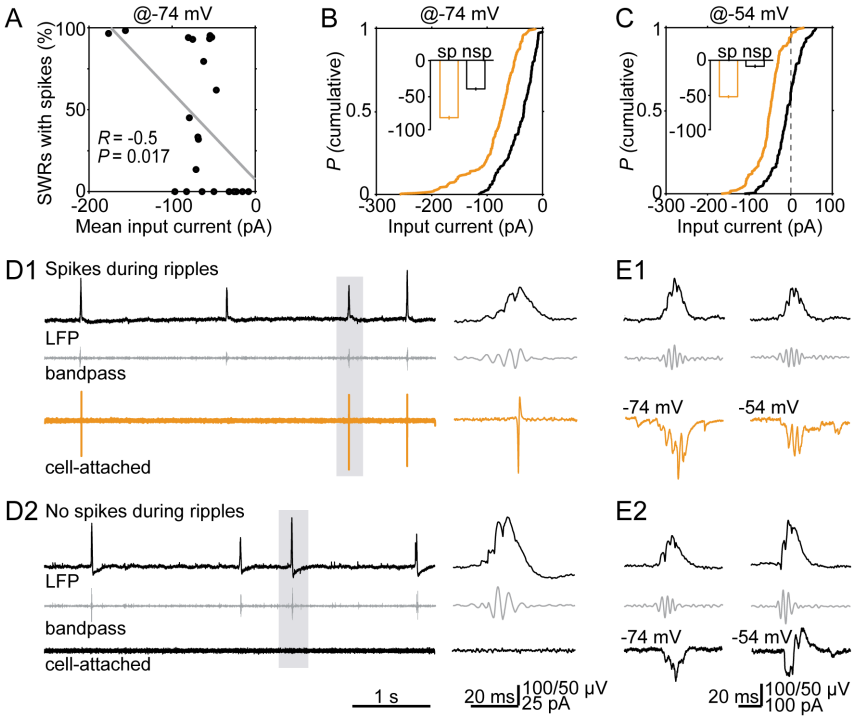

Figure 2.9 The magnitude of input currents determines the recruitment of O-LM neurons during ripples. **(*A*)** The spiking probability of O-LM cells during SWRs is correlated to their mean input current (R = -0.5; P = 0.017; n = 22 experiments). **(*B*)** Cumulative probability of the average input current in O-LM cells held at -74 mV for spiking (orange) and silent cells (black). Quartiles of spiking cells: Median: -72.9 pA, P25: -93.8 pA, P75: -53.7 pA; quartiles of non-spiking cells: Median: -33.8 pA, P25: -59.1 pA, P75: -19.3 pA. The inset shows the mean values (sp: spiking; nsp: nonspiking or silent). **(*C*)** Distributions of average input currents for spiking (orange) and silent (black) O-LM neurons held at -54 mV. Quartiles of spiking cells: Median: -49.2 pA, P25: -66.6 pA, P75: -33.5 pA; quartiles of nonspiking cells: Median: -8.2 pA, P25: -27.4 pA, P75: 12.1 pA. The inset shows the means values. **(*D*)** *Top*: unfiltered LFP, *middle*: 127-300 Hz band-pass filtered LFP, *bottom*: cell-attached recording of a spiking (*top panel, D1*, orange) and of a non-spiking O-LM cell (*bottom panel, D2*, black). The *right panels* show magnifications of the highlighted events. **(*E*)** *Top*: unfiltered LFP, *middle*: band-pass filtered LFP, *bottom*: cPSCs of a spiking (*E1*, orange) and a non-spiking O-LM cell (*E2*, black) close to the reversal potential of Cl^- (-74 mV, *left*) and at -54 mV (*right*).

chloride and, to unmask also the inhibition, at a more positive holding potential (at -54 mV). As shown in Figure 2.9 (B) the spiking O-LM cells received stronger excitatory currents as the non-spiking O-LM neurons (at -74 mV, for spiking: -82.7 ± 2.7 pA and silent cells: -41.3 ± 2.1 pA; P = 1.6×10^{-24}, K-S test). At the more depolarized holding potential, we observed stronger inhibition in the non-spiking O-LM cells (Figure 2.9 (C), at -54 mV, for spiking: -52.4 ± 2.2 pA and silent cells: -8.7 ± 2.5 pA; P = 4.1×10^{-33}, K-S test). In addition, also in single examples we found this difference in the excitatory and inhibitory currents (Figure 2.9 (D) and (E)). In Figure 2.9 (E1) the spiking O-LM cell receives excitatory input also at the more positive holding potential where the non-spiking O-LM neuron receives first excitatory and with some delay also inhibitory input.

These results indicate that the strength of excitatory input to the O-LM neuron define if the O-LM neuron participates actively during the SWR or if the cell remains silent. As a possible reason for this difference, we considered differences in

the strength of the underlying network activity: Indeed we observed a correlation between the percentage of SWRs with spikes and both the ripple amplitude and the SWR amplitude in the different O-LM cells. Furthermore the mean ripple amplitude and mean SWR amplitude over all spiking and non-spiking O-LM neurons were different (Figure 2.10 (A) and (B)). The percentage of SWRs with spikes and the associated inter-SWR interval of the experiments was not correlated, nevertheless the mean inter-SWR interval in experiments with spiking O-LM cells was significantly shorter than in experiments with non-spiking O-LM neurons (Figure 2.10 (C)).

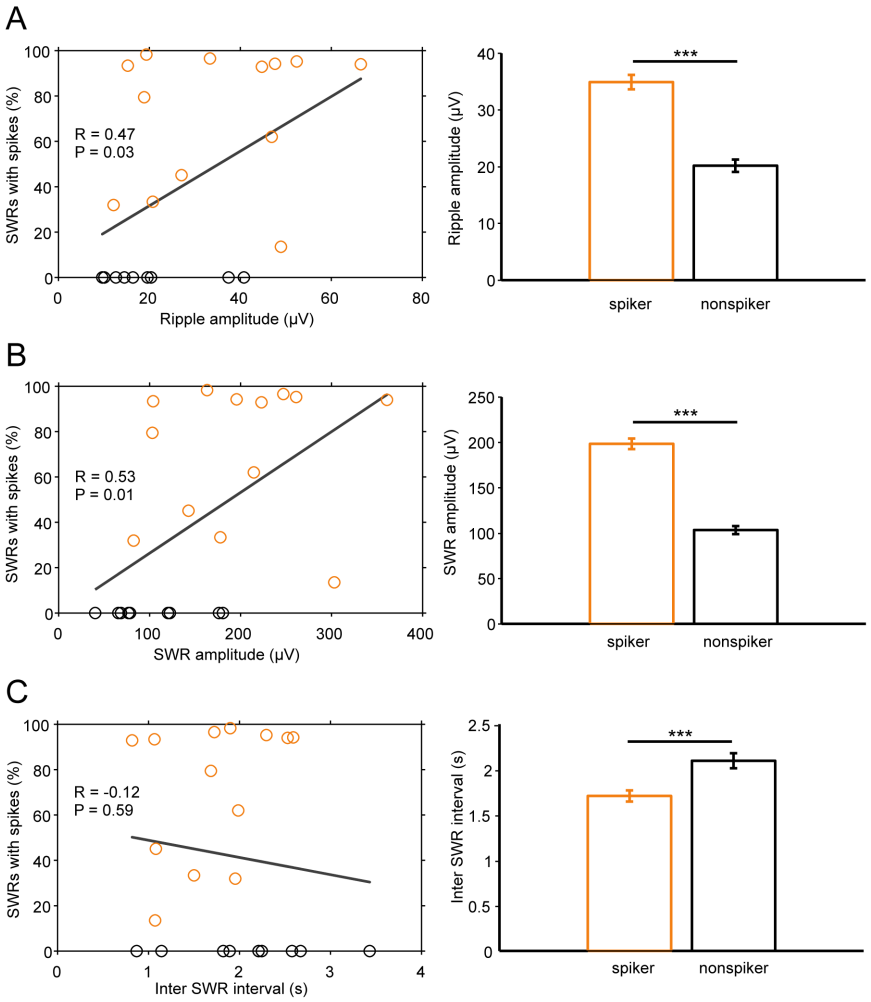

Figure 2.10 Summary of SWR characteristics in spiking and silent O-LM neurons derived from cell-attached experiments. **(*A*)** The *left panel* shows the percentage of SWRs associated with spikes as a function of ripple amplitude (moderate positive correlation; R = 0.47; P = 0.03; 22 experiments). The *right panel* shows the mean values of ripple amplitude for spiking and nonspiking O-LM neurons (34.9 ± 1 µV vs. 20.2 ± 1 µV; P = 2.8×10^{-18}; ranksum test; 22 experiments). **(*B*)** *Left*: percentage of SWRs associated with spikes as a function of SWR amplitude; both quantities are moderately positively correlated (R = 0.53; P = 0.01). *Right*: Mean values of SWR amplitudes for spiking and nonspiking O-LM neurons (198.4 ± 5.8 µV vs. 103.3 ± 4.4 µV; P = 5.2×10^{-28}; ranksum test; 22 experiments). **(*C*)** *Left*: percentage of SWRs associated with spikes as a function of the mean inter-SWR interval (no correlation; R = 0.12; P = 0.6; 22 experiments). *Right*: mean values of the inter SWR-intervals for spiking vs. nonspiking neurons (1.7 ± 0.1 s vs. 2.1 ± 0.1 s; P = 5.0×10^{-5}; ranksum test; 22 experiments).

2.5 Discussion

In this study we investigated O-LM interneurons *in vitro* during ripple oscillations in the CA1 network. In addition to the suprathreshold recruitment of O-LM cells, we studied the underlying synaptic mechanisms in all recorded cells. We found cPSCs related to the ripples in the O-LM neurons and saw that these currents were mainly excitatory. This contrasts the cPSCs in pyramidal neurons which displayed mainly inhibitory outward currents at the same holding potential. Further analysis with regard to the timing of the excitatory input revealed that the input is late with respect to the LFP SWR and locked to the early ascending LFP ripple phase. We also observed that this excitatory input is sufficient to lead to an active participation of O-LM cells during SWR. In 13 out of 22 O-LM neurons we observed spikes which occurred late with respect to the ripple in the LFP, consistent with the late excitatory synaptic input. Most of the spikes occurred after the maximum of the ripple in the field and locked to the early ascending phase of the LFP ripple.

Not all of the recorded O-LM interneurons examined in our work fired action potentials during SWRs, 9 out of 22 were silent. We also focused on this ambivalent behavior of the O-LM cells during ripple oscillations. We tested if the amount of synaptic input was correlated to the spiking probability of O-LM neurons and we found such a correlation. In addition to this we observed stronger excitatory and less inhibitory synaptic input in spiking versus silent O-LM neurons. As intrinsic parameters like resting membrane potential, input resistance and the action potential threshold can change the firing probability of a cell, we analyzed all these parameters. However, they were all statistically similar and therefore unlikely to influence the spiking activity of O-LM interneurons. The recording depth below the slice surface could influence the extent to which synaptic connections are preserved in the recorded cell. We could rule out this hypothesis. Parameters like the amplitude of the ripple or the amplitude of the SPW in the LFP or the incidence of SWRs can be used to quantify activity levels of the network. All these parameters were enhanced in the spiking O-LM neurons, indeed suggesting a dependence of spiking in O-LM cells from the activity level of the network. An additional factor that can influence the spike rate of neurons is the relation of excitation and inhibition. This ratio might also contribute as we saw smaller inhibitory synaptic currents recorded at a slightly depolarized recording potential (-54 mV) in the spiking O-LM interneurons.

Chapter 3

Comparison of synaptic input in deep and superficial CA1 pyramidal cells during ripple oscillations

3.1 Heterogeneity of CA1 pyramidal neurons

The pyramidal cell layer in CA1 is often presumed as a layer with a homogenous group of principal cells. However there were several differences observed regarding pyramidal cells located more proximally (close to CA2) or more distally (close to the subiculum) as well as the cells located more to the stratum radiatum (superficial cells) or more to the stratum oriens (deep cells).

Proximal pyramidal cells receive input from the medial entorhinal cortex (MEC) and therefore receive more spatial information compared with the distal paramidal cells which are innervated by the lateral entorhinal cortex (LEC). Additionally, proximal pyramidal neurons fire phase-locked to theta activity in the MEC (Tamamaki and Nojyo, 1995; Henriksen et al., 2010). Also along the proximal-distal axis, the probability of pyramidal neurons to burst is different. At the proximal site the percentage of bursting cells is much smaller compared with the bursting cells found at the distal site (10 % versus 34 %; Jarsky et al., 2008).

In addition, pyramidal cells in the superficial or deep layer of the stratum pyramidale show anatomical differences. The dendrites of superficial cells terminate more often in the stratum radiatum whereas dendrites of deep pyramidal cells preferentially terminate in stratum oriens (Bannister and Larkman, 1995). Differences in pyramidal cells of the superficial and deep layer were already observed 1991 by Baimbridge who described calbindin D28k (CB) positive neurons in the superficial, and CB-negative neurons in the deep layer. They further noticed an earlier occurrence of CB-negative compared with CB-positive neurons during neurogenesis by

one to two days (Baimbridge et al., 1991). Differences in long-range projections in the superficial and deep pyramidal cells have been reported, too. Deep, CB-negative cells project to more diverse brain areas, and they have denser innervation patterns as superficial, CB-positive neurons. Additionally, although all pyramidal neurons project to the subiculum only the superficial, CB-positive ones terminate in the molecular layer of the subiculum (Arszovszki et al., 2014).

Superficial and deep pyramidal cells do not only show anatomical and immunohistochemical differences, they also have different physiological properties and firing behavior during gamma and theta oscillations. Senior et al. (2008) investigated pyramidal cell firing during theta-nested gamma oscillations in the awake rat. They observed two populations of pyramidal neurons, one which discharged at the trough, the other which discharged in the rising phase of gamma oscillation. Besides the timing of the firing these two types of pyramidal neurons also showed differences in spike waveform, firing rate and burst firing tendency (Senior et al., 2008). Buzsáki and co-workers investigated the phase-locked firing of superficial and deep pyramidal cells in more detail: They investigated in freely moving rats the firing properties of pyramidal cells during different brain states. While all pyramidal cells fired at the trough of theta when the animal explored the maze, the deep pyramidal neurons change their firing and fire at the peak of theta during rapid eye movement (REM) sleep. The authors also found higher firing rates, more bursting cells, more cells with place fields and stronger modulations in the pyramidal neurons of the deep layer (Mizuseki et al., 2011).

In an additional study published by Lee et al., 2014 it was shown that deep pyramidal cells receive three times stronger inhibition from parvalbumin expressing (PV) basket cells than superficial pyramidal neurons. However, superficial cells provide stronger excitation to PV basket cells than deep pyramidal neurons. This suggests a stronger inhibition of the pyramidal neurons in the deep layer after excitatory activity in the pyramidal layer. The superficial pyramidal cells activate the PV basket interneurons which then strongly inhibit the deep pyramidal neurons. In addition to this subdivision of the pyramidal layer into a superficial and a deep layer the pyramidal cells in the deep layer can be further classified according to their long range projection areas. These subgroups differ in the strength of inhibitory inputs they receive from PV basket cells (Lee et al., 2014).

The experiments and results summarized in the following focused on the synaptic inputs into deep and superficial pyramidal cells during ripple oscillations. Due to the strong differences in inhibitory synaptic inputs from soma targeting PV basket cells, we assumed a different integration of the two groups of pyramidal neurons into the network during SWRs.

3.2 Subdividing CA1 pyramidal cells

We recorded from deep or superficial pyramidal cells in the whole-cell configuration in parallel with the local field potential. In principle, the classification of the cells ac-

cording to their position in the cell layer could be determined during the experiment but can be only unequivocally classified in post-hoc stainings. During the recording we therefore loaded the cells with biocytin to allow for post-hoc identification of cell type and localization of the neuron (Figure 3.1 (A)). In some cells calbindin could be

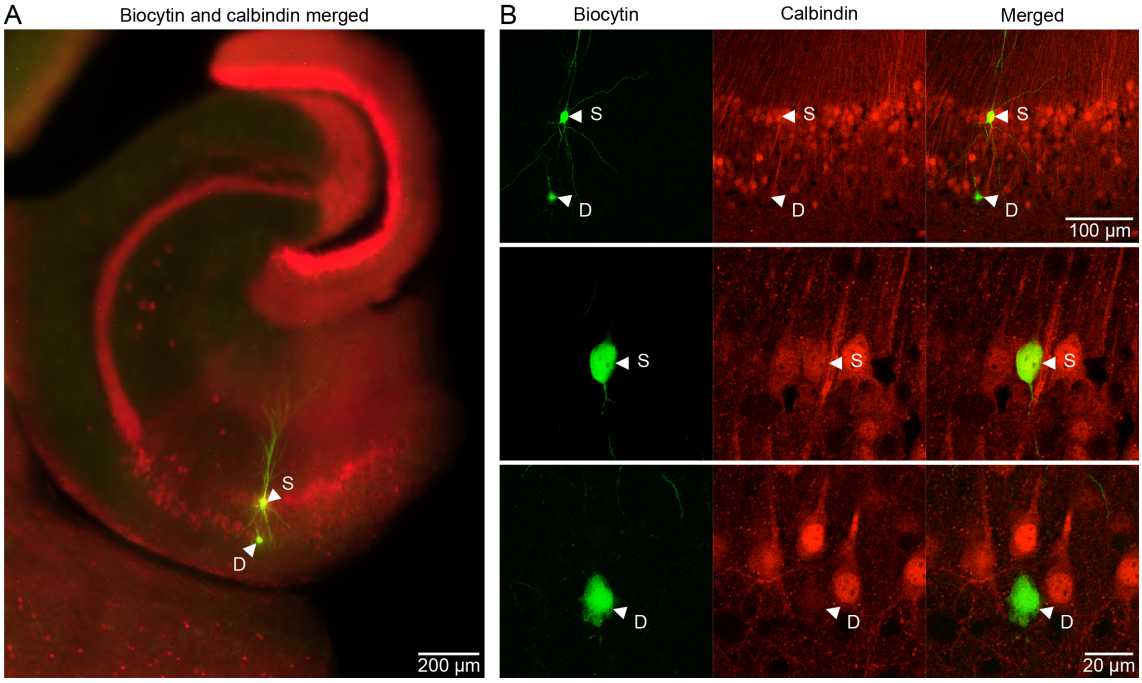

Figure 3.1 Post-hoc staining of recorded deep and superficial pyramidal neurons in the ventral CA1, immunoreactivity for calbindin could be observed in a subset of CA1 pyramidal neurons. **(*A*)** Fluorescence microscopic overview tile scan showing immunofluorescent labeling in the hippocampus for calbindin (AF594, red) and for biocytin (AF488, green). Arrows indicate a superficial (S) and a deep (D) pyramidal neuron. Note: Calbindin is located not only in the superficial layer. **(*B*)** Confocal single plane images. *Top:* Zoom in into the pyramidal cell layer in CA1, the arrows mark the superficial and deep pyramidal neurons as in *A*. Larger magnfication of the superficial (*middle*) and deep (*bottom*) pyramidal cell. *Left:* Biocytin staining (green), *middle:* calbindin staining (red) and *right:* overlay of biocytin and calbindin staining. Note: The superficial pyramidal cell is calbindin positive, the deep pyramidal cell is calbindin negative.

detected additionally (Figure 3.1 (B), *middle*). Note that in horizontal slices from the ventral pol of the hippocampus (Figure 3.1 (A)) there is no continuous calbindin staining of the superficial layer. At the proximal pole of CA1 pyramidal cells in the deep layer are calbindin immunoreactive. Approximately in the middle of CA1 up to the distal pole there is a switch of the calbindin immunoreactivity towards the superficial pyramidal cells, where calbindin staining is even stronger.

3.3 Ripple-associated reversal potential

During the ripple oscillation all pyramidal cells in area CA1 receive synaptic inputs. At holding potentials negative to the reversal potential of chloride, these inputs appear as inward currents that contain a temporal overlay of excitatory and inhibitory currents. Close to the reversal potential of chloride cPSCs are minimal in amplitude

and display mainly excitatory synaptic input; at even more positive holding potentials (above ∼-50 mV) cPSCs display a small inward component followed by an outward component. And if the cell is clamped to again more positive holding potentials the cPSCs are outward currents. The amplitude of the composed excitatory and inhibitory ripple-associated component at a given holding potential results from the driving forces of both excitatory and inhibitory synaptic inputs to the cell; given the dominance of inhibitory inputs during ripples possible differences of inhibitory signaling among deep and superficial pyramidal cells might be significant. If deep and superficial pyramidal cells are differently integrated in the network and deep pyramidal cells receive more inhibition, the inhibition to excitation ratio could be altered. In this case the ripple-associated reversal potential should be also different in the two groups.

We recorded from deep and superficial pyramidal cells at different holding potentials starting at a negative potential of around -70 mV. Then we increased the holding potential in steps of 5 mV and recorded ripple-associated cPSCs at each of these potentials (Figure 3.2 (A)). Figure 3.2 (B) shows a slight shift of the ripple-associated reversal potential to more negative potentials in the deep cells compared with the superficial neurons (V_{rev},deep = -58.7 mV; V_{rev},superficial = -50.8 mV). For this figure the mean of all cPSCs from all deep or all superficial cells at a given holding potential were calculated and all mean values were fitted with a linear regression. A slightly different analysis of the same data came to similar results: The separate

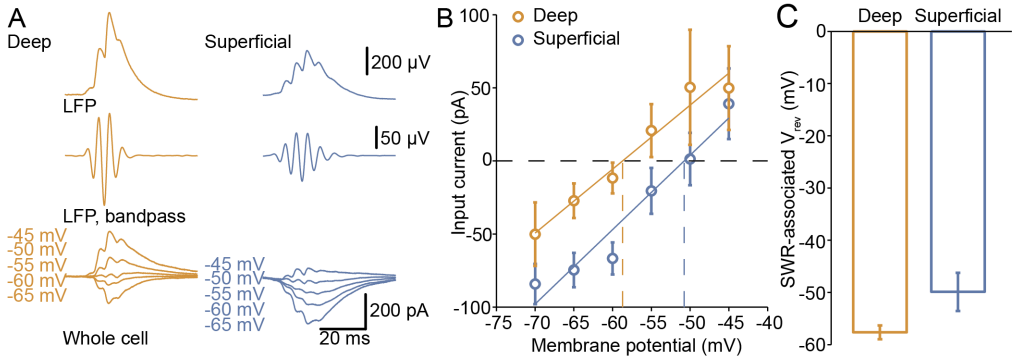

Figure 3.2 ripple-associated reversal potential in deep and superficial pyramidal cells. **(*A*)** Simultaneous LFP and whole-cell voltage-clamp recordings at different holding potentials show stronger outward currents in the deep compared to the superficial pyramidal neurons. (*Top*) Mean of all SWR events. (*Middle*) Ripple component of the SWR events (120-300 Hz band-pass filtered). (*Bottom*) Mean cPSCs at the different holding potentials, (*left*) for the deep and (*right*) for the superficial pyramidal cells. **(*B*)** Deep pyramidal cells display a more negative ripple-associated reversal potential than superficial pyramidal cells (V_{rev},deep = -58.7 mV; V_{rev},superficial = -50.8 mV). **(*C*)** Mean of separate for every cell estimated SWR-associated reversal potential (mean V_{rev},deep = -57.6 ± 1.3 mV; mean V_{rev},superficial = -49.9 ± 3.6 mV; P = 0.28, rank-sum test, n = 5 deep pyramidal cells, n = 8 superficial pyramidal cells).

estimation of the reversal potential in single cells (Figure 3.2 (C)) shows the same shift (mean V_{rev},deep = -57.6 ± 1.3 mV; mean V_{rev},superficial = -49.9 ± 3.6 mV) as for pooled deep and superficial pyramidal cells. This finding indicates that the deep pyramidal cells receive either less excitatory or more inhibitory synaptic currents.

However, with the given numbers of cells (n = 5 deep pyramidal cells, n = 8 superficial pyramidal cells) and the variability within the dataset, the finding remains a trend (no significant difference, P = 0.28; rank-sum test).

3.4 Reversal potential of chloride in deep and superficial CA1 pyramidal neurons

Wiring properties of the neuronal network, but also intrinsic properties of the single cell and especially the reversal potential of chloride can influences the magnitude of inhibitory currents at a particular holding potential. Different chloride reversal potentials in deep and superficial pyramidal cells can lead to different ripple-associated reversal potentials if both groups would receive the same amount of excitatory and inhibitory synaptic inputs. On the other hand, systematic differences in the reversal potential of chloride could also mask different ripple-associated reversal potentials in deep and superficial pyramidal cells. To differentiate between these two possibilities we performed experiments to estimate the reversal potential for chloride in deep and superficial cells.

We recorded evoked IPSCs in the presence of AMPA/kainate, NMDA and GABAB receptor blockers in the two cell groups and held the cells at different potentials. Comparable to the recordings of ripple-associated reversal potentials the cells showed strong inward currents at very negative holding potentials. The more positive the holding potential the weaker were the inward currents, they disappeared at the reversal potential and reversed to outward currents at holding potentials positive to the reversal potential. Figure 3.3 (A) and (B) shows examples of recorded IPSCs at different holding potentials for a deep and superficial cell respectively. The collected data were analyzed with two different methods, the first using a linear regression fit through all data points and the zero crossing gives the reversal potential (Figure 3.3 (C1) and (D1)). The other method used only the closest two points above and below zero. The reversal potential for each cell was estimated by the zero crossing of the line connecting the two points (Figure 3.3 (C2) and (D2)). Both methods revealed nearly identical reversal potentials for deep and superficial pyramidal cells (V_{rev},deep all points = -65.3 mV and V_{rev},superficial all points = -61.3 mV; and V_{rev},deep two points = -65.7 mV and V_{rev},superficial two points = -61.2 mV, P = 0.06, rank-sum test, n = 8 deep pyramidal cells, n = 9 superficial pyramidal cells).

3.5 Excitatory and inhibitory synaptic currents in pyramidal cells during SWRs

As shown above (3.3), for SWR associated reversal potentials we found a trend that we were interested to analyze in greater detail. In the recordings of the SWR-associated reversal potential there was always a mix of inhibitory and excitatory

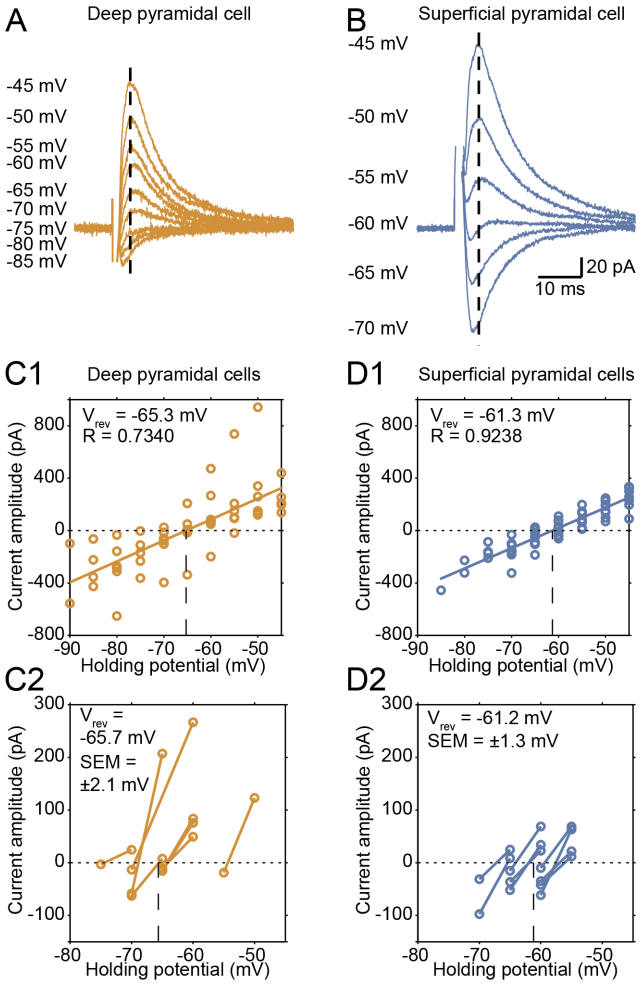

Figure 3.3 Reversal potential for inhibition in deep and superficial pyramidal cells. **(*A*)** Example traces of evoked inhibitory PSCs of a deep pyramidal cell recorded at different holding potentials in the presence of antagonists for AMPA/kainate, NMDA and GABAB receptors (20 µM NBQX, 50 µM D-APV, 20 µM SCH 50911). The dashed line mark the time point of the maximum in the recording at -45 mV. At this time point the values in each of the recorded signals at the different holding potentials were selected. **(*B*)** Example traces like in *A*, but recorded from a superficial pyramidal neuron. **(*C*)** The amplitudes were plotted against the holding potentials and the zero crossing of the linear regression through all points reveal the chloride reversal potential. (*C1*) For the deep pyramidal cells the calculated reversal potential is -65.3 mV. (*C2*) The reversal potential for the superficial pyramidal neurons is -61.3 mV. **(*D*)** An alternative method for the estimation of the reversal potential shows similar values. For this method for every cell the amplitude values below and above zero were plotted and the mean of all zero crossings were calculated. (*D1*) In deep pyramidal cells is the reversal potential with this method at -65.7 mV. (*D2*) Superficial pyramidal cells have a reversal potential of -61.2 mV.

synaptic currents. To differentiate between the excitatory and inhibitory component of the cPSCs in deep and superficial pyramidal cells we performed experiments where the cells were clamped at a holding potential close to the reversal potential for excitation and inhibition. At the reversal potential for chloride at around -65 mV mainly excitatory currents could be recorded. Vice versa, at the reversal potential for excitation at around +6 mV, mainly inhibitory currents were recorded.

Figure 3.4 (A) shows the recording of a deep and a superficial pyramidal neuron. Both cells receive excitatory synaptic currents during SWRs when recorded close to

the chloride reversal potential. The same cells were also recorded at the reversal po-

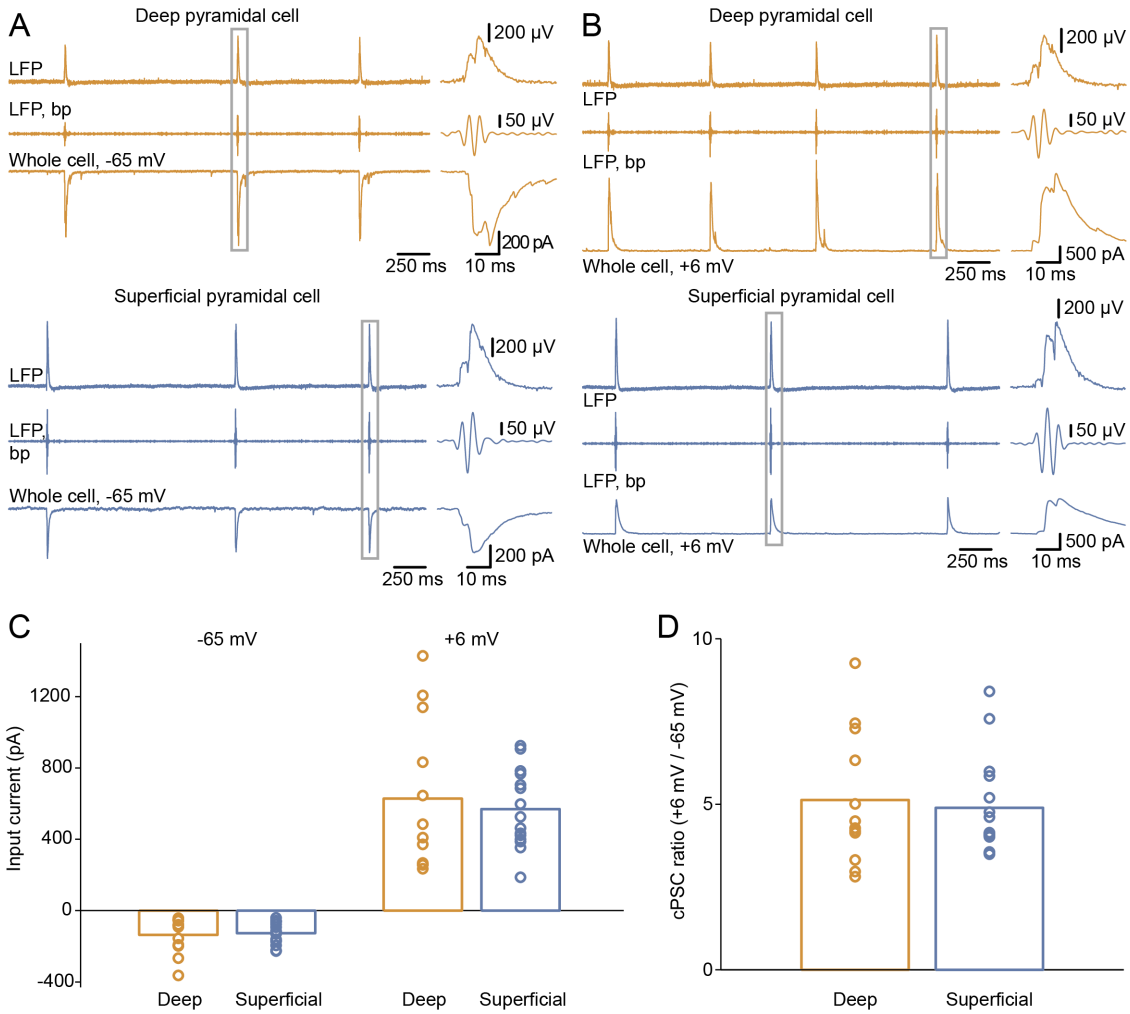

Figure 3.4 Excitatory and inhibitory cPSCs are not different in deep and superficial pyramidal neurons. **(*A*)** Example of excitatory cPSCs in deep (*top*, orange) and superficial (*bottom*, blue) pyramidal cells. In each panel on the top the LFP signal is shown, band-pass filtered LFP (120 - 300 Hz band-pass (bp) filter) (*middle*), whole-cell recording voltage-clamped at -65 mV, close to the reversal potential of chloride (*bottom*). On the (*right*) the depicted event is magnified. **(*B*)** Example traces of inhibitory cPSCs recorded close to the reversal potential of excitation at a holding potential of +6 mV in deep (*top*, orange) and superficial (*bottom*, blue) pyramidal neurons were shown. For each recording the unfiltered LFP (*top*), the 120 - 300 Hz band-pass filtered LFP (*middle*) and the whole-cell recording (*bottom*) is shown. (*Right*) Magnification of the highlighted events. **(*C*)** The calculated mean input currents show no differences between deep and superficial pyramidal cells ($p_{-65\ mV} = 0.75$ and $p_{+6\ mV} = 0.79$, rank sum test, n = 12 deep and n = 15 superficial pyramidal cells). Note the wider variability in the deep pyramidal cells. **(*D*)** The ratio between the inhibitory and the excitatory currents is comparable in deep and superficial pyramidal neurons ($p_{ratio} = 0.83$, rank sum test, n = 12 deep and n = 15 superficial pyramidal cells).

tential for excitation and both, the deep and the superficial pyramidal neuron receive strong inhibitory currents during the ripple oscillation (Figure 3.4 (B)). Summery of the calculated excitatory and inhibitory input currents of 12 deep and 15 superficial pyramidal neurons is shown in Figure 3.4 (C). Neither the mean excitatory nor the mean inhibitory current differed between the two groups. However, the variance of the mean current values for the excitatory as well the inhibitory currents of the

single cells differed: Excitatory currents: variance deep cells = $1.03\times10^{+4}$; variance superficial cells = $3.83\times10^{+3}$; inhibitory currents: variance deep cells = $1.79\times10^{+5}$; variance superficial cells = $4.76\times10^{+4}$. To investigate if there were differences of the inhibitory synaptic currents in relation to the excitatory synaptic currents the ratio between these two conditions in each cell were calculated (Figure 3.4 (D)). However cIPSC-to-cEPSC ratios did not differ between deep and superficial pyramidal neurons.

All previous recordings were performed either as single LFP-and-whole-cell recordings or as sequential recordings of a deep and a superficial cell in a random order for each hippocampal slice investigated. To rule out biases caused by this experimental procedure, in a subset of experiments we recorded from a deep and a superficial cell in parallel. Figure 3.5 (A) shows an example from such a recording. Both cells show cEPSCs at the holding potential of -65 mV and cIPSCs at the holding potential of +6 mV during the ripple oscillation. Mean values of all three parallel recordings are shown in Figure 3.5 (B). Each of the recordings show a different behavior. In recording 1 the superficial cell receives both stronger excitatory and inhibitory synaptic currents as the deep pyramidal neuron. In recording 2 both cells receive comparable amounts of excitatory and inhibitory currents. Finally, in recording 3, the deep neuron receives stronger synaptic inputs compared to the superficial cell. A quantitative analysis of each input was done and the synaptic input currents of superficial cells were plotted against the input currents of the deep cells (Figure 3.5 (C)). In single examples there are shifts to stronger currents in one of the cells, but across all examples there is no tendency for deep or superficial cells to receive stronger currents during the SWR events.

Summarising the results: In the deep and superficial pyramidal cells we saw a slight, however not significant difference of the SWR-associated reversal potential. Nevertheless, this difference could be based on different reversal potentials for chloride or different strength of excitatory and inhibitory currents in the deep and superficial pyramidal neurons. We observed both comparable reversal potentials for chloride and comparable cEPSCs and cIPSCs. These results indicate that also the SWR-associated reversal potentials are comparable in deep and superficial pyramidal neurons.

3.6 Discussion

3.6.1 Classification of deep and superficial pyramidal neurons

We recorded from deep and superficial pyramidal cells in CA1 to investigate the integration of these anatomically and physiologically different cell groups into the network during ripple oscillations. With combined biocytin and calbindin staining after the recordings we could unequivocally differentiate deep and superficial cells. The strong calbindin staining shows calbindin positive cell bodies in CA1. Unlike

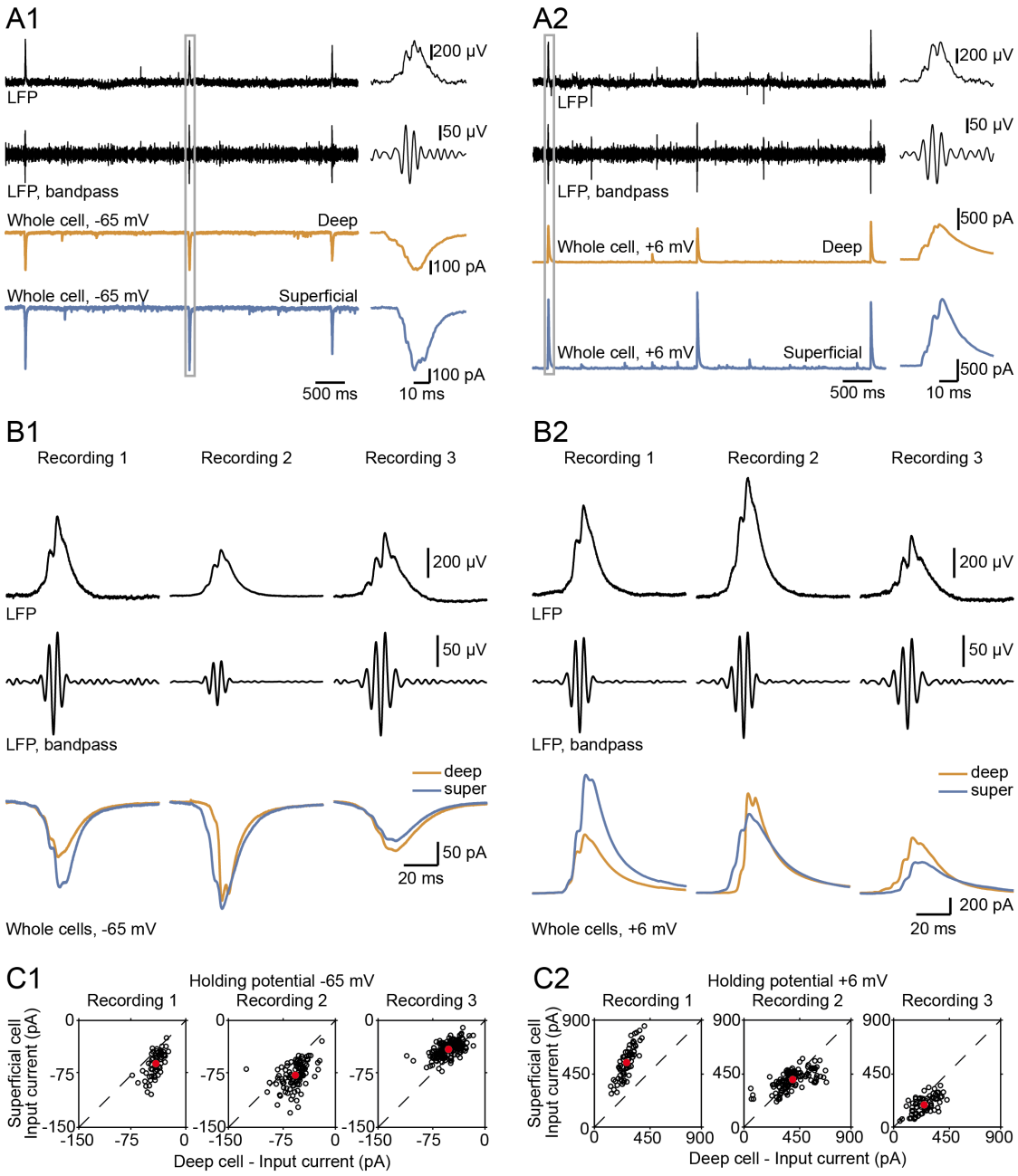

Figure 3.5 Three parallel recordings from deep and superficial pyramidal neurons do not reveal differences in excitatory or inhibitory cPSCs. **(*A*)** Example traces from a simultanous field, and double whole-cell recording. (*Top*) Unfiltered LFP, (*upper middle*) ripple (120 - 300 Hz band-pass filtered LFP), (*lower middle*, orange) whole-cell recording from a deep pyramidal cell, (*bottom*, blue) whole-cell recording from a superficial pyramidal cell. (*A1*) Whole-cell recording close to the reversal potential for chloride, (*A2*) recording of inhibitory synaptic currents with a holding potential around the reversal potential for excitation. **(*B*)** Average of all events of the three parallel recordings. (*Top*) Mean LFP events, (*middle*) mean ripple events (band-pass filtered at 120 - 300 Hz), (*bottom*) overlay of mean cPSCs of deep (orange) and superficial (blue) pyramidal neurons. (*B1*) Parallel recording of excitatory cPSCs. (*B2*) Parallel recording of inhibitory cPSCs. **(*C*)** In the three examples there is no tendency to larger input currents in deep or superficial pyramidal cells. (*C1*) In deep as well as superficial pyramidal cells there is the same amount of excitatory cPSCs. (*C2*) Also the inhibitory cPSCs do not show different magnitudes in the deep and superficial pyramidal neurons. The red dots indicate the mean values.

calbindin stainings in the dorsal part of CA1 the calbindin positive cells are not exclusively located in the superficial layer. The proximal part of CA1 shows very few calbindin positive cells in the superficial layer but a moderate calbindin staining in the deep layer. In the middle of CA1 there is a switch to a strong calbindin staining in the superficial pyramidal layer.

In some cells (example in Figure 3.1 (B)) we found expression of calbindin. However it is known that there is a wash-out of calbindin during the recording (Müller et al., 2005). After 15 minutes there is less than 25 % left from the fluorescence at the beginning of the recording. We therefore grouped the cells by their anatomical localization rather than immunocytochemical markers and recorded from very deep and very superficial pyramidal cells directly at or very close to the boarder to stratum oriens or stratum radiatum to avoid a wrong classification.

3.6.2 Slightly different SWR-associated reversal potential in deep and superficial pyramidal neurons

The two groups of pyramidal cells had slightly but not significantly different SWR-associated reversal potentials. The reversal potential of deep cells was more negative compared to the reversal potential of the superficial cells. This means that at the same membrane potential a deep cell receives less excitation than a superficial cell, or more inhibition or a combination of both. This would fit with the results from Lee et. al (Lee et al., 2014). They recorded unitary IPSCs (uIPSCs) evoked by PV positive basket cells in pyramidal neurons and observed a stronger inhibition in the deep pyramidal cells.

3.6.3 Comparable chloride reversal potential in deep and superficial pyramidal cells

We ruled out that differences in the chloride reversal potential, i.e. the reversal potential of inhibition, could influence the SWR-associated reversal potential. The reversal potential for deep and superficial pyramidal cells was very similar however not significantly different. Of note, the variability in the measurements in the group of deep cells in comparison to the group of superficial cells was much higher. This fact is displayed in the correlation coefficient in Figure 3.3 (C1) and (D1), (R deep = 0.7340; R superficial = 0.9238).

Chapter 4

Analysis of synaptic inputs in pyramidal neurons in area CA2 during SWRs

4.1 Region CA2 of the hippocampus

CA2 is a relative small region located between CA1 and CA3 in the hippocampus. After this region had been neglected for a long time, more and more research has been done on this region recently. First described by Lorente de Nó (1934) meanwhile the definition of the exact borders have changed. Expression of Purkinje cell protein 4 (PCP4) is mostly used in *in situ* hybridisations and immunolabelings to define the borders to CA1 and CA3 (Lein et al., 2005; San Antonio et al., 2014; Kohara et al., 2014). PCP4 is also expressed in the dentate gyrus but its expression is not overlapping with the CA1 marker mannosidase 1, alpha and the marker for CA3 the bcl-2-related ovarian killer protein (Lein et al., 2005). If the border between CA2 and CA3 is defined due to the PCP4 expression then a part of CA2 cells overlaps with the mossy fibers conflicting with the former definition which used the end of the mossy fiber tract to delineate the border between CA2 and CA3 (Lein et al., 2005; Kohara et al., 2014).

Besides PCP4 there are several other proteins with characteristic expression in CA2 neurons. Within the hippocampus, these markers are either highly enriched in the CA2 region or exclusively expressed in this subfield (Piskorowski and Chevaleyre, 2012). These CA2 marker proteins include adenosine A1 receptors which have the strongest immunoreactivity after P28 (Ochiishi et al., 1999), the vasopressin 1b receptor (Avpr1b) which is prominently expressed in CA2 pyramidal neurons (Young et al., 2006), and the metabotropic glutamate receptor type 4 (mGluR4) which was in the hippocampus exclusively detected in the CA2 region (Phillips et al., 1997). In addition, the epidermal growth factor (EGF) receptor is strongly expressed in the cell bodies of CA2 neurons in adult rats (Tucker et al., 1993), and within the hippocampus the expression of the α-actinin-2 protein is comparably strong in the

molecular layer of dentate gyrus and in the CA2 region (Wyszynski et al., 1998). Finally, the regulator of G-protein signaling 14 (RGS14) is also highly enriched in CA2 pyramidal neurons (Lee et al., 2010).

In comparison to CA1 the CA2 pyramidal cells have a larger soma and also the dendritic ramification is different. Apical dendrites of CA1 pyramidal neurons bifurcate far away from the soma. In contrast, CA2 pyramidal neurons have apical dendrites which bifurcate close to the soma (Ishizuka et al., 1995; Chevaleyre and Siegelbaum, 2010). The bifurcation of the apical dendrite is not an exclusive property of CA2 neurons but is also observed in CA3 pyramidal cells. A dendritic feature to distinguish between these two cell types are the thorny excrescences which are characteristic of CA3 pyramidal neurons (Ishizuka et al., 1995).

Besides anatomical and histochemical differences between CA2 pyramidal neurons in comparison to CA1 and CA3 there are also differences regarding interneurons. For example, in the pyramidal cell layer of CA2 more parvalbumin, somatostatin, calbindin and vasoactive intestinal polypeptide positive interneurons can be found than in the same layer in CA1 or CA3 (Botcher et al., 2014). So far, however, in CA2, only few types of interneuron, among them the basket cells, two different types of bistratified cells and stratum pyramidale-stratum radiatum interneurons have been analyzed and described in detail (Mercer et al., 2007, 2012a,b).

The CA2 region receives extrahippocampal projections stem from the lateral supramammillary nucleus (Haglund et al., 1984; Maglóczky et al., 1994; Cui et al., 2013), the entorhinal cortex layer II, the medial septal nuclei, vertical and horizontal limbs of the nucleus of the diagonal band of Broca, the median raphe nucleus and from the paraventricular nuclei of the hypothalamus (Cui et al., 2013). Efferent extrahippocampal projections target the medial and lateral septal nuclei, the vertical and horizontal limbs of the diagonal band of Broca, the supramammillary nuclei (Cui et al., 2013) and the medial entorhinal cortex layer II neurons (Rowland et al., 2013). Interestingly, this latter connection has been described to be monosynaptic (Rowland et al., 2013).

The exact anatomical pathways between entorhinal cortex and hippocampus are still under investigation. Regarding entorhinal cortex layer II there is a consensus that fibers from this layer project to the CA2 area. Whereas inputs to CA2 from the entorhinal cortex layer III were recorded in some publications (Chevaleyre and Siegelbaum, 2010; Jones and McHugh, 2011), in other work the input from layer II was investigated in isolation (Bartesaghi and Gessi, 2004; Bartesaghi et al., 2006) and in one recent study using an optogenetic approach the authors could not detect any inputs from layer III entorhinal cortex fibers (Kohara et al., 2014). Using specific tools future work will have to unequivocally define the projections from the entorhinal cortex arriving in CA2.

Synaptic input from the entorhinal cortex is provided onto the distal apical dendrites of CA2 pyramidal cells. Probably local dendritic sodium spikes and the dendritic geometry of CA2 pyramidal neurons are the required mechanisms that enable the distal dendritic inputs to drive action potentials in CA2 cells (Sun et al., 2014). This

synapse, in addition to be very strong, has also the property to undergo marked alterations in synaptic plasticity (Chevaleyre and Siegelbaum, 2010).

Intrahippocampal connections are described between both the dentate gyrus and CA2 and between CA3 and CA2. Via the mossy fiber pathway, dentate gyrus granule cells project onto CA2 neurons (Kohara et al., 2014; Llorens-Martín et al., 2015). Via the Schaffer collateral pathway, the CA3 region sends excitatory fibers to CA2, and this excitatory synaptic input is accompanied with strong feed-forward inhibition (Chevaleyre and Siegelbaum, 2010). Interestingly, this excitatory synapse can not be potentiated with the usually used stimulation protocols (Zhao et al., 2007; Chevaleyre and Siegelbaum, 2010) and the mechanism underlying this remarkable resistance against synaptic potentiation is probably based on the expression of RGS14 in CA2 pyramidal cells (Lee et al., 2010). Physiological doses of caffeine or adenosine A1 receptor antagonists are on the other hand able to potentiate the synapse between CA3 and CA2 pyramidal neurons in a long lasting manner (Simons et al., 2012), suggesting control of this synapse by ambient adenosine.

CA2 neurons strongly innervate CA1 neurons, preferentially the deep pyramidal cells in CA1 (Bartesaghi et al., 2006; Chevaleyre and Siegelbaum, 2010; Kohara et al., 2014). This indicates another cycle within the hippocampus adding to the classical entorhinal cortex-dentate gyrus-CA3-CA1 synaptic loop. In this cycle there is a direct activation of CA2 by the entorhinal cortex, followed by an activation of CA1.

A recent study investigated the function of CA2. The authors genetically inactivated the CA2 region in mice and observed a pronounced loss of social memory. The animals were not able to remember a conspecific but had normal spatial, sociable and contextual memory (Hitti and Siegelbaum, 2014). This loss of social recognition memory fits with the fact that in CA2 Avpr1b is highly expressed (see above) and that this receptor is involved in social recognition (Young et al., 2006).

Neurons of the supramammillary nucleus and CA2 pyramidal cells fire phase-locked to hippocampal theta rhythm indicating that the CA2 region plays an important role in this oscillation (Maglóczky et al., 1994).

However, the role of CA2 within the hippocampal network during ripples has not been investigated so far. SWRs probably are generated in the CA3 region and send a wave of activity to CA1 where the ripple oscillation is generated locally (Buzsáki et al., 1992; Maier et al., 2011). We were interested to shed light on the activation pattern within CA2 during ripples; therefore, we started with investigating synaptic activity in CA2 pyramidal cells during ripple oscillations.

In all experiments we determined the CA2 region host hoc with a PCP4 immunostaining; we observed an overlay of the mossy fiber tract with the CA2 area (Figure 4.1 (A) a, b, d, e, (B) a, b, d, e) in agreement with results shown by SanAntonio et al. (2014) and Kohara et al. (2014). For every recorded cell we verified the location in the CA2 area defined by PCP4 (Figure 4.1 (A) c, f, (B) c, d). The large cell body and the early bifurcating apical dendrite could be nicely observed as exemplified in the biocytin stainings in Figure 4.1 (A) c-f, and (B) c-f.

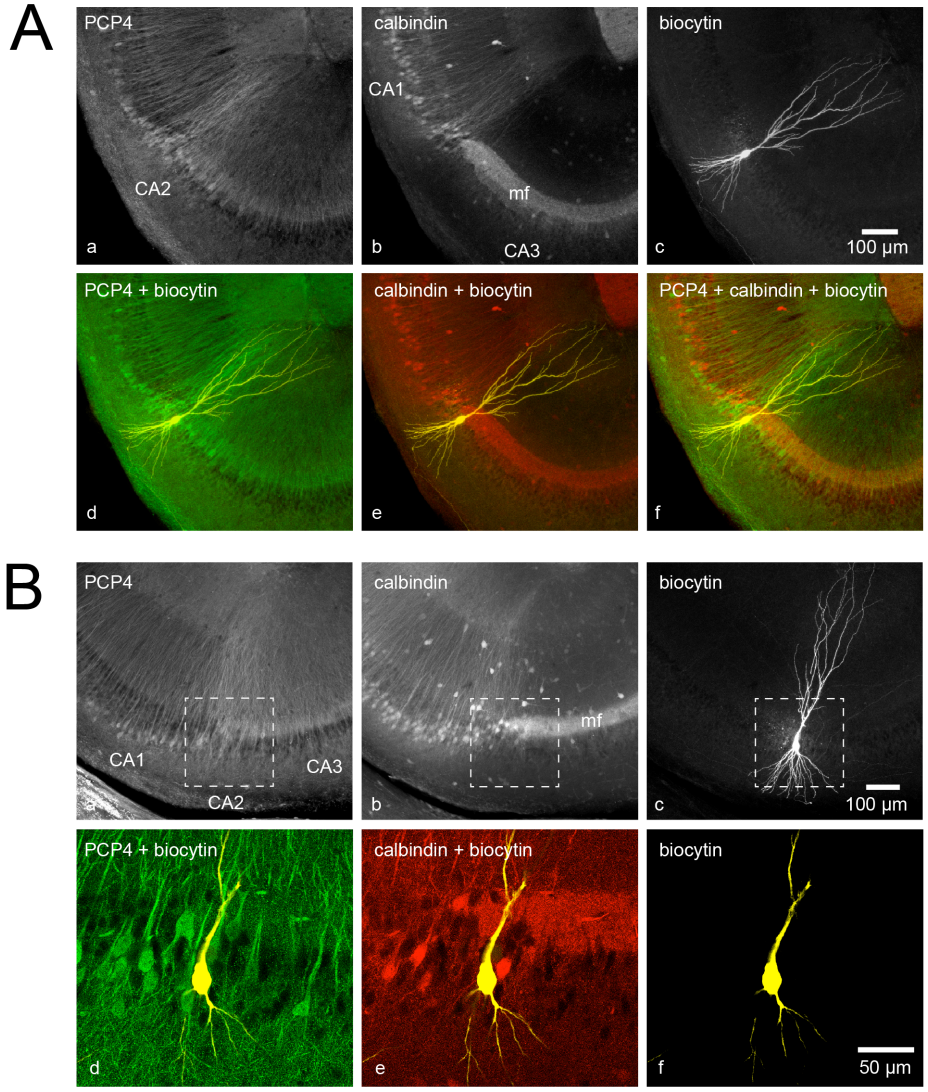

Figure 4.1 Post-hoc immunostainings confirm the localization of the recorded cells in the CA2 region. **(*A*)** Immunostaining against PCP4, calbindin and biocytin (*a-c*, respectively). The biocytin filled pyramidal neuron is located in the region of PCP4 positive cells (*d*), as well as on the border of the calbindin positive mossy fiber tract (*e*). Overlay of PCP4, calbindin and biocytin staining (*f*). **(*B*)** Same staining as in *A* from a different slice and recording (*a-c*). *d-f* show a larger magnification of the images *a-c* and the overlay with the biocytin filled cell. Note that a single confocal image plane is shown in images *d-f*.

4.2 Basic characteristics of SWR complexes in area CA2

To record SWRs in the CA2 area we positioned the LFP electrode in the pyramidal cell layer of CA2 as sketched in Figure 4.2 (A). An example of SWRs in area CA2 is shown in Figure 4.2 (B). In the right top panel the typical sharp wave with the superimposed ripple is displayed and in the right bottom panel the band-pass filtered signal highlights the ripple component. Figure 4.2 (C), left shows the mean values of

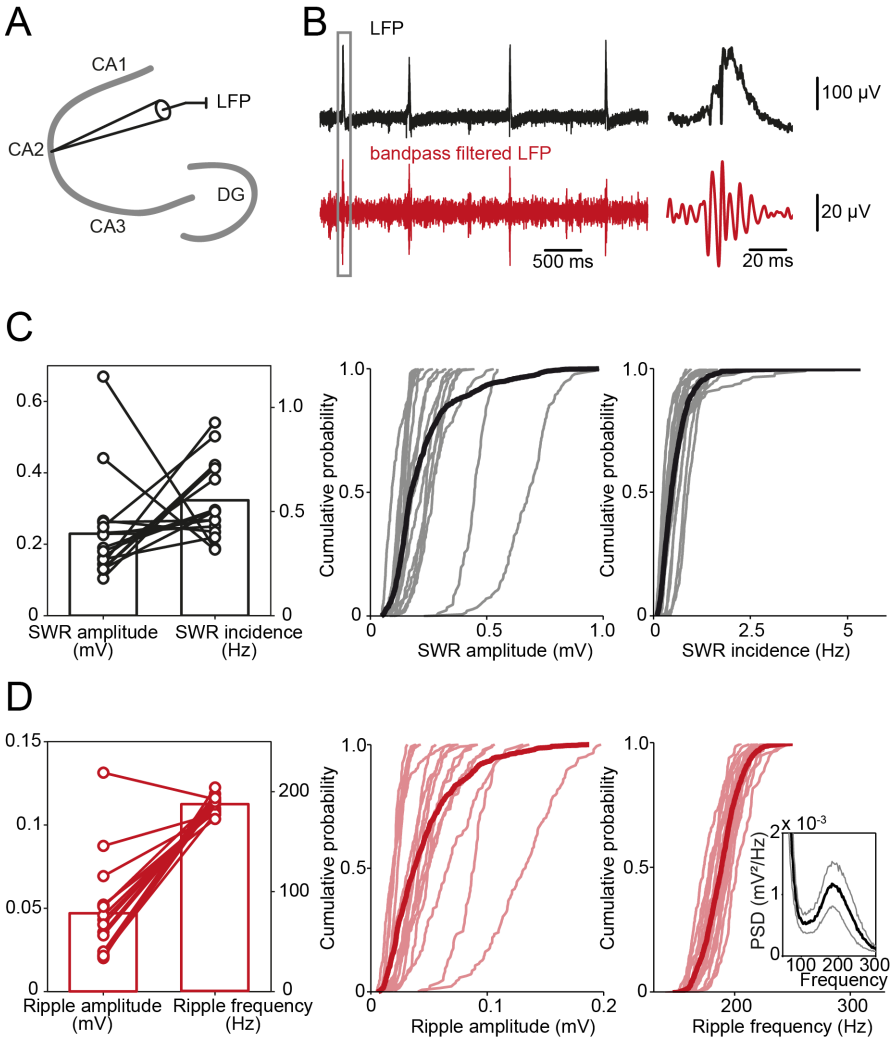

Figure 4.2 Extracellular electrophysiological description of SWRs in the CA2 area. **(*A*)** Schematic view of the recording position of the LFP in the pyramidal cell layer in the CA2 region. **(*B*)** Example trace of the LFP recording (black) and band-pass filtered (120-300 Hz) LFP (red). The *right* panels show an enlargement of the marked SWR event in the *left* panels. **(*C*)** The SWR amplitude and incidence of all 16 recordings in the CA2 region are shown. (*left*) The mean values over all SWRs (barplot) and the mean values of each single recording (open circles) are shown for the amplitude as well as the incidence. Note, there is no correlation between SWR amplitude and incidence. The cumulative plots show the distribution of amplitude (*middle*) and incidence (*right*) values in the single experiments (gray lines) and over all experiments (bold black line, 68 randomly selected events of each experiment, quartiles of SWR amplitude: Median: 175 µV, P25: 134 µV, P75: 263 µV; quartiles of SWR incidence: Median: 0.46 Hz, P25: 0.29 Hz, P75: 0.71 Hz). **(*D*)** Ripple amplitude and ripple frequency of the SWR events shown in (*C*) are displayed. Mean values of ripple amplitude and ripple frequency over all recordings (barplots) and mean values of each recording (open circles) were plotted (*left*). Cumulative plots show the distribution of ripple amplitude (*middle*) and ripple frequency (*right*) of each individual recording (light red lines) and of all recordings (bold red line, 68 randomly selected events of each experiment, quartiles of ripple amplitude: Median: 37 µV, P25: 23 µV, P75: 59 µV; quartiles of ripple frequency: Median: 186 Hz, P25: 174 Hz, P75: 198 Hz). The power density spectrogram for all ripple events of the 16 recordings is shown in the inset (gray lines indicate the SEM).

amplitude and incidence of the SWRs of single experiments and over all cells. The distribution of SWR amplitudes and average incidence values for single experiments and the distribution across all experiments are shown in Figure 4.2 (C), middle and right. The distributions of average ripple oscillation amplitude and frequency are

displayed in Figure 4.2 (D). As shown in Figure 4.2 (D) the power spectral density displays a clear peak at the ripple frequency of approximately 200 Hz.

4.3 Synaptic inputs recorded in CA2 pyramidal neurons during SWRs

In our recordings, all pyramidal neurons in CA2 received synaptic inputs during SWRs. Figure 4.3 (A) sketches the recording configuration with the LFP electrode in the pyramidal cell layer of area CA2 and the simultaneous whole-cell patch clamp recording of a CA2 pyramidal cell. An overlay of the reconstructed pyramidal neuron with calbindin and PCP4 staining is shown in Figure 4.3 (B). The pyramidal cell is clearly located within the region of PCP4 positive neurons and overlaps with the calbindin positive mossy fiber tract. The recorded cell was voltage-clamped at different holding potentials (Figure 4.3 (C)) and receives outward currents which appear stronger at potentials of -50 or -55 mV. Between -55 and -65 mV SWR-associated currents switch polarity indicating the SWR-associated reversal potential. At potentials more negative to -65 mV inward currents become increasingly larger in amplitude, consistent with increasing driving forces for both excitation and inhibition. The currents for each SWR-associated synaptic input were quantified and the mean synaptic currents were plotted against the holding potentials (Figure 4.3 (D)). We found a linear relationship between the holding potential and the amplitudes of the SWR-linked synaptic currents which allowed us to estimate the SWR-associated reversal potential of the pyramidal neuron (Figure 4.3 (D)). The distribution of SWR-associated reversal potentials had an average of -60.2 $\pm$ 4.7 mV (Figure 4.3 (E)). For all recorded cells, we plotted the mean SWR-associated synaptic currents at different holding potentials against the holding potentials and calculated the average SWR-associated reversal potential (Figure 4.3 (F)).

In the recordings for the SWR-associated reversal potential at the different holding potentials there is always a mixture of inhibitory and excitatory currents whereby the impact of the two components changes with different holding potentials. To differentiate between excitatory and inhibitory currents in a different set of experiments we used a cesium-based intracellular solution and clamped the cells close to the reversal potential of chloride to mainly record excitation and the reversal potential of excitation at +6 mV to isolate inhibition. In Figure 4.4 (A) a pyramidal neuron recorded under these condition is shown. The recorded biocytin filled and stained neuron is located in the area of PCP4 positive neurons and the whole-cell patch clamp recording from this cell was performed simultaneously with the LFP recording nearby the cell. An example of recorded mean SWRs and SWR-associated mean excitatory synaptic inputs for one cell is displayed in Figure 4.4 (B). Across cells, the mean cEPSCs of single cells show a large variation (Figure 4.4 (B)). In Figure 4.4 (C) an example of compound inhibitory synaptic currents in a CA2 pyramidal neuron is shown for one cell and the mean cIPSC value for each cell shows again a large variability of cPSCs between cells. The ratio between the excitatory

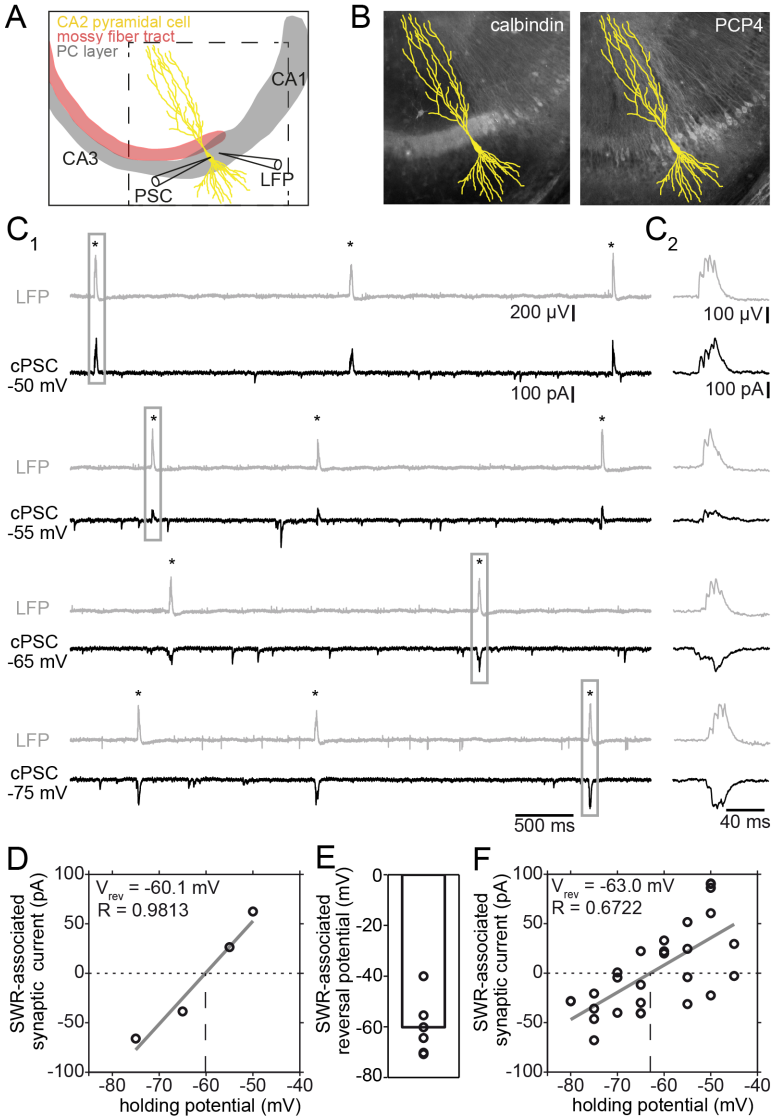

Figure 4.3 Compound PSCs in CA2 pyramidal neurons during SWRs. **(*A*)** Schematic of the recording configuration. Recording of PSCs of a CA2 pyramidal cell in the whole-cell patch clamp mode and simultaneous recording of the LFP nearby the cell in the CA2 region. **(*B*)** Overlay of the biocytin filled, reconstructed cell with the immunostaining for calbindin (*left*) and PCP4 (*right*). **(*C*)** Example traces of a simultaneous LFP and whole-cell patch clamp recording as shown in (*A*) at different holding potentials. (*C1*) Gray traces are the LFP recordings (asterisks mark the SWR events), black traces show the cPSCs corresponding to the SWR events. Events marked with a gray box are magnified (*C2*). **(*D*)** There is a linear correlation between the mean SWR-associated currents and the holding potential. For the example shown in (*C*) the SWR associated reversal potential is -60.1 mV. **(*E*)** The SWR-associated reversal potentials of individual linear regression fits for every single experiment are shown (open circles). Average SWR-associated reversal potential is displayed (bar plot, mean: -60.2 ± 4.7 mV). **(*F*)** From all 6 experiments the mean SWR-associated currents at the different holding potentials were ploted against the holding potential and a linear regression fit through all points were done. This fit result in a SWR-associated reversal potential of -63.0 mV.

and the inhibitory currents displays a similar variability between cells as for isolated excitatory and inhibitory currents (Figure 4.4 (D)). The cumulative distribution of cEPSCs and cIPSCs over all cells displays a large variability whereas the variation of each single cell has a much smaller distribution (Figure 4.4 (E)). For given cells,

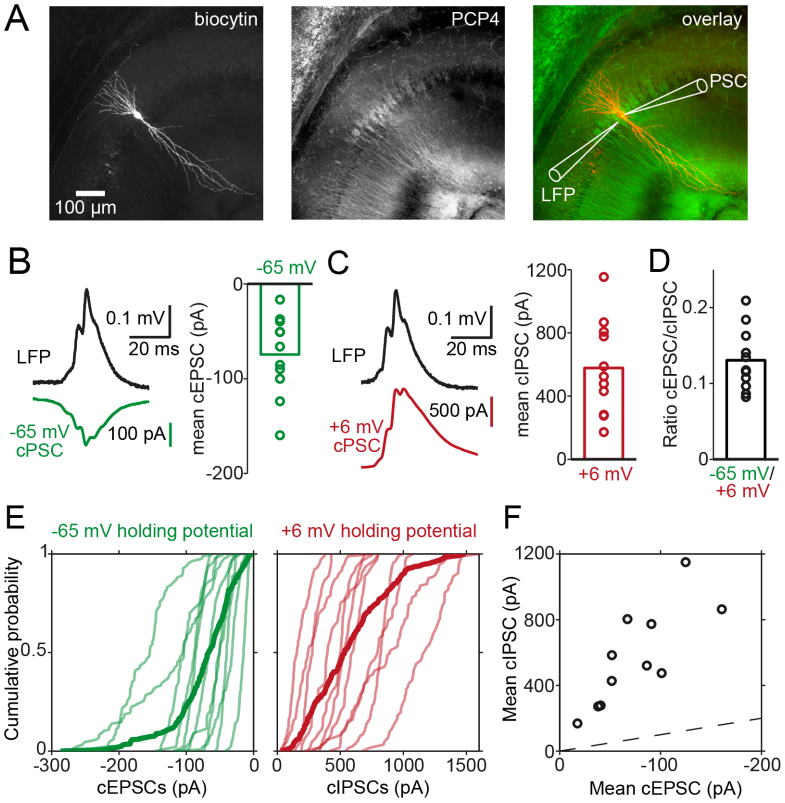

Figure 4.4 Separation and description of excitatory and inhibitory synaptic currents in CA2 pyramidal cells during SWRs. **(*A*)** Example of a recorded cell in the CA2 area. Staining of the biocytin filled recorded cell (*left*), immunostaining of the CA2 marker PCP4 (*middle*) and overlay of biocytin and PCP4 staining and indication of the recording configuration (*right*). **(*B*)** (*left*) Mean SWR (black) of all SWR events during the recording at the holding potential of -65 mV and mean cPSCs (green) of the same events of the recorded CA2 pyramidal neuron. (*right*) Open circles show the mean excitatory SWR-associated currents of 11 single experiments. The barplot represents the mean cEPSCs recorded close to the reversal potential for inhibition at -65 mV (mean = -74.6 ± 12.7 pA). **(*C*)** (*left*) Mean SWR (black) of all SWR events during the recording close to the reversal potential for excitation at +6 mV and mean cPSCs (red) of the same events of the recorded CA2 pyramidal cell. (*right*) Open circles show the mean inhibitory SWR-associated currents of all 11 single experiments. The barplot represents the mean cIPSCs recorded at +6 mV holding potential (mean = 578.2 ± 89.7 pA). **(*D*)** Ratio of mean cEPSCs divided by mean cIPSCs of every single experiment (open circles). The barplot represents the mean ratio over all cells (mean = 0.13 ± 0.04). **(*E*)** Cumulative plots of all events of each single experiment show the distribution of the cEPSCs (*left*, light green lines) and cIPSCs (*right*, light red lines). From each cell 30 events were randomly selected to show the distribution of cEPSCs (*left*, bold green line) and cIPSCs (*right*, bold red line) over all 11 cells. Quartiles for the distribution of cEPSCs in the CA2 pyramidal neurons (*left*, green): Median: -67.0 pA, P25: -69.4 pA, P75: -40.4 pA; for cIPSCs (*right*, red): Median: 533.6 pA, P25: 304.2 pA, P75: 792.2 pA. **(*F*)** The mean cIPSCs and mean cEPSCs are positively correlated (R = 0.7615).

we found a strong positive correlation for inhibitory and excitatory SWR-associated synaptic inputs (R = 0.76; Figure 4.4 (F)).

4.4 Timing of synaptic input into CA2 pyramidal neurons during ripple oscillation

The synaptic inputs into CA2 pyramidal neurons during SWRs display a superimposed fast component which can already be recognized in the raw signals. Band-pass filtering the synaptic inputs in the range of the ripple frequency (120 and 300 Hz) consistently revealed a strong ripple component over all individual events for excitatory as well as inhibitory synaptic inputs. The ripple component is not only visible in single events but could also be observed in the averaged signal suggesting a stereotypical time course of these synaptic inputs (Figure 4.5 (A1), and (A2), (B1), and (B2)). Besides the ripple component, the spectrogram also displays the slow time course of the underlying sharp wave. These two frequency components can be observed in spectrograms of single cells and of the average of cPSCs across the whole population of sampled CA2 pyramidal cells, both for excitatory and inhibitory currents (Figure 4.5 (A3), (A5), (B3), and (B5)). In line, power spectral density plots of single cPSCs and also of the average current display a peak at around 200 Hz (Figure 4.5 (A4), (B4)). However, this peak is variable with respect to amplitude or frequency within cPSCs of single neurons and across the population of analyzed cells (Figure 4.5 (A6), (B6)).

We compared the fast component of cPSCs in CA2 pyramidal cells with the ripple component of the LFP. For every single event the potentials of the LFP and the synaptic currents were band-pass filtered (120-300 Hz) and the phase of cPSCs with temporal reference to the LFP ripple was calculated (see 7.5 Data analysis). We analyzed the phases of currents recorded close to the reversal potential of chloride (-65 mV). An example of a single event is shown in Figure 4.6 (A1) and the calculated phase of 284.9° is displayed in the phase plot in Figure 4.6 (B1) as a thin black vector. The other events recorded in the same cell are plotted as gray vectors in the same plot and the bold black vector is the average vectors over all events (Figure 4.6 (B1)). Figure 4.6 (C1) shows the average vector over all recorded cells. The same analysis was done for the recordings at a more positive potential (-50 mV) to compare how inhibition in the mixed excitatory and inhibitory synaptic input will influence the phase with regard to the LFP. Figure 4.6 (A2) displays a single event and Figure 4.6 (B2) all events of the same cell and the average vector over all events. The difference between the average vector of the excitation and the average vector if inhibition is unmasked is 47° in the example cell (Figure 4.6 (B1) and (B2)). The average vectors over all recorded cells (Figure 4.6 (C1) and (C2)) display a phase difference of 57.8°.

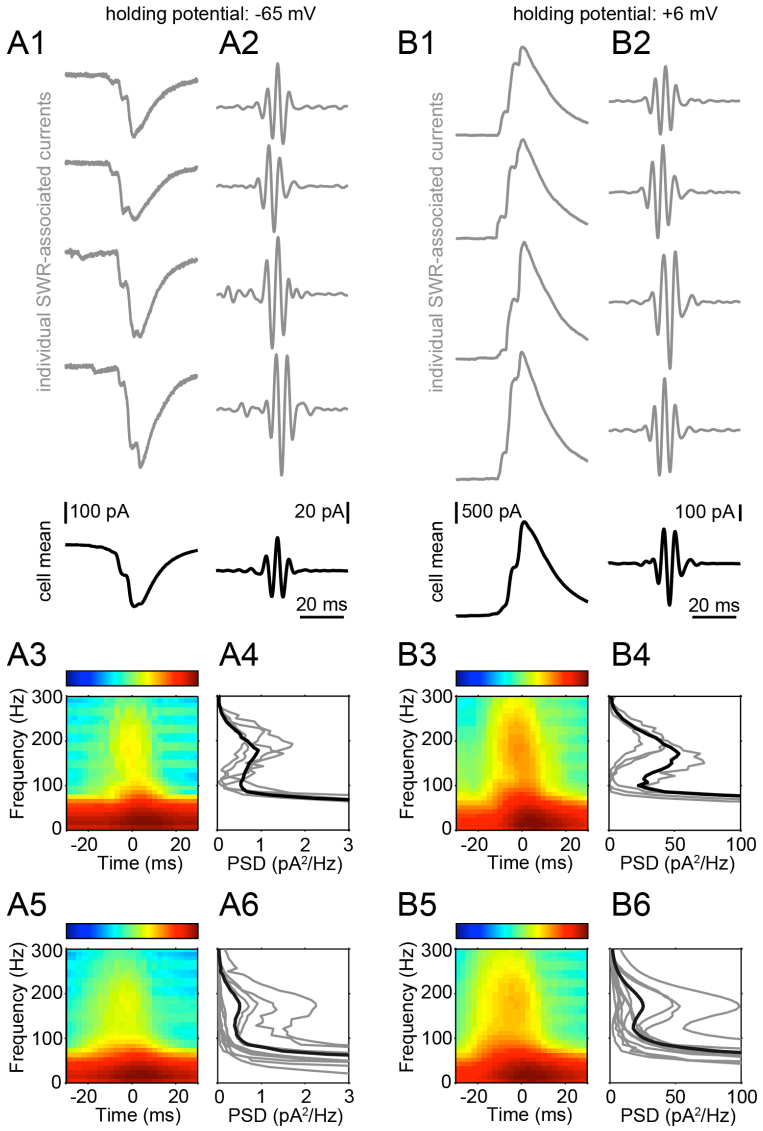

Figure 4.5 Fast synaptic input currents onto CA2 pyramidal cells during SWRs. **(*A*)** cEPSCs recorded close to the reversal potential for inhibition. (*A1*) Examples for individual SWR associated currents (gray) show small fluctuations of the current in the ripple frequency. (*A2*) Ripple component of the individual currents (gray) is clearly visible in band-pass filtered (120-300 Hz) currents of the examples in (*A1*). (*A1* and *A2*, *lower panel*, black) Display of the mean of all 48 SWR-associated currents of the example experiment recorded at a holding potential of -65 mV. (*A3*) Spectrogram of all 48 cEPSCs recorded at -65 mV holding potential. (*A4*) Power spectral densities of the individual cEPSCs (gray) shown in (*A1*) and averaged power spectral density (black) for all cEPSCs. (*A5*) Spectrogram of all cEPSCs of all 11 recorded cells. (*A6*) Averaged power spectral densities of all cEPSCs of each single cell (gray) and of all cEPSCs over all cells (black). **(*B*)** cIPSCs recorded close to the reversal potential for excitation at +6 mV holding potential. (*B1*-*B6*) Same as in (*A*). (*B1*, gray) Displayed individual cIPSCs recorded at a holding potential of +6 mV. Also in this inhibitory currents there are current deflections in the range of the ripple frequency noticeable. The band-pass filtered (120-300 Hz) cIPSCs show a strong ripple component (*B2*, gray). (*B1* and *B2*, *bottom panel*, black) Average cIPSC and average band-pass filtered (120-300 Hz) cIPSC of SWR-associated currents recorded in the example cell at +6 mV holding potential. (*B3*) Spectrogram of all SWR events in the example cell recorded close to the reversal potential for excitation. (*B4*) Power spectral densities of the individual cIPSCs (gray) shown in (*B1*) and averaged PSD of all 58 cIPSCs in the cell. (*B5*) Spectrogram of cIPSCs of all 11 recorded cells. (*B6*) Averaged power spectral densities of all cIPSCs of each single cell (gray) and of all cIPSCs over all cells (black).

4.5 Comparison of the timing of synaptic input into CA1 and CA2 pyramidal neurons during ripple oscillation

We first calculated the phases of synaptic inputs with respect to the LFP ripple in area CA1 for deep and superficial CA1 pyramidal cells separately. We found that, with respect to the LFP ripple, the average phase is later in superficial versus deep pyramidal cells (at -65 mV superficial vs. deep: 340.6° and 308.7°; at -50 mV superficial vs. deep: 231.2° and 199.3°). Together, there is a phase difference

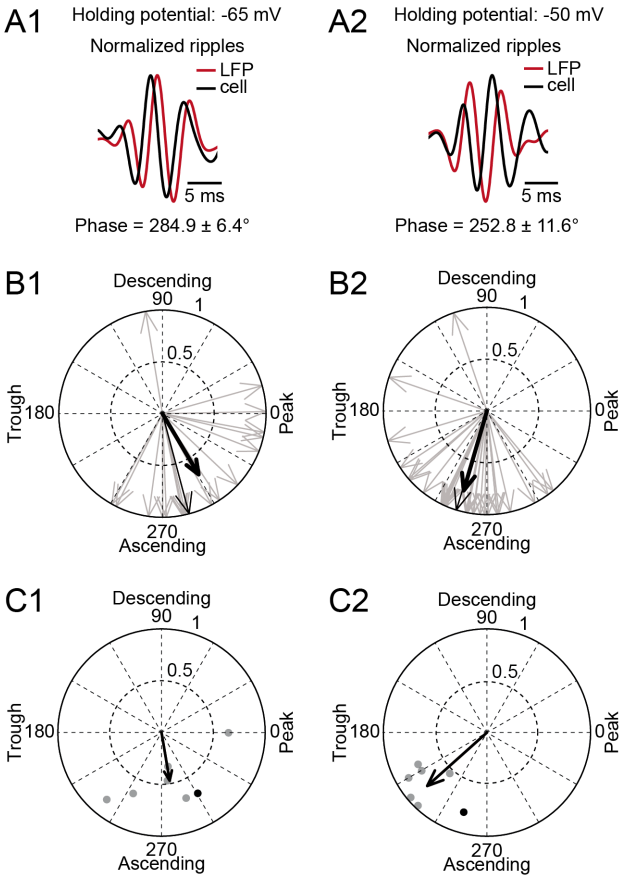

Figure 4.6 Phases of synaptic conductances of CA2 pyramidal neurons with respect to LFP ripples. **(*A*)** Example of the ripple component of a SWR event. Normalized ripples of the band-pass filtered (120-300 Hz) LFP (red) and the synaptic conductance (bp filtered at 120-300 Hz, black). The phase shift of the conductance with respect to LFP for an individual event at holding potential of -65 mV (*A1*, mean phase and estimation error: 284.9 ± 6.4°) and for a more positive holding potential of -50 mV (*A2*, mean phase and extimation error: 252.8 ± 11.6°). **(*B*)** Phases with respect to the LFP of all compound synaptic conductances recorded in the same cell as in (*A*). Gray vectors indicate individual events and the thin black vector displays the event shown in (*A*). Average vector (bold black) over all events in one cell recorded at -65 mV holding potential (*B1*, average vector: 300.8° with a vector strength of 0.67) and at -50 mV holding potential (*B2*, average vector: 253.8° with a vector strength of 0.8). **(*C*)** Display of the phases of synaptic conductances with respect to the LFP. Dots represent the phase and strength of average vectors from individual cells (black dot shows the average vector of the example in *B*) and the vector represents the average over all seven cells at a holding potential of -65 mV (*C1*, average vector: 279.6° with a vector strength of 0.47) and at a holding potential of -50 mV (*C2*, average vector: 221.8° with a vector strength of 0.77).

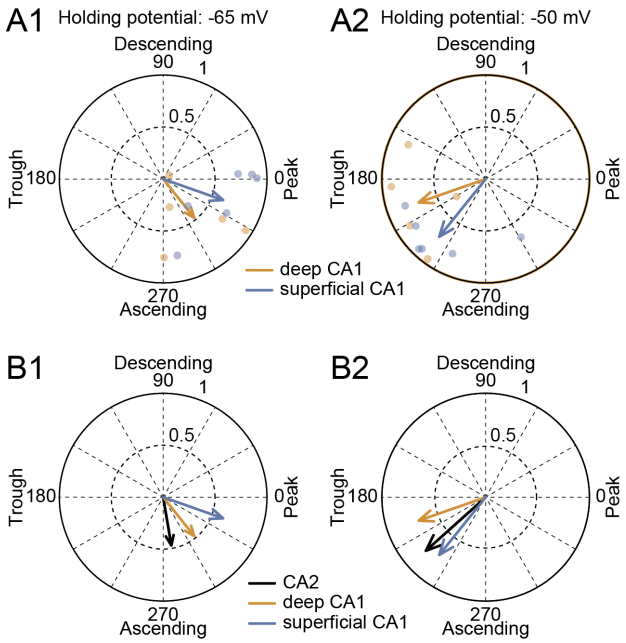

Figure 4.7 Phases of synaptic conductances with respect to LFP ripples of deep and superficial CA1 compared to CA2 pyramidal neurons. **(*A*)** Phases of compound synaptic conductances with respect to LFP. Dots represent the phase and strength of single-cell vectors (light orange: deep CA1 pyramidal neurons, light blue: superficial CA1 pyramidal cells) and vectors display the mean vectors over all five deep and six superficial cells (orange and blue, respectively). Phases of conductances in the recordings at -65 mV holding potential (*A1*, average vector, deep: 308.7° with a vector strength of 0.48, average vector, superficial: 340.6° with a vector strength of 0.61) and at -50 mV holding potential (*A2*, average vector, deep: 199.3° with a vector strength of 0.68, average vector, superficial: 231.2° with a vector strength of 0.71). **(*B*)** Comparison of phases of synaptic conductances with respect to the LFP between deep and superficial CA1 pyramidal cells and CA2 pyramidal cells at a holding potential of -65 mV (*B1*, average vectors: deep CA1: 308.7°, superficial CA1: 340.6°, CA2: 279.6°) and at a holding potential of -50 mV (*B2*, average vectors: deep CA1: 199.3°, superficial CA1: 231.2°, CA2: 221.8°).

between deep and superficial pyramidal cells of 31.9° for both the excitatory and mixed excitatory and inhibitory synaptic currents (Figure 4.7 (A1) and (A2)).

Due to the difference in inhibitory control received by deep and superficial CA1 and CA2 pyramidal neurons we were interested in whether we could observe any phase differences. The ripple oscillation in CA1 is a local phenomenon triggered by an excitatory drive from CA3 (Buzsáki et al., 1992; Maier et al., 2011). In CA2, so far, nothing is known about the origin of the ripple. However, in contrast to CA1, area CA2 receives strong feed-forward inhibitory input from CA3 and excitatory input from dentate gyrus granule cells. We found that, across recording conditions, phases of synaptic inputs were remarkably similar (Figure 4.7 (B1) and (B2)) especially for the mixed excitatory and inhibitory synaptic currents. In detail, for excitatory cPSCs recorded at -65 mV, we found phase differences of 29.1° in CA2 and deep CA1 pyramidal neurons and 61° in CA2 compared to CA1 superficial pyramidal neurons. For mixed excitatory and inhibitory cPSCs recorded at -50 mV, we found phase differences of 22.5° in CA2 and deep CA1 pyramidal neurons and 9.4° in CA2 compared to CA1 superficial neurons.

4.6 Discussion

The borders between the three parts of the *cornu ammonis*, CA1, CA2 and CA3, are defined in different ways. Historically, anatomical properties as differences in cell morphology and the termination of the mossy fiber tract were used to distinguish between the three areas (Lorente de Nó, 1934). However, recently, applying new methods of *in situ* hybridization and immunostainings the borders were redefined (Lein et al., 2005; San Antonio et al., 2014; Kohara et al., 2014). In our study we used immunostainings of the protein PCP4 to clearly define the CA2 area. PCP4 is strongly expressed in the hippocampus in CA2 pyramidal cells and also in dentate gyrus granule cells and has been applied as a marker to identify CA2 in several publications (Lein et al., 2005; San Antonio et al., 2014; Kohara et al., 2014).

All CA2 pyramidal neurons we recorded from receive excitatory and inhibitory cPSCs. As one characteristic of the CA2 cells during SWRs we recorded the SWR-associated reversal potential. These reversal potentials of CA2 pyramidal neurons showed a large variability. However in individual cells, the relationship between the cPSCs and the holding potential was strongly linear, rendering the estimation of the reversal potential very reliable. This indicates that the variability in the SWR-associated reversal potential over cells is not due to estimation errors but more likely to reflect a variability in the integration of CA2 pyramidal neurons into the network during SWRs. In line with this idea, excitatory and inhibitory cPSCs showed a large variability in strength across the recorded CA2 pyramidal cells and a much less variability of cPSCs between different SWR events within one cell.

Chapter 5

Discussion

An *in vitro* model of SWRs (Maier et al., 2009) was used to investigate the participation of different cell types in the network during SWRs. Even though the number of cell types we investigated is little compared with the number of cell types in the hippocampus the results are important. Complex interactions of different cells and cell types underlie SWRs. And our results can contribute to a better understanding of these interactions and give rise to further questions and investigations.

5.1 Recruitment of oriens-lacunosum moleculare interneurons during hippocampal ripples

Studying O-LM interneurons we found that O-LM cells spike during ripple oscillations. O-LM cells spike late with respect to the LFP SWR and these spikes are phase locked to the ascending phase of the LFP ripple. Only in 13 out of 22 O-LM neurons we observed spikes during SWR, but all 22 O-LM cells receive excitatory cPSCs. In line with the late spiking during ripple oscillations, also the excitatory synaptic input is late with respect to the LFP ripple and as it was observed for the spikes also the phase of the input is locked to the ascending phase of the ripple.

In contrast to our results obtained in slices, Klausberger (2003) found a reduction of spike probability of O-LM neurons during ripple oscillations. This behavior of the O-LM cells can potentially be explained by the anesthesia of the rats with urethane and ketamine. Indeed, in a more recent study, in head fixed awake mice the opposite behavior of the O-LM cells, an increase in firing rate during ripples, was shown (Varga et al., 2012).

5.1.1 Different spiking behavior of O-LM cells during sharp wave-ripple complexes

Additional to the explanations described in Chapter 2.5 regarding synaptic input and intrinsic cell parameters and slice properties there are two further possible explanations for the difference in spiking activity of O-LM cells. First, pyramidal cells projecting onto O-LM neurons express metabotropic glutamate receptors (mGluR), probably mGluR7. A persistent activation of these receptors leads to a reduction of EPSCs in O-LM cells (Shigemoto et al., 1996; Losonczy et al., 2003) and thereby also the excitatory currents during the ripple oscillation in the O-LM neurons are smaller and the neuron may not spike. Second, a recent study showed that O-LM cells are derived from two different origins, the caudal ganglionic eminence (CGE) and the medial ganglionic eminence (MGE). O-LM cells derived from the CGE only show the expression of the serotonin $(5\text{-HT})_{3A}$ receptor (Chittajallu et al., 2013). Interestingly, the study showed a stronger recruitment during gamma oscillations of O-LM cells derived from the MCE, which do not express the 5-HT_{3A} receptor. It is therefore feasible that the spiking O-LM cells in our study are also the MGE derived O-LM neurons. This might be an interesting question for future research on O-LM involvement in ripple oscillations.

5.1.2 Possible sources of the excitatory drive onto O-LM cells

O-LM cells receive their excitatory inputs primarily from pyramidal cells in the local CA1 network (Sik et al., 1995). It is known that these neurons spike only sparsely during ripple oscillation which raises the question where the strong excitation in the O-LM neurons originates from. Pyramidal cells spike sparsely and also irregularly during ripple oscillations but they fire together in clusters where other cells outside the cluster do not spike (Bähner et al., 2011; Brunel and Wang, 2003; Csicsvari et al., 2000). If an O-LM cell would receive excitation from a majority of cells of one of these spiking clusters the excitation would be strong enough to lead to O-LM cell firing despite the sparse firing of individual pyramidal cells. Another scenario is the following, based on an observation in the CA3 region. Pyramidal neurons in CA3 show more spikes in the axons than in the somata and these ectopic action potentials are probably isolated from the soma due to highly active axo-axonic cells. These cells inhibit the axon initial segment and prevent the traveling of the ectopic action potential to the soma (Dugladze et al., 2012). Supposing that these ectopic action potentials also exist in CA1, the active axons projecting to O-LM cells could provide the strong, phasic, and ripple locked excitation observed in these neurons. Models support this suggestion assuming coupled axon networks as a basis of ripple oscillations (Draguhn et al., 1998; Traub et al., 1999, 2012).

5.1.3 O-LM cells spike late during the ripple

With respect to the ripple maximum in the LFP the O-LM neurons receive excitatory currents mainly after the ripple maximum, and in line with the lagging excitation also spiking occurred late during the ripple. The delay could be caused by various reasons depending also on the origin of the excitatory currents in the O-LM cells. Assuming that the strong excitation in O-LM cells is based on clusters of sparsely spiking pyramidal neurons a possible explanation for the late arrival of the excitation could be a modulation of the output of the cluster projecting onto the O-LM cell by interneurons (Taxidis et al., 2012). In this case the O-LM neurons do not receive excitation at the beginning of the ripple oscillation because axo-axonic cells control the output of pyramidal cells by inhibiting the axon initial segment of pyramidal cells (Maccaferri et al., 2000; Somogyi et al., 1985). Due to the early activity of axo-axonic cells during the ripple oscillation, they spike mainly before the ripple maximum in the LFP and could be responsible for the late excitatory input into the O-LM neurons (Klausberger et al., 2003). In the alternative scenario, if we assume a coupled axon network with spikes independent of the soma as the origin of excitation in the O-LM cells, the activity of axo-axonic cells could not determine the late spiking because most of the spikes are independent from the axon initial segment of the pyramidal cells. However, the synapses between the presynaptic pyramidal cells and postsynaptic O-LM cells express properties which could explain the late firing. These synapses show a low initial release probability so that the O-LM neuron receives only small excitatory currents and the synapse show facilitation at the beginning of the ripple oscillation (McBain et al., 1994; Ali and Thomson, 1998; Losonczy et al., 2002, 2003; Biró et al., 2005). As a consequence, the excitatory currents in the O-LM cell become larger during the oscillation. An additional explanation that accounts for the late excitatory input onto O-LM neurons could be temporal summation of synaptic input.

5.1.4 What could be the functional significance of O-LM cell spiking during sharp wave-ripple complexes?

In our study we observed different levels of spiking activity of O-LM cells during ripple oscillations. This raises the question of the consequence of active or silent O-LM neurons. Due to their special morphology with cell body and dendrites in the stratum oriens and the axon branching in the stratum lacunosum moleculare, O-LM cells could have the function to gate the input from CA3 via the Schaffer collaterals and the input arriving from the entorhinal cortex layer III (Leão et al., 2012). Active O-LM cells inhibit the distal dendrites of pyramidal neurons in CA1 in the stratum lacunosum moleculare and disinhibit the feed-forward inhibition from CA3 by inhibiting interneurons in stratum radiatum. A consequence of these two sites of action is an enhancement of excitatory input from CA3 and along with this a reduced direct excitatory input from the entorhinal cortex due to O-LM cell activity (Leão et al., 2012). However, this gating theory suggested by Leão et al. is

not the only possibility regarding the function of O-LM cell activity. Other studies have shown a strong feed-forward inhibition from the entorhinal cortex layer III which leads to strong inhibitory currents in the pyramidal neuron as a consequence of entorhinal cortex activity. In this scenario the recruitment of O-LM cells would result in a disinhibition of this feed-forward inhibition in the stratum lacunosum moleculare and would result in a stronger impact of the excitatory input from the entorhinal cortex (Empson and Heinemann, 1995; Elfant et al., 2008). An additional role of O-LM neuron activity was described by Maccaferri (2000). They observed IPSCs in the soma of pyramidal cells as a result of O-LM cell activity and this would result in reduced pyramidal cell activity.

Irrespective of the above mentioned scenarios, O-LM cell activity during ripple oscillations might have an important impact in the gating of input from CA3 and the entorhinal cortex layer III and, by reducing the excitability of pyramidal cells, could also contribute to the termination of a ripple event.

5.2 Comparison of synaptic input in deep and superficial CA1 pyramidal cells during ripple oscillations

Probably the CA1 pyramidal neurons form different subgroups with different anatomical and physiological properties. One possibility to divide CA1 pyramidal neurons is to separate in deep and superficial pyramidal cells. To investigate if these two groups of cells display differences in their integration into the network during ripple oscillations we analyzed the synaptic input in deep and superficial CA1 pyramidal neurons during SWR.

5.2.1 Deep and superficial pyramidal cells have comparable ripple-associated compound EPSCs and IPSCs

It has been shown recently that PV basket cells inhibit deep pyramidal cells two to three times stronger than superficial pyramidal cells (Lee et al., 2014); therefore, it was of interest to have a separate measure of excitatory and especially inhibitory synaptic currents. In recordings where we separated the inhibitory and excitatory currents during the ripple oscillation we observed strong excitatory as well as strong inhibitory synaptic currents during each ripple event. In these experiments we did not observe any differences in either the strength of cEPSC or cIPSCs between deep and superficial pyramidal cells. We also recorded superficial and deep pyramidal cells at the same time to rule out the possibility of network changes over the recording time in sequential recordings. However also in this approach there was no consistent tendency for deep cells to receive more inhibition. In fact one example shows more

inhibition in the deep pyramidal cell but in the other example we observed the opposite effect or no differences.

Together, we did not observe strong differences in inhibition of deep versus superficial pyramidal cells during SWRs as described by Lee et al., 2014 for uIPSCs. The main difference is that we did not monitor isolated currents originating from PV basket cells because during ripples several populations of inhibitory neurons are active that contribute to cIPSCs recorded in pyramidal neurons. During SWRs different interneuron types are active. Beside PV basket cells (Klausberger and Somogyi, 2008; Varga et al., 2012; Forro et al., 2013), also O-LM cells (Varga et al., 2012; Pangalos et al., 2013; Forro et al., 2013), bistratified cells (Klausberger et al., 2004; Klausberger and Somogyi, 2008) and during some, but not all ripple events also CCK positive interneurons (Klausberger et al., 2005) show increased firing rates. It is known that CCK basket cells comparably inhibit the pyramidal neurons of the deep and superficial layer. Both cell groups receive the same strength of effective unitary IPSCs from the CCK basket cells (Lee et al., 2014). For the other interneurons active during ripples it is not known whether they differentially innervate deep and superficial pyramidal cells. For example bistratified interneurons are highly active during ripples. One possibility could be that these interneurons inhibit both the deep and the superficial pyramidal cells with the same strength. In this case, the effect of PV basket cells would be weakened. Another possibility could be that bistratified interneurons inhibit the superficial pyramidal cells stronger than the deep ones and thereby could counteract the PV basket cells.

5.2.2 Compound EPSCs and IPSCs are highly variable

As mentioned in Chapter 3.6 for the chloride reversal potential also for the cEPSCs and cIPSCs the distribution of values is broader in deep compared to superficial pyramidal cells. The same is evident in the data, published by Lee et al. (2014, their figure 1E). This leads to the possibility that the distinction between deep and superficial pyramidal cells is not the only way to classify the group of CA1 pyramidal cells. At least the deep pyramidal cell layer seems to consists of several subgroups. Perhaps the uniform group of pyramidal cells has to be divided into more specialized groups. Lee et al. (2014) also grouped pyramidal cells by their long-range projections and found differences in the uIPSCs from PV basket cells in the different groups. However, there are multiple other possibilities to differentiate between pyramidal cells. For example one could divide proximal and distal CA1 pyramidal cells, or there could be differences in pyramidal cells of the dorsal and the ventral pole of the hippocampus.

5.3 Analysis of synaptic inputs in pyramidal neurons in area CA2 during SWRs

5.3.1 CA2 neurons receive compound postsynaptic currents during SWRs

Within the hippocampus, the CA2 area is innervated by dentate gyrus granule cells (Kohara et al., 2014; Llorens-Martín et al., 2015), however, CA2 pyramidal neurons receive also strong feed-forward inhibition mainly from CA3 (Chevaleyre and Siegelbaum, 2010). Since SWRs probably are initiated in CA3 (Buzsáki, 1986; Buzsáki et al., 1992) it was not clear if the SWRs skip the CA2 area and directly travel from CA3 to CA1. However, in spite of these circuit properties, we observed SWRs in the CA2 region of all slices tested. It is difficult to estimate the recording area of an LFP electrode and given the fact that the CA2 region is very small there was the possibility that recorded signals were contaminated by CA1 or CA3. We could not rule out this possibility. However, in all intracellular recordings from CA2 pyramidal cells we observed excitatory as well as inhibitory synaptic inputs during SWRs, suggesting that the local network at least contributes to the LFP SWRs we recorded in CA2.

A further interesting result was that cells receiving large excitatory synaptic currents also receive large inhibitory synaptic currents during SWRs. One possible explanation of this phenomenon is that if the excitatory synapses are getting potentiated in one cell there is a counteracting process which also potentiate the inhibitory synapses. Another possibility is that there are more excitatory as well as inhibitory synapses in the CA2 pyramidal cells which receiving stronger currents during SWRs. Finally, it is in principle feasible that this difference is merely reflecting the recording depth, with more superficially recorded neurons receiving smaller synaptic inputs because of severed dendrites.

5.3.2 Phasic, ripple-locked compound postsynaptic currents

We found a strong phasic, ripple-locked component in both the excitatory and inhibitory cPSCs in pyramidal cells in area CA2. The phase of excitatory cPSCs was later with respect to the LFP ripple than the phase of a mixed excitatory and inhibitory currents. This could indicate two independent oscillators expressing different phases relative to the LFP ripple, with the inhibitory component leading the excitatory component.

Comparison of the phases of cEPSCs of CA2 pyramidal cells with the phases of cEPSCs of deep and superficial CA1 pyramidal neurons showed different phase relationships. The earliest phase for the cEPSCs could be observed in CA2 with respect to the LFP in CA2 followed by deep and finally superficial pyramidal neurons with respect to the LFP in CA1. The phases of the mixed cEPSCs and cIPSCs have

a different behavior. There is not a large difference between the phases of cIPSCs with respect to the respective LFP ripple.

Since the in vitro slice model of SWRs is a reduced system most likely without active synaptic inputs from entorhinal cortex or other brain regions to the hippocampus, the observed synaptic inputs in CA2 pyramidal neurons during ripples probably arise from area CA3 or from area CA2 itself. CA1 is innervated by CA3 and potentially CA2 in this experimental system. One could speculate that the excitation, which has an earlier phase in CA2 travels from CA3 via CA2 to CA1. If the area CA2 is interposed between region CA3 and CA1, this could also explain the different phases of cEPSCs of deep and superficial CA1 pyramidal cells because the deep pyramidal neurons are stronger innervated by CA2 than the superficial ones (Kohara et al., 2014). The inhibition which seems to have the same phase relationship to the LFP ripple in CA2 as in CA1 is either provided in both areas by feed-forward inhibition (Pouille and Scanziani, 2001; Maccaferri and Dingledine, 2002; Chevaleyre and Siegelbaum, 2010) or is generated in a feed-back mechanism by local and phase-locked interneurons in CA2 and CA1. Differences in phases of mixed cEPSCs and cIPSCs between CA1 deep and superficial pyramidal cells could be explained by stronger inputs of specific interneurons (Lee et al., 2014).

Chapter 6

Outlook

In the study described in Chapter 2 we demonstrated that O-LM neurons receive mainly excitatory input during SWRs. We analyzed the timing of this input with respect to the ripple oscillation in the field and we observed an action potential firing of the O-LM cells late during the SWRs. These results give rise to the question of the function of the O-LM cell spiking during the SWRs. In addition it is interesting to understand why about half of the O-LM neurons spikes during ripple oscillations and the other half is silent. With respect to the latter it would be important to study if the two different O-LM cells described by Chittajallu (2013) could explain the different spiking behavior of the O-LM neurons. The two types of O-LM interneurons in this study are derived from different origins and the CGE-derived O-LM cells express 5-HT_{3A} receptor whereas O-LM cells originate from the MGE never express this receptor. Activation of this receptor leads to an inward current in the CGE-derived O-LM cells and increases the firing probability of this O-LM type during gamma oscillation. As a first attempt regarding the spiking behavior of O-LM cells during SWRs, the application of the agonist at the 5-HT_{3A} receptor, 1-(3-chlorophenyl)biguanide hydrochloride (mCPBG), would be possible. In such an experiment an O-LM neuron which does not spike during the ripple should start spiking comparable to the CGE derived O-LM cells which increased their previously low firing probability during gamma oscillations after the application of mCPBG (Chittajallu et al., 2013). An other option would be to repeat recordings in the transgenic mouse which expresses green fluorescent protein (GFP) under the control of the 5-HT_{3A} receptor promoter, which is also used in the mentioned study.

The question of the functional relevance of the O-LM cell spiking during ripple oscillation requires more complex experiments. Leão et al. (2012) used a mouse which expresses the Cre recombinase specifically in O-LM cells in CA1 under the control of the promoter for the nicotinic acetylcholine receptor $\alpha 2$ subunit. This mouse could be used to inject the floxed version of different optogenetic channels and pumps in the ventral hippocampus. With archaerhodopsin-3 (Arch), a light-driven proton pump from the archaebacteria *Halorubrum sodomense*, it is possible to hyperpolarize cells with light of a special wave length (Chow et al., 2010). In contrast, with Channelrhodopsin-2 (ChR2), a light-gated ion channel from *Chlamydomonas rein-*

hardtii the cells could be depolarized and forced to elicit action potentials, again with light of a specific wave length (Nagel et al., 2003). Three weeks after the virus injection of either Arch or ChR2 it should be possible to detect the expression of the rhodopsins in the O-LM cells, and these infected O-LM neurons could be manipulated with light. Optogenetic hyperpolarization of the O-LM cells in a broad field in CA1 with a light pulse during ripple oscillations would lead to silencing of spiking O-LM cells during the oscillation. Several parameters of SWRs could be used to analyze the effect of the manipulation. The amplitude of the sharp wave, amplitude of the ripple, ripple length, ripple frequency and the incidence of SWRs are parameters which could be changed if the O-LM cells are removed from the active network. The opposite experiment to the expression of Arch is the expression of ChR2 in CA1 O-LM neurons. Light activation of infected neurons leads to spiking. Light activated action potential firing of the majority of O-LM cells during the ripple oscillation could also result in a change of parameters of SWRs. We collected preliminary data regarding these experiments, but could not observe any substantially effects of the O-LM cells and thus network manipulation.

To investigate the role of the recruitment of O-LM neurons in routing CA3 and entorhinal cortex input during ripple oscillations a system has to be chosen where the input from the entorhinal cortex is provided. Such an experimental system could be found in vivo. In vitro the input from CA3 via Schaffer collaterals is provided during ripple oscillations. However, it is difficult to stimulate electrically the entorhinal cortex input independent from other fibers projecting to CA1 stratum lacunosum moleculare. This problem has to be solved before a study of the O-LM neurons in the presence of this two inputs is possible in vitro during ripple oscillation.

In Chapter 3 we investigated the synaptic involvement of deep and superficial pyramidal neurons in CA1 in the network during ripple oscillations. Until now, in our recordings, we did not find any differences between deep and superficial pyramidal cells during SWRs. We performed all recordings in the ventral hippocampus where we can reliably record ripple events. Continuing with this study it would be possible to proceed in two different directions: One approach could be to do perforated patch experiments, which prevent the wash out of calbindin. This approach would enable to group the pyramidal cells according to positive or negative calbindin stainings. Differences between CB-positive and CB-negative pyramidal cells would become visible.

Another approach could be to identify functional subgroups in the pyramidal cell layer independent of their deep and superficial location, but with regard to the ripple oscillation. Based on the broad variability in all recorded excitatory and inhibitory synaptic inputs a cluster analysis would be useful. Parameters used for a cluster analysis could include (a) the strength of cEPSCs and cIPSCs, (b) the different long-range projections of CA1 pyramidal cells, (c) the location in the pyramidal cell layer with regard to the border to area CA2 and the subiculum and (d) different afferent fibers in the different parts of CA1.

We recorded SWRs in the area CA2 and analyzed the synaptic excitatory and inhibitory inputs in pyramidal neurons in this region (Chapter 4). As an approach for further investigations an experimental system would be interesting, where also the input from the entorhinal cortex is integrated. Maybe the application of a similar approach as used in the study by Kohara et al. (2014) would be possible. A separate optogenetic activation of fibers arriving from the entorhinal cortex layer II or layer III could influence the ripple oscillation in CA2 as well as in CA1. Together, the combination of modern techniques as optogenetics and the in vitro approach to SWRs will foster our understanding of the CA2 network in the context of SWRs, which might also help to form new ideas about the role of CA2 in general.

Chapter 7

Methods

7.1 Preparation of hippocampal slices

All experiments were carried out in accordance with local and national guidelines (Berlin state government, T0100/03).

For all experiments C57BL/6 mice at the age of 3 - 6 weeks were used. The mice were either decapitated or decapitated following isoflurane anesthesia. For the experiments in Chapter 2 (Recruitment of oriens-lacunosum moleculare interneurons during hippocampal ripples) the brains were quickly removed from the skull and transferred to standard artificial cerebrospinal fluid (ACSF, 1-4 °C), containing 119 mM NaCl, 2.5 mM KCl, 1.3 mM $MgCl_2$, 2.5 mM $CaCl_2$, 10 mM glucose, 1.0 mM NaH_2PO_4 and 26 mM $NaHCO_3$, equilibrated with carbogen [95 % (vol/vol) O2 and 5 % (vol/vol) CO_2], pH 7.4 at 37 °C, 290-310 mosmol/L. For all other experiments the brains were transferred to a sucrose-based ACSF (1-4 °C) for preparation containing 75 mM sucrose, 87 mM NaCl, 2.5 mM KCl, 7 mM $MgCl_2$, 0.5 mM $CaCl_2$, 25 mM glucose, 1.25 mM NaH_2PO_4 and 26 mM $NaHCO_3$, equilibrated with carbogen. For all experiments horizontal slices of ventral to mid-hippocampus were cut on a slicer (VT1200S; Leica) at 0.1 mm/s speed, 1.00 mm amplitude and 400 µm thickness. The slices were transferred to an interface chamber and stored at 32-34 °C, continuously oxygenized with carbogen and perfused with standard ACSF at ∼1 ml/min. Before the slices were transferred to the recording chamber they recovered at least 1 h after slice preparation.

7.2 Electrophysiology

All experiments were done in a submerged recording chamber (Maier et al., 2009). The chamber was perfused at high flow rate (5-6 mL/min) with standard ACSF at 31-32 °C. The different hippocampal areas and the different cell types were identified using infrared differential interference contrast (IR-DIC) video microscopy. Glass microelectrodes with a tip diameter of ∼5-10 µm and a resistance of 0.2-0.3 MΩ

were filled with standard ACSF and used either for LFP recordings or as stimulation electrodes. The LFP recordings were performed in the pyramidal cell layer of area CA1 (Chapter 2 and Chapter 3) or CA2 (Chapter 4) and were amplified 1,000 fold, filtered at 1-8 kHz and sampled at 5, 10 or 20 kHz. A Multiclamp 700A (Chapter 2) or Multiclamp 700B (Chapter 3 and Chapter 4) both from Axon Instruments were used to perform extracellular and whole-cell recordings. For parallel two-cell-and-LFP recordings, a custom-made two-channel extracellular amplifier was used. Cell-attached and whole-cell recordings were performed with borosilicate glass electrodes (2-5 MΩ) filled with different intracellular solutions depending on the experiment:

Figure 2.1 (A, B), 2.3-2.10, 3.2, 3.3, 4.3, 4.6, 4.7 (A), 7.1-7.3: 120 mM K-gluconate, 10 mM Hepes, 3 mM Mg-ATP, 10 mM KCl, 5 mM EGTA, 2 mM $MgSO_4$, 0.3 mM Na-GTP, and 14 mM phosphocreatine; pH was adjusted to 7.4 with KOH.

Figure 2.4: 120 mM Cs-fluoride, 10 mM KCI, 10 mM Hepes, 5 mM EGTA, and 1 mM disodium 4,4'-diisothiocyanatostilbene-2,2'-disulfonate (DIDS); pH was adjusted to 7.4 with NaOH.

Figure 2.1 (C) and Figure 2.2: 135 mM K-gluconate, 10 mM Hepes, 2 mM Mg-ATP, 20 mM KCl, 0.2 mM EGTA; pH was adjusted to 7.4 with KOH.

Figure 3.4, 3.4, 4.4, 4.5: 120 mM gluconic acid, 10 mM KCI, 2 mM $MgSO_4$, 3 mM Mg-ATP, 1 mM Na-GTP, 5 mM EGTA, 10 mM HEPES; pH was adjusted to 7.4 with 1 M CsOH.

7.2.1 O-LM cell identification

O-LM cells were identified by their horizontal orientation of oval somata and dendrites. Recorded O-LM cells were always $\geq$50 µm below the slice surface (range: 50-127 µm; median: 65 µm; 37 cells). The cells were recorded first in the cell-attached configuration and then the membrane was ruptured to perform the whole-cell configuration. For the analysis of the cell-attached data the first minute in this configuration was excluded. After performing the whole-cell configuration the cell was de- and hyperpolarized with current steps of 800-1000 ms and only cells with the characteristic spike pattern of O-LM neurons were included in further analyses. The series resistance was monitored throughout the whole experiment. Cells with a series resistance above 25 MΩ or with a variation of the series resistance of more than ±30 % were excluded from further analysis. All the potentials in Chapter 2 (Recruitment of oriens-lacunosum moleculare interneurons during hippocampal ripples) are corrected for the liquid junction potential which was calculated ($\sim$14 mV) and verified experimentally (data not shown).

7.2.2 Identification of deep and superficial CA1 pyramidal neurons

Pyramidal cells in the CA1 region were recorded in the pyramidal cell layer. Cells at the border to stratum oriens and to stratum radiatum were chosen to record from deep and superficial pyramidal cells respectively.

7.2.3 Identification of CA2 pyramidal neurons

Pyramidal cells in the area CA2 were also recorded in the pyramidal cell layer. The bigger size of the soma was used to distinguish between CA1 and CA2 neurons. The border to the CA3 region was more difficult to detect. The mossy fiber tract, which is visible in the IR-DIC optic was used as an indication. The border to the CA3 region is close to the end of the mossy fiber tract. The location of the cell in the area CA2 was confirmed in post-hoc stainings. PCP4 was used as a marker for the CA2 region and in combination with biocytin stainings the location of all recorded cells was verified.

7.3 Slice processing, immunohistochemistry and anatomical reconstruction

All cells were loaded with 0.3-0.5 % biocytin during the recording. The recorded slices were transferred to 4 % paraformaldehyde (PFA) and stored at 4 °C overnight. The PFA was exchanged by 0.1 M phosphate buffer (PB) the next day and slices were stored at 4 °C until the slices were further processed.

For biocytin stainings the slices were resectioned (100 µm) and rinsed extensively in 0.1 M phosphate buffer (PB) containing 0.9 % NaCl (PBS). Biocytin-filled cells were subsequently visualized with 3,3'-diaminobenzidine tetrahydrochloride (0.015 %) using a standard ABC kit (Vectorlabs) and reconstructed on a light microscope at 60× or 100× with a Neurolucida 3D reconstruction system (MicroBrightField, Williston, VT, USA).

For immunostainings in area CA1 (Chapter 3) the slices were resectioned (90 µm) and rinsed extensively in 0.1 M PBS. The sections were incubated in PBS containing 1 % Triton X-100 and 5 % normal goat serum (NGS; Vector Laboratories) at room temperature for 1 h. Slices were stained in a double immunofluorescent labeling for the biocytin-filled cells and calbindin. Therefore the sections were transferred to PBS containing 1 % Triton X-100, 2.5 % NGS, the streptavidin-conjugated Alexa Fluor 488 (1:500; Invitrogen) for the visualization of the biocytin-filled cells, and the CB-23 antibody (1:10000; Swant) at 4 °C for 48 h. Subsequently, sections were rinsed and then incubated in a secondary antibody (anti-rabbit-conjugated Alexa Fluor 594, Invitrogen) diluted at 1:500 in PBS containing 0.5 % Triton X-100 at room temperature. After 2h sections were rinsed extensively in 0.1 M PBS and

embedded in a fluorescent mounting medium (Fluormount; Sigma-Aldrich) under coverslips.

For immunostainings in area CA2 (Chapter 4) the slices were resectioned (90 µm) and rinsed extensively in 0.1 M PBS. The sections were incubated in PBS containing 1 % Triton X-100 and 5 % NGS at room temperature for 1 h. Slices were stained in a triple immunofluorescent labeling for the biocytin-filled cells, calbindin and the CA2 marker protein PCP4. Therefore the sections were transferred to PBS containing 1 % Triton X-100, 2.5 % NGS, the streptavidin-conjugated Alexa Fluor 647 (1:500; Invitrogen) for the visualization of the biocytin-filled cells, the CB 300 antibody (1:500; Swant) and the PCP4 antibody (1:200; Sigma-Aldrich) at 4 °C for 48 h. Subsequently, sections were rinsed and then incubated in a mixture of secondary antibodies (anti-rabbit-conjugated Alexa Fluor 488 and anti-mouse-conjugated Alexa Fluor 555, Invitrogen) diluted at 1:200 in PBS containing 0.5 % Triton X-100 at room temperature. After 2h sections were rinsed extensively in 0.1 M PBS and embedded in a fluorescent mounting medium (Fluormount) under coverslips.

Imaging of the cells was performed on a confocal laser-scanning microscope (Leica DM 2500, Chapter 3) or a STED microscope (Leica DMI 6000, Chapter 3 and Chapter 4).

7.4 Applied drugs

D-(-)-2-Amino-5-phosphonopentanoic acid (D-APV), 6-Imino-3-(4-methoxyphenyl)-1(6H)-pyridazinebutanoic acid hydrobromide (gabazine), and (2S)-(+)-5,5-Dimethyl-2-morpholineacetic acid (SCH 50911) were obtained from Biotrend. 2,3-Dioxo-6-nitro-1,2,3,4-tetrahydrobenzo[f]quinoxaline-7-sulfonamide (NBQX), disodium 4,4'-diisothiocyanatostilbene-2,2'-disulfonate (DIDS), and cesium fluoride were purchased from Sigma Aldrich.

7.5 Data analysis

The described data analysis algorithms in the following sections were developed for the study by Pangalos et al., 2013 and for this thesis. All of the following analysis was done using custom-made code in Matlab (MathWorks, Natick, MA).

7.5.1 Intrinsic cellular parameters

Directly after performing the whole-cell configuration in the recordings the resting membrane potential was estimated in the current-clamp mode.

For the calculation of the input resistance (R_i) during the experiment several test pulses with a 50 ms duration and a voltage step of $\Delta V = 4$ mV were applied and the resistance was calculated post-hoc on the basis of Ohm's law. The related

ΔI to the voltage step is the difference between the steady-state current and the baseline current before the voltage step. To calculate a reliable R_i first a window with a variable length to avoid spontaneous synaptic currents to be integrated in the analysis was implemented for the estimation of the baseline and the steady state current. Second, the SEM of ΔI was built by error propagation of the baseline- as well as the steady-state current SEM. The ΔI of measurements where the SEM exceeded 15% was excluded.

The action potential threshold was defined as the voltage where the positive slope dV/dt exceeded 20 mV/ms and was calculated from rheobase recordings where positive current injections were just strong enough to elicit action potentials.

7.5.2 Detection of sharp wave-ripple complexes

The SWR detection was performed by a threshold based algorithm (Wilson and McNaughton, 1994). The LFP and the related currents in a window of $\pm$100 ms around the maximum of the LFP SWR were cut out after the detection.

7.5.3 Amplitude of SWR and ripple events

The SWR amplitude was calculated as the maximum amplitude in this SWR. For the calculation of the ripple amplitude the data were first band-pass filtered (Chapter 2: 127-300 Hz; Chapter 3 and Chapter 4: 120-300 Hz). In a second step the hilbert transform was applied and the ripple amplitude was calculated by the maximum of the absolute part of the transformed signal.

7.5.4 Input calculation

In a first step to analyze the synaptic input, the SWR events were detected and cut out (see 7.5.2 Detection of sharp wave-ripple complexes). Next, the average synaptic input currents were detected. In contrast to the calculation of electric charge, for the calculation of the average synaptic input current also the duration of the synaptic input was included. The following algorithm was applied: First, 1$\times$ the SD of all baseline corrected events of the recording was calculated. In a second step, a smaller window ($\pm$50 ms) around the SWR maximum was cut out and every single cPSC was rectified and smoothed (moving average filter with a 10 ms window) as shown in Figure 7.1 (A1) and (A2). The time between the crosspoints of the smoothed signal and the 1$\times$ SD was defined as Δt (Figure 7.1 (A3)). The area under the curve (A) was calculated and in a last step this area was divided by the duration of the input (Δt) (Figure 7.1 (A4)). For O-LM neurons different detection thresholds for the quantification of the input duration were compared. The calculation for the spiking and nonspiking O-LM cells were repeated for the recordings at -74 mV except of the 1$\times$ SD also with 2$\times$ SD and with 20% from peak (Figure 7.1 (B1)-(B3)). A change in the absolute values for the input currents was found, however not in the basic

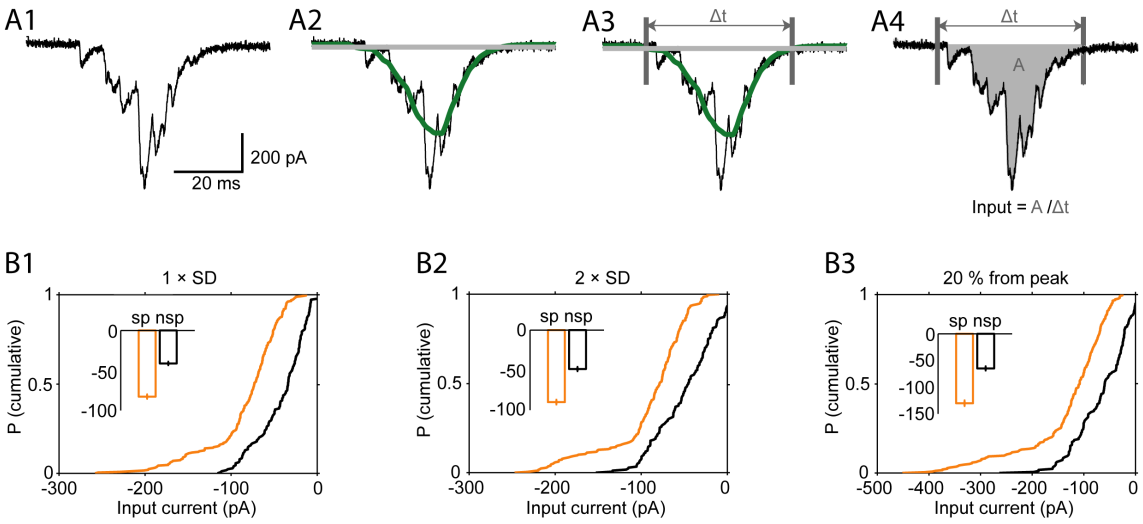

Figure 7.1 Estimation of average synaptic input currents during ripples and validation of the applied threshold criterion to estimate the signal width. (*A1*) Example of ripple-associated synaptic input in an O-LM neuron after offset correction. (*A2*) The green trace represents the inverted and smoothed (moving average filter; 10 ms time constant) version of the root-mean-squared original input current; the averaged SD of all current traces of the cell is given by the gray horizontal line. (*A3*) The width Δt of the signal was determined as the time difference of the intersections of the smoothed signal (green line) and the grey line. (*A4*) Finally, the average estimated synaptic input current is quantified by dividing the time integral of the current trace (area A under curve) by the width Δt of the signal. (*B1*) Distributions of average synaptic input currents for spiking (orange) and silent (black) O-LM neurons with 1× the averaged SD. The inset shows the mean values. The plot is identical to that displayed in Figure 2.9 (B). The same analysis was applied on the same data but different criteria were used to determine the signal width, i.e., 2× SD (*B2*) and 20% of event peak (*B3*). For all tested thresholds, highly significant differences were found for spiking and nonspiking O-LM neurons (K-S test P values: 1.6×10^{-24} (*B1*), 5.7×10^{-18} (*B2*), and 1.0×10^{-15} (*B3*)).

finding, which corroborates that the spiking O-LM neurons receive more excitatory input.

7.5.5 Estimation of the reversal potential of chloride

For the estimation of the reversal potential of chloride in O-LM interneurons and pyramidal cells experiments were performed in the presence of antagonists for AMPA/ kainate-, NMDA-, and GABAB receptors to isolate GABAA receptor-mediated currents. During extracellular stimulation O-LM or pyramidal cells were recorded at different holding potentials. From these recordings the reversal potential was calculated, i.e. the potential at which no synaptic currents could be observed. As a first step in this analysis the current amplitudes were calculated at the different holding potentials at the time point of the maximum current in the recording at a more positive holding potential (Figure 7.2 (A)). In O-LM cells the recorded currents show an inward rectification wherefore the two points below and above the zero line were plotted and the associated zero crossings were calculated. The mean of these revealed a value of V_{rev} = -76.8 mV (Figure 7.2 (B)). In addition, three other ways were tested to calculate the reversal potential (Figure 7.2 (C1)-(C3))

with only slightly different results. The recorded currents in pyramidal cells showed no rectification in contrast to those in O-LM neurons.

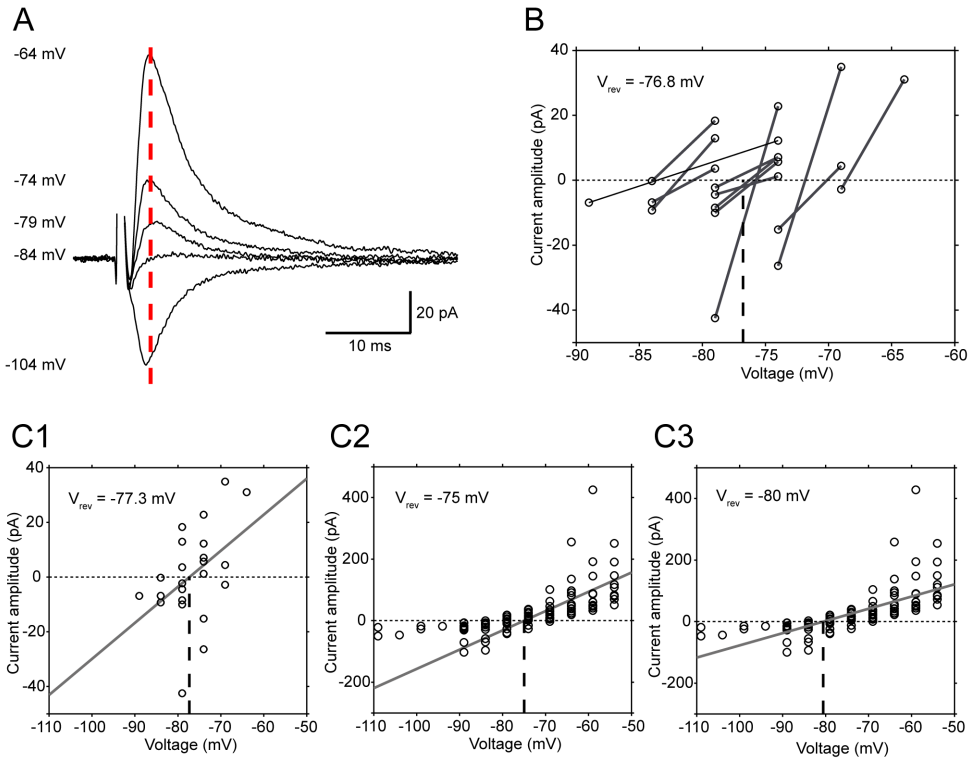

Figure 7.2 Estimation of the reversal potential of inhibition in O-LM cells in area CA1. (*A*) Examples of evoked synaptic currents in an O-LM interneuron voltage-clamped at different holding potentials in the presence of antagonists for AMPA/kainate-, NMDA-, and GABAB receptors (20 µM NBQX, 50 µM D-APV, and 20 µM SCH 50911). The dashed red line refers to the time point of the signal peak at -64 mV and gives the reference at which current amplitudes were determined for other holding potentials. For display, the stimulus artifact was truncated. (*B*) The first amplitude values below and above 0 pA were plotted against their respective holding potential (12 cells). Solid lines indicate the corresponding point-pairs. The vertical dashed line represents the mean for all zero crossings and hence, the average experimentally determined reversal potential of Cl^- (V_{rev} = -76.8 mV). (*C*) Different ways to determine the Cl^- reversal potential were additionally tested. Panel *C1* displays the linear regression fit through the same values as shown in panel (*B*, dashed line, V_{rev} = -77.3 mV). (*C2, C3*) Inspection of postsynaptic current amplitudes recorded below V_{rev} demonstrated outward rectification of IPSCs in O-LM neurons. Linear regression fit through only values $\geq$ -74 mV (*C2*) and through all data points (*C3*) illustrates the bias towards negative reversal potentials by outward rectification. To determine the V_{rev} in O-LM neurons, the method shown in panel *B* was applied.

7.5.6 Calculation of the SWR associated reversal potential

First, the input currents at the different holding potentials were calculated. To estimate the SWR associated reversal potential the input currents were plotted against the related holding potentials and a linear regression were fitted. The estimation was done with two different approaches. On the one hand the mean was calculated from the input currents of all cells of a group at one holding potential. A linear regression was fitted through all mean values and the zero crossing of the fitted line gives the SWR associated reversal potential for the cell population. On the other hand in

a second approach the SWR associated reversal potential was calculated for every individual cell. For this approach the calculated input currents were against the related holding potentials for every cell and the linear regression was fitted. Again the zero crossing of the fitted line gives the SWR associated reversal potential, but for the single cell, not for the whole-cell population. In this case the SWR associated reversal potential for the whole population was calculated as the mean value of the reversal potentials for the single cells.

7.5.7 Phase and envelope analysis

For the analysis of the phases and envelopes of individual ripple epochs, the detected SWR events were further analyzed in several steps. The excitatory ripple-associated synaptic currents were inverted to estimate the underlying conductances and analyze the timing of synaptic inputs. The single LFP events as well as the related conductances were band-pass filtered with a second order Butterworth filter with cut-of frequencies of 127 and 300 Hz. Using the Hilbert transform applied on these filtered signals the envelopes were calculated for all pairs of LFP and conductance events. An example of a filtered LFP ripple and its current-derived conductance trace, together with their overlaid envelopes are shown in Figure 7.3 (A).

To ensure that the conductance is linked to the LFP ripple only events were included, where the maximum of the conductance envelope was found within a temporal window of 40 ms centered to the maximum of the envelope of the LFP ripple. This requirement fulfilled 92 $\pm$ 1% of all events of the recordings.

A Hilbert phase plot of an example LFP ripple and its associated conductance traces are shown in Figure 7.3 (B). The next step included the subtraction of the conductance- from the LFP-Hilbert phase signals, resulting in a function that describes the phase difference of both signals over time (Figure 7.3 (D)). The time point of the maximum overlap of the envelopes of LFP ripple envelope and conductance was chosen as signature of the phase difference of both signals for the given ripple (Figure 7.3 (C) and (D)). Around this point in time the phase difference is relatively constant and the fluctuations in a time window of 7 ms around the point were used to estimate the reliability of the calculated phase. The indicated error (Figure 7.3 (D)) is then defined as the root mean square of the deviation from the estimated synaptic input phase. The 7 ms window is calculated from O-LM cell data from Figure 2.3 (B) and represents the time between the half-peaks of the LFP and conductance envelope.

In this last steps of the analysis all events were excluded where the maximum of the envelope either of the LFP or of the conductance is smaller than 3 times their baseline value. An additional criterion was applied to exclude signals where the phase envelope peaks were too distant in time ($>$ 20 ms); altogether, a total of 76.4 $\pm$ 3.5 % of all events in this set of experiments were analyzed.

Finally, for each recorded neuron, an average phase-vector was calculated. Mathematically, such a vector can be characterized by its phase angle and its vector

strength. A mean phase of vectors with the corresponding SEM as well as the average vector for the polar plots was estimated for all cells.

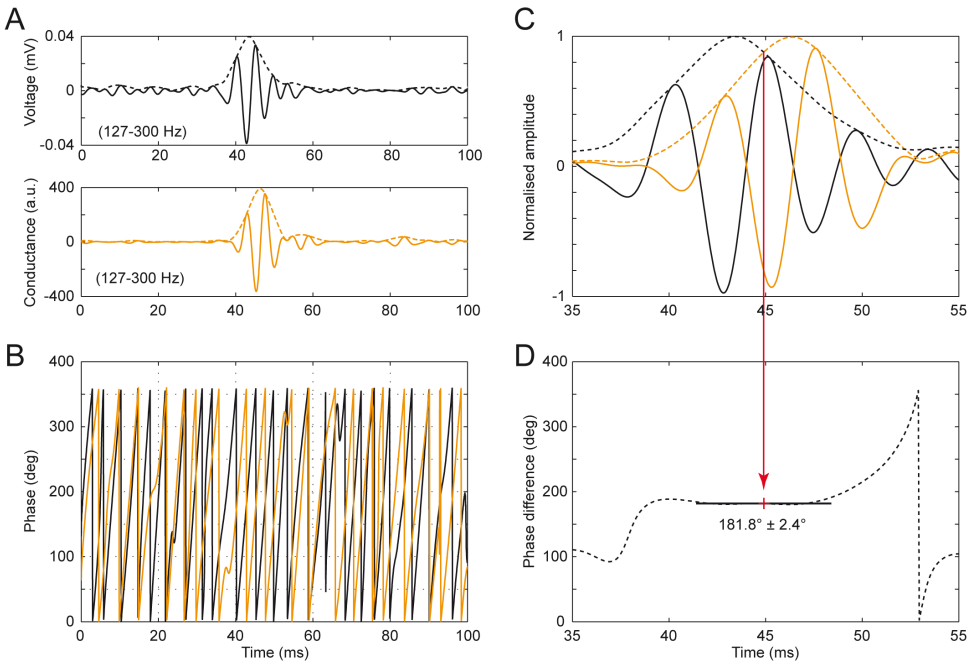

Figure 7.3 Phase and envelope analysis. (*A*) Ripple component (127-300 Hz, band-pass filtered) of both LFP (top, black) and excitatory cPSC-derived conductance (bottom, orange) overlaid with the respective envelopes derived from their Hilbert transforms. (*B*) Hilbert phase of the signals shown (*A*); black: LFP; orange: conductance. (*C*) Magnification and overlay of the normalized signals shown in panel *A*. (*D*) Phase difference trace (dashed black line). The dashed line is obtained by subtracting the phase of the conductance (orange trace in *B*) from the phase of the LFP (black trace in *B*). The phase of synaptic input was estimated by determining the phase difference at the point of maximum envelope overlap as depicted in panel *C* (red arrow). The phase estimation error is obtained from the deviations of the phase trace from the sampled value within a window of 7 ms (black horizontal line). For this particular example the phase estimate was 181.8° ± 2.4°.

7.5.8 Detection and timing of spikes

The time at which a spike occurs was estimated with temporal reference to the maximum of the ripple LFP's envelope in a time window of 120 ms surrounding that maximum. The detection algorithm differed slightly for the different recording conditions: In the current-clamp condition a threshold was used to identify spikes and the time point of the maximum of slope in the ascending phase of the action potential was taken as the time-stamp of the spike. For the cell-attached recordings the raw traces were filtered with a band-width of 0.5-1.5 kHz and the spike had to overshoot the 4×SD of the baseline in the raw as well as the filtered trace. The time point of the spike was determined by the trough of the action current. In Figure 2.5 (B) and Figure 2.4 (C2) the smoothed histogram profiles are constructed by first substituting each spike with a Gaussian kernel ($\sigma = 3.7$ ms) and then adding all the resulting kernels.

After the detection, the spike phase with respect to the LFP ripple was calculated. For this calculation, as for the estimation of the input phase, the Hilbert phase of the LFP ripple was used. The spike phase was estimated by the Hilbert phase of the LFP at the time point of the spike. For this calculation two requirements had to be met: First, the spike had to occur in a time window of 40 ms surrounding the maximum of the LFP envelope. And second, the envelope at the time point of the spike had to be larger than 2× the mean Hilbert envelope outside the SWR.

The average spike phase and for each cell the amount of phase locking were calculated. The latter was estimated by the mean resultant length of phase distribution, i.e. the vector strength.

7.5.9 Spectrogram representation

The spectrograms in Figure 4.5 (A3, A5, B3, B5) were build by the MATLAB function "spectrogram" using short-time Fourier transform. Parameters used in this function were the Hamming window (window = 500), the number of overlapping segments that produces 50 % overlap between segments (noverlap = 450), the FFT length (nfft = 2,048) and the sampling frequency (fs = 20,000).

7.5.10 Power spectral density analysis

Spectral analysis of SWRs was computed on stretches of 160 ms ((Figure 2.1 (C)), 400 ms (Figure 4.2 (D)) or 140 ms (Figure 4.5 (A4, A6, B4, B6)) of raw data centered on the SWR peak, using the Fast Fourier Transform (FFT) algorithm. Frequency resolution of all the resulting PSD plots was 10 Hz. Peaks of power line hum (50 Hz) and its harmonics were removed if necessary.

7.5.11 Coherence analysis

The coherence $C_{xy}(f)$ of two signals x and y is defined as their normalized cross-spectral density. The coherence was calculated using PSDs by the Welch periodogram method (2,048 FFT points).

7.5.12 Statistics

Data are reported as mean ±SEM, which is also indicated by error bars in the figures. Instead of the SEM and the error bars the single cell values are plotted in addition to the mean value in some figures. Statistical significance was assessed using the rank-sum, the two-sample Kolmogorov-Smirnov (K-S) or the Kuiper's test (Berens, 2009) at the given significance level (P).

References

Acsády, L., Görcs, T. J., and Freund, T. F. (1996). Different populations of vasoactive intestinal polypeptide-immunoreactive interneurons are specialized to control pyramidal cells or interneurons in the hippocampus. *Neuroscience*, 73(2):317–334.

Ali, A. B. and Thomson, A. M. (1998). Facilitating pyramid to horizontal oriens-alveus interneurone inputs: dual intracellular recordings in slices of rat hippocampus. *The Journal of physiology*, 507 (Pt 1):185–199.

Andersen, P., Morris, R., Amaral, D., Bliss, T., and O'Keefe, J. (2006). The Hippocampus Book.

Arszovszki, A., Borhegyi, Z., and Klausberger, T. (2014). Three axonal projection routes of individual pyramidal cells in the ventral CA1 hippocampus. *Frontiers in Neuroanatomy*, 8.

Axmacher, N., Elger, C. E., and Fell, J. (2008). Ripples in the medial temporal lobe are relevant for human memory consolidation. *Brain : a journal of neurology*, 131(Pt 7):1806–1817.

Bähner, F., Weiss, E. K., Birke, G., Maier, N., Schmitz, D., Rudolph, U., Frotscher, M., Traub, R. D., Both, M., and Draguhn, A. (2011). Cellular correlate of assembly formation in oscillating hippocampal networks in vitro. *Proceedings of the National Academy of Sciences of the United States of America*, 108(35):E607–16.

Baimbridge, K. G., Peet, M. J., McLennan, H., and Church, J. (1991). Bursting response to current-evoked depolarization in rat CA1 pyramidal neurons is correlated with lucifer yellow dye coupling but not with the presence of calbindin-D28k. *Synapse (New York, N.Y.)*, 7(4):269–277.

Bannister, N. J. and Larkman, A. U. (1995). Dendritic morphology of CA1 pyramidal neurones from the rat hippocampus: I. Branching patterns. *The Journal of comparative neurology*, 360(1):150–160.

Baraban, S. C. and Tallent, M. K. (2004). Interneuron Diversity series: Interneuronal neuropeptides–endogenous regulators of neuronal excitability. *Trends in neurosciences*, 27(3):135–142.

Bartesaghi, R. and Gessi, T. (2004). Parallel activation of field CA2 and dentate gyrus by synaptically elicited perforant path volleys. *Hippocampus*, 14(8):948–963.

Bartesaghi, R., Migliore, M., and Gessi, T. (2006). Input-output relations in the entorhinal cortex-dentate-hippocampal system: evidence for a non-linear transfer of signals. *Neuroscience*, 142(1):247–265.

Bartos, M., Vida, I., Frotscher, M., Meyer, A., Monyer, H., Geiger, J. R. P., and Jonas, P. (2002). Fast synaptic inhibition promotes synchronized gamma oscillations in hippocampal interneuron networks. *Proceedings of the National Academy of Sciences of the United States of America*, 99(20):13222–13227.

Berens, P. (2009). CircStat: A MATLAB Toolbox for Circular Statistics.

Biró, A. A., Holderith, N. B., and Nusser, Z. (2005). Quantal size is independent of the release probability at hippocampal excitatory synapses. *Journal of Neuroscience*, 25(1):223–232.

Botcher, N. A., Falck, J. E., Thomson, A. M., and Mercer, A. (2014). Distribution of interneurons in the CA2 region of the rat hippocampus. *Frontiers in Neuroanatomy*, 8:104.

Bragin, A., Engel, J., Wilson, C. L., Fried, I., and Buzsáki, G. (1999). High-frequency oscillations in human brain. *Hippocampus*, 9(2):137–142.

Brunel, N. and Wang, X.-J. (2003). What determines the frequency of fast network oscillations with irregular neural discharges? I. Synaptic dynamics and excitation-inhibition balance. *Journal of neurophysiology*, 90(1):415–430.

Buhl, E. H., Halasy, K., and Somogyi, P. (1994). Diverse sources of hippocampal unitary inhibitory postsynaptic potentials and the number of synaptic release sites. *Nature*, 368(6474):823–828.

Buzsáki, G. (1986). Hippocampal sharp waves: their origin and significance. *Brain research*, 398(2):242–252.

Buzsáki, G. (1989). Two-stage model of memory trace formation: a role for "noisy" brain states. *Neuroscience*, 31(3):551–570.

Buzsáki, G. (1996). The hippocampo-neocortical dialogue. *Cerebral cortex (New York, N.Y. : 1991)*, 6(2):81–92.

Buzsáki, G. and Draguhn, A. (2004). Neuronal oscillations in cortical networks. *Science (New York, N.Y.)*, 304(5679):1926–1929.

Buzsáki, G., Horváth, Z., Urioste, R., Hetke, J., and Wise, K. (1992). High-frequency network oscillation in the hippocampus. *Science (New York, N.Y.)*, 256(5059):1025–1027.

Chevaleyre, V. and Siegelbaum, S. A. (2010). Strong CA2 pyramidal neuron synapses define a powerful disynaptic cortico-hippocampal loop. *Neuron*, 66(4):560–572.

Chittajallu, R., Craig, M. T., McFarland, A., Yuan, X., Gerfen, S., Tricoire, L., Erkkila, B., Barron, S. C., Lopez, C. M., Liang, B. J., Jeffries, B. W., Pelkey, K. A., and McBain, C. J. (2013). Dual origins of functionally distinct O-LM interneurons revealed by differential 5-HT3AR expression. *Nature neuroscience*.

Chow, B. Y., Han, X., Dobry, A. S., Qian, X., Chuong, A. S., Li, M., Henninger, M. A., Belfort, G. M., Lin, Y., Monahan, P. E., and Boyden, E. S. (2010). High-performance genetically targetable optical neural silencing by light-driven proton pumps. *Nature*, 463(7277):98–102.

Chrobak, J. J. and Buzsáki, G. (1994). Selective activation of deep layer (V-VI) retrohippocampal cortical neurons during hippocampal sharp waves in the behaving rat. *The Journal of neuroscience : the official journal of the Society for Neuroscience*, 14(10):6160–6170.

Cobb, S. R., Buhl, E. H., Halasy, K., Paulsen, O., and Somogyi, P. (1995). Synchronization of neuronal activity in hippocampus by individual GABAergic interneurons. *Nature*, 378(6552):75–78.

Csicsvari, J., Hirase, H., Czurkó, A., Mamiya, A., and Buzsáki, G. (1999). Oscillatory coupling of hippocampal pyramidal cells and interneurons in the behaving Rat. *The Journal of neuroscience : the official journal of the Society for Neuroscience*, 19(1):274–287.

Csicsvari, J., Hirase, H., Mamiya, A., and Buzsáki, G. (2000). Ensemble patterns of hippocampal CA3-CA1 neurons during sharp wave-associated population events. *Neuron*, 28(2):585–594.

Csicsvari, J., Jamieson, B., Wise, K. D., and Buzsáki, G. (2003). Mechanisms of gamma oscillations in the hippocampus of the behaving rat. *Neuron*, 37(2):311–322.

Cui, Z., Gerfen, C. R., and Young, W. S. (2013). Hypothalamic and other connections with dorsal CA2 area of the mouse hippocampus. *The Journal of comparative neurology*, 521(8):1844–1866.

Diba, K. and Buzsáki, G. (2007). Forward and reverse hippocampal place-cell sequences during ripples. *Nature neuroscience*, 10(10):1241–1242.

Draguhn, A., Traub, R. D., Schmitz, D., and Jefferys, J. G. (1998). Electrical coupling underlies high-frequency oscillations in the hippocampus in vitro. *Nature*, 394(6689):189–192.

Dugladze, T., Schmitz, D., Whittington, M. A., Vida, I., and Gloveli, T. (2012). Segregation of axonal and somatic activity during fast network oscillations. *Science (New York, N.Y.)*, 336(6087):1458–1461.

Ego-Stengel, V. and Wilson, M. A. (2010). Disruption of ripple-associated hippocampal activity during rest impairs spatial learning in the rat. *Hippocampus*, 20(1):1–10.

Elfant, D., Pál, B. Z., Emptage, N., and Capogna, M. (2008). Specific inhibitory synapses shift the balance from feedforward to feedback inhibition of hippocampal CA1 pyramidal cells. *The European journal of neuroscience*, 27(1):104–113.

Empson, R. M. and Heinemann, U. (1995). The perforant path projection to hippocampal area CA1 in the rat hippocampal-entorhinal cortex combined slice. *The Journal of physiology*, 484 (Pt 3):707–720.

Eschenko, O., Ramadan, W., Mölle, M., Born, J., and Sara, S. J. (2008). Sustained increase in hippocampal sharp-wave ripple activity during slow-wave sleep after learning. *Learning & memory (Cold Spring Harbor, N.Y.)*, 15(4):222–228.

Forro, T., Valenti, O., Lasztoczi, B., and Klausberger, T. (2013). Temporal Organization of GABAergic Interneurons in the Intermediate CA1 Hippocampus During Network Oscillations. *Cerebral cortex (New York, N.Y. : 1991)*.

Foster, D. J. and Wilson, M. A. (2006). Reverse replay of behavioural sequences in hippocampal place cells during the awake state. *Nature*, 440(7084):680–683.

Freund, T. F. (2003). Interneuron Diversity series: Rhythm and mood in perisomatic inhibition. *Trends in neurosciences*, 26(9):489–495.

Freund, T. F. and Buzsáki, G. (1996). Interneurons of the hippocampus. *Hippocampus*, 6(4):347–470.

Freund, T. F. and Katona, I. (2007). Perisomatic inhibition. *Neuron*, 56(1):33–42.

Fuentealba, P., Begum, R., Capogna, M., Jinno, S., Marton, L. F., Csicsvari, J., Thomson, A., Somogyi, P., and Klausberger, T. (2008). Ivy cells: a population of nitric-oxide-producing, slow-spiking GABAergic neurons and their involvement in hippocampal network activity. *Neuron*, 57(6):917–929.

Girardeau, G., Benchenane, K., Wiener, S. I., Buzsáki, G., and Zugaro, M. B. (2009). Selective suppression of hippocampal ripples impairs spatial memory. *Nature neuroscience*, 12(10):1222–1223.

Glickfeld, L. L. and Scanziani, M. (2006). Distinct timing in the activity of cannabinoid-sensitive and cannabinoid-insensitive basket cells. *Nature neuroscience*, 9(6):807–815.

Gulyás, A. I., Görcs, T. J., and Freund, T. F. (1990). Innervation of different peptide-containing neurons in the hippocampus by GABAergic septal afferents. *Neuroscience*, 37(1):31–44.

Gulyás, A. I., Szabó, G. G., Ulbert, I., Holderith, N., Monyer, H., Erdélyi, F., Szabó, G., Freund, T. F., and Hájos, N. (2010). Parvalbumin-containing fast-spiking basket cells generate the field potential oscillations induced by cholinergic receptor activation in the hippocampus. *Journal of Neuroscience*, 30(45):15134–15145.

Haglund, L., Swanson, L. W., and Köhler, C. (1984). The projection of the supramammillary nucleus to the hippocampal formation: an immunohistochemical and anterograde transport study with the lectin PHA-L in the rat. *The Journal of comparative neurology*, 229(2):171–185.

Hájos, N., Pálhalmi, J., Mann, E. O., Németh, B., Paulsen, O., and Freund, T. F. (2004). Spike timing of distinct types of GABAergic interneuron during hippocampal gamma oscillations in vitro. *The Journal of neuroscience : the official journal of the Society for Neuroscience*, 24(41):9127–9137.

Henriksen, E. J., Colgin, L. L., Barnes, C. A., Witter, M. P., Moser, M.-B., and Moser, E. I. (2010). Spatial representation along the proximodistal axis of CA1. *Neuron*, 68(1):127–137.

Hitti, F. L. and Siegelbaum, S. A. (2014). The hippocampal CA2 region is essential for social memory. *Nature*, pages –.

Ishizuka, N., Cowan, W. M., and Amaral, D. G. (1995). A quantitative analysis of the dendritic organization of pyramidal cells in the rat hippocampus. *The Journal of comparative neurology*, 362(1):17–45.

Jadhav, S. P., Kemere, C., German, P. W., and Frank, L. M. (2012). Awake hippocampal sharp-wave ripples support spatial memory. *Science (New York, N.Y.)*, 336(6087):1454–1458.

Jarsky, T., Mady, R., Kennedy, B., and Spruston, N. (2008). Distribution of bursting neurons in the CA1 region and the subiculum of the rat hippocampus. *The Journal of comparative neurology*, 506(4):535–547.

Jinno, S., Klausberger, T., Marton, L. F., Dalezios, Y., Roberts, J. D. B., Fuentealba, P., Bushong, E. A., Henze, D., Buzsáki, G., and Somogyi, P. (2007). Neuronal diversity in GABAergic long-range projections from the hippocampus. *The Journal of neuroscience : the official journal of the Society for Neuroscience*, 27(33):8790–8804.

Jones, M. W. and McHugh, T. J. (2011). Updating hippocampal representations: CA2 joins the circuit. *Trends in neurosciences*, 34(10):526–535.

Katona, I., Acsády, L., and Freund, T. F. (1999). Postsynaptic targets of somatostatin-immunoreactive interneurons in the rat hippocampus. *Neuroscience*, 88(1):37–55.

Klausberger, T., Magill, P. J., Marton, L. F., Roberts, J. D. B., Cobden, P. M., Buzsáki, G., and Somogyi, P. (2003). Brain-state- and cell-type-specific firing of hippocampal interneurons in vivo. *Nature*, 421(6925):844–848.

Klausberger, T., Marton, L. F., Baude, A., Roberts, J. D. B., Magill, P. J., and Somogyi, P. (2004). Spike timing of dendrite-targeting bistratified cells during hippocampal network oscillations in vivo. *Nature neuroscience*, 7(1):41–47.

Klausberger, T., Marton, L. F., O'Neill, J., Huck, J. H. J., Dalezios, Y., Fuentealba, P., Suen, W. Y., Papp, E., Kaneko, T., Watanabe, M., Csicsvari, J., and Somogyi, P. (2005). Complementary roles of cholecystokinin- and parvalbumin-expressing GABAergic neurons in hippocampal network oscillations. *The Journal of neuroscience : the official journal of the Society for Neuroscience*, 25(42):9782–9793.

Klausberger, T. and Somogyi, P. (2008). Neuronal diversity and temporal dynamics: the unity of hippocampal circuit operations. *Science (New York, N.Y.)*, 321(5885):53–57.

Kogo, N., Dalezios, Y., Capogna, M., Ferraguti, F., Shigemoto, R., and Somogyi, P. (2004). Depression of GABAergic input to identified hippocampal neurons by group III metabotropic glutamate receptors in the rat. *The European journal of neuroscience*, 19(10):2727–2740.

Kohara, K., Pignatelli, M., Rivest, A. J., Jung, H.-Y., Kitamura, T., Suh, J., Frank, D., Kajikawa, K., Mise, N., Obata, Y., Wickersham, I. R., and Tonegawa, S. (2014). Cell type-specific genetic and optogenetic tools reveal hippocampal CA2 circuits. *Nature neuroscience*, 17(2):269–279.

Lansink, C. S., Goltstein, P. M., Lankelma, J. V., McNaughton, B. L., and Pennartz, C. M. A. (2009). Hippocampus leads ventral striatum in replay of place-reward information. *PLoS biology*, 7(8):e1000173.

Lapray, D., Lasztoczi, B., Lagler, M., Viney, T. J., Katona, L., Valenti, O., Hartwich, K., Borhegyi, Z., Somogyi, P., and Klausberger, T. (2012). Behavior-dependent specialization of identified hippocampal interneurons. *Nature neuroscience*, 15(9):1265–1271.

Leão, R. N., Mikulovic, S., Leão, K. E., Munguba, H., Gezelius, H., Enjin, A., Patra, K., Eriksson, A., Loew, L. M., Tort, A. B. L., and Kullander, K. (2012). OLM interneurons differentially modulate CA3 and entorhinal inputs to hippocampal CA1 neurons. *Nature neuroscience*, 15(11):1524–1530.

Lee, A. K. and Wilson, M. A. (2002). Memory of sequential experience in the hippocampus during slow wave sleep. *Neuron*, 36(6):1183–1194.

Lee, S. E., Simons, S. B., Heldt, S. A., Zhao, M., Schroeder, J. P., Vellano, C. P., Cowan, D. P., Ramineni, S., Yates, C. K., Feng, Y., Smith, Y., Sweatt, J. D., Weinshenker, D., Ressler, K. J., Dudek, S. M., and Hepler, J. R. (2010). RGS14 is a natural suppressor of both synaptic plasticity in CA2 neurons and hippocampal-based learning and memory. *Proceedings of the National Academy of Sciences of the United States of America*, 107(39):16994–16998.

Lee, S.-H., Marchionni, I., Bezaire, M., Varga, C., Danielson, N., Lovett-Barron, M., Losonczy, A., and Soltesz, I. (2014). Parvalbumin-Positive Basket Cells Differentiate among Hippocampal Pyramidal Cells. *Neuron*.

Lein, E. S., Callaway, E. M., Albright, T. D., and Gage, F. H. (2005). Redefining the boundaries of the hippocampal CA2 subfield in the mouse using gene expression and 3-dimensional reconstruction. *The Journal of comparative neurology*, 485(1):1–10.

Llorens-Martín, M., Jurado-Arjona, J., Avila, J., and Hernández, F. (2015). Novel connection between newborn granule neurons and the hippocampal CA2 field. *Experimental neurology*, 263:285–292.

Lorente de Nó, R. (1934). Studies on the structure of the cerebral cortex. II. Continuation of the study of the ammonic system. *J Psychol Neurol*, 34:113–177.

Losonczy, A., Somogyi, P., and Nusser, Z. (2003). Reduction of excitatory postsynaptic responses by persistently active metabotropic glutamate receptors in the hippocampus. *Journal of neurophysiology*, 89(4):1910–1919.

Losonczy, A., Zhang, L., Shigemoto, R., Somogyi, P., and Nusser, Z. (2002). Cell type dependence and variability in the short-term plasticity of EPSCs in identified mouse hippocampal interneurones. *The Journal of physiology*, 542(Pt 1):193–210.

Maccaferri, G. (2005). Stratum oriens horizontal interneurone diversity and hippocampal network dynamics. *The Journal of physiology*, 562(Pt 1):73–80.

Maccaferri, G. and Dingledine, R. (2002). Control of feedforward dendritic inhibition by NMDA receptor-dependent spike timing in hippocampal interneurons. *Journal of Neuroscience*, 22(13):5462–5472.

Maccaferri, G. and McBain, C. J. (1996). Long-term potentiation in distinct subtypes of hippocampal nonpyramidal neurons. *The Journal of neuroscience : the official journal of the Society for Neuroscience*, 16(17):5334–5343.

Maccaferri, G., Roberts, J. D., Szucs, P., Cottingham, C. A., and Somogyi, P. (2000). Cell surface domain specific postsynaptic currents evoked by identified GABAergic neurones in rat hippocampus in vitro. *The Journal of physiology*, 524 Pt 1:91–116.

Maglóczky, Z., Acsády, L., and Freund, T. F. (1994). Principal cells are the postsynaptic targets of supramammillary afferents in the hippocampus of the rat. *Hippocampus*, 4(3):322–334.

Maier, N., Morris, G., Johenning, F. W., and Schmitz, D. (2009). An approach for reliably investigating hippocampal sharp wave-ripples in vitro. *PloS one*, 4(9):e6925.

Maier, N., Tejero-Cantero, A., Dorrn, A. L., Winterer, J., Beed, P. S., Morris, G., Kempter, R., Poulet, J. F. A., Leibold, C., and Schmitz, D. (2011). Coherent phasic excitation during hippocampal ripples. *Neuron*, 72(1):137–152.

Martina, M., Vida, I., and Jonas, P. (2000). Distal initiation and active propagation of action potentials in interneuron dendrites. *Science (New York, N.Y.)*, 287(5451):295–300.

McBain, C. J., DiChiara, T. J., and Kauer, J. A. (1994). Activation of metabotropic glutamate receptors differentially affects two classes of hippocampal interneurons and potentiates excitatory synaptic transmission. *The Journal of neuroscience : the official journal of the Society for Neuroscience*, 14(7):4433–4445.

Memmesheimer, R.-M. (2010). Quantitative prediction of intermittent high-frequency oscillations in neural networks with supralinear dendritic interactions. *Proceedings of the National Academy of Sciences*, 107(24):11092–11097.

Mercer, A., Botcher, N. A., Eastlake, K., and Thomson, A. M. (2012a). SP-SR interneurones: a novel class of neurones of the CA2 region of the hippocampus. *Hippocampus*, 22(8):1758–1769.

Mercer, A., Eastlake, K., Trigg, H. L., and Thomson, A. M. (2012b). Local circuitry involving parvalbumin-positive basket cells in the CA2 region of the hippocampus. *Hippocampus*, 22(1):43–56.

Mercer, A., Trigg, H. L., and Thomson, A. M. (2007). Characterization of neurons in the CA2 subfield of the adult rat hippocampus. *The Journal of neuroscience : the official journal of the Society for Neuroscience*, 27(27):7329–7338.

Mizuseki, K., Diba, K., Pastalkova, E., and Buzsáki, G. (2011). Hippocampal CA1 pyramidal cells form functionally distinct sublayers. *Nature neuroscience*, 14(9):1174–1181.

Müller, A., Kukley, M., Stausberg, P., Beck, H., Müller, W., and Dietrich, D. (2005). Endogenous Ca2+ buffer concentration and Ca2+ microdomains in hippocampal neurons. *Journal of Neuroscience*, 25(3):558–565.

Nagel, G., Szellas, T., Huhn, W., Kateriya, S., Adeishvili, N., Berthold, P., Ollig, D., Hegemann, P., and Bamberg, E. (2003). Channelrhodopsin-2, a directly light-gated cation-selective membrane channel. *Proceedings of the National Academy of Sciences of the United States of America*, 100(24):13940–13945.

Ochiishi, T., Saitoh, Y., Yukawa, A., Saji, M., Ren, Y., Shirao, T., Miyamoto, H., Nakata, H., and Sekino, Y. (1999). High level of adenosine A1 receptor-like immunoreactivity in the CA2/CA3a region of the adult rat hippocampus. *Neuroscience*, 93(3):955–967.

O'Keefe, J. (1976). Place units in the hippocampus of the freely moving rat. *Experimental neurology*, 51(1):78–109.

O'Neill, J., Pleydell-Bouverie, B., Dupret, D., and Csicsvari, J. (2010). Play it again: reactivation of waking experience and memory. *Trends in neurosciences*, 33(5):220–229.

Oren, I., Mann, E. O., Paulsen, O., and Hájos, N. (2006). Synaptic currents in anatomically identified CA3 neurons during hippocampal gamma oscillations in vitro. *The Journal of neuroscience : the official journal of the Society for Neuroscience*, 26(39):9923–9934.

Pangalos, M., Donoso, J. R., Winterer, J., Zivkovic, A. R., Kempter, R., Maier, N., and Schmitz, D. (2013). Recruitment of oriens-lacunosum-moleculare interneurons during hippocampal ripples. *Proceedings of the National Academy of Sciences*.

Pennartz, C. M. A., Lee, E., Verheul, J., Lipa, P., Barnes, C. A., and McNaughton, B. L. (2004). The ventral striatum in off-line processing: ensemble reactivation during sleep and modulation by hippocampal ripples. *Journal of Neuroscience*, 24(29):6446–6456.

Peyrache, A., Khamassi, M., Benchenane, K., Wiener, S. I., and Battaglia, F. P. (2009). Replay of rule-learning related neural patterns in the prefrontal cortex during sleep. *Nature neuroscience*, 12(7):919–926.

Phillips, T., Makoff, A., Brown, S., Rees, S., and Emson, P. (1997). Localization of mGluR4 protein in the rat cerebral cortex and hippocampus. *Neuroreport*, 8(15):3349–3354.

Piskorowski, R. A. and Chevaleyre, V. (2012). Synaptic integration by different dendritic compartments of hippocampal CA1 and CA2 pyramidal neurons. *Cellular and molecular life sciences : CMLS*, 69(1):75–88.

Ponomarenko, A. A., Li, J.-S., Korotkova, T. M., Huston, J. P., and Haas, H. L. (2008). Frequency of network synchronization in the hippocampus marks learning. *The European journal of neuroscience*, 27(11):3035–3042.

Pouille, F. and Scanziani, M. (2001). Enforcement of temporal fidelity in pyramidal cells by somatic feed-forward inhibition. *Science (New York, N.Y.)*, 293(5532):1159–1163.

Ramadan, W., Eschenko, O., and Sara, S. J. (2009). Hippocampal sharp wave/ripples during sleep for consolidation of associative memory. *PloS one*, 4(8):e6697.

Rowland, D. C., Weible, A. P., Wickersham, I. R., Wu, H., Mayford, M., Witter, M. P., and Kentros, C. G. (2013). Transgenically targeted rabies virus demonstrates a major monosynaptic projection from hippocampal area CA2 to medial entorhinal layer II neurons. *Journal of Neuroscience*, 33(37):14889–14898.

Royer, S., Zemelman, B. V., Losonczy, A., Kim, J., Chance, F., Magee, J. C., and Buzsáki, G. (2012). Control of timing, rate and bursts of hippocampal place cells by dendritic and somatic inhibition. *Nature neuroscience*, 15(5):769–775.

San Antonio, A., Liban, K., Ikrar, T., Tsyganovskiy, E., and Xu, X. (2014). Distinct physiological and developmental properties of hippocampal CA2 subfield revealed by using anti-Purkinje cell protein 4 (PCP4) immunostaining. *The Journal of comparative neurology*, 522(6):1333–1354.

Schlingloff, D., Káli, S., Freund, T. F., Hájos, N., and Gulyás, A. I. (2014). Mechanisms of sharp wave initiation and ripple generation. *Journal of Neuroscience*, 34(34):11385–11398.

Senior, T. J., Huxter, J. R., Allen, K., O'Neill, J., and Csicsvari, J. (2008). Gamma oscillatory firing reveals distinct populations of pyramidal cells in the CA1 region of the hippocampus. *Journal of Neuroscience*, 28(9):2274–2286.

Shigemoto, R., Kulik, A., Roberts, J. D., Ohishi, H., Nusser, Z., Kaneko, T., and Somogyi, P. (1996). Target-cell-specific concentration of a metabotropic glutamate receptor in the presynaptic active zone. *Nature*, 381(6582):523–525.

Sik, A., Penttonen, M., Ylinen, A., and Buzsáki, G. (1995). Hippocampal CA1 interneurons: an in vivo intracellular labeling study. *The Journal of neuroscience : the official journal of the Society for Neuroscience*, 15(10):6651–6665.

Simons, S. B., Caruana, D. A., Zhao, M., and Dudek, S. M. (2012). Caffeine-induced synaptic potentiation in hippocampal CA2 neurons. *Nature neuroscience*, 15(1):23–25.

Somogyi, P., Freund, T. F., Hodgson, A. J., Somogyi, J., Beroukas, D., and Chubb, I. W. (1985). Identified axo-axonic cells are immunoreactive for GABA in the hippocampus and visual cortex of the cat. *Brain research*, 332(1):143–149.

Sun, Q., Srinivas, K. V., Sotayo, A., and Siegelbaum, S. A. (2014). Dendritic Na(+) spikes enable cortical input to drive action potential output from hippocampal CA2 pyramidal neurons. *eLife*, 3.

Tamamaki, N. and Nojyo, Y. (1995). Preservation of topography in the connections between the subiculum, field CA1, and the entorhinal cortex in rats. *The Journal of comparative neurology*, 353(3):379–390.

Tamás, G., Buhl, E. H., Lörincz, A., and Somogyi, P. (2000). Proximally targeted GABAergic synapses and gap junctions synchronize cortical interneurons. *Nature neuroscience*, 3(4):366–371.

Taxidis, J., Coombes, S., Mason, R., and Owen, M. R. (2012). Modeling sharp wave-ripple complexes through a CA3-CA1 network model with chemical synapses. *Hippocampus*, 22(5):995–1017.

Traub, R. D., Schmitz, D., Jefferys, J. G., and Draguhn, A. (1999). High-frequency population oscillations are predicted to occur in hippocampal pyramidal neuronal networks interconnected by axoaxonal gap junctions. *Neuroscience*, 92(2):407–426.

Traub, R. D., Schmitz, D., Maier, N., Whittington, M. A., and Draguhn, A. (2012). Axonal properties determine somatic firing in a model of in vitro CA1 hippocampal sharp wave/ripples and persistent gamma oscillations. *The European journal of neuroscience*, 36(5):2650–2660.

Tucker, M. S., Khan, I., Fuchs-Young, R., Price, S., Steininger, T. L., Greene, G., Wainer, B. H., and Rosner, M. R. (1993). Localization of immunoreactive epidermal growth factor receptor in neonatal and adult rat hippocampus. *Brain research*, 631(1):65–71.

Vanderwolf, C. H. (1969). Hippocampal electrical activity and voluntary movement in the rat. *Electroencephalography and clinical neurophysiology*, 26(4):407–418.

Varga, C., Golshani, P., and Soltesz, I. (2012). Frequency-invariant temporal ordering of interneuronal discharges during hippocampal oscillations in awake mice. *Proceedings of the National Academy of Sciences*, 109(40):E2726–34.

Vida, I. and Frotscher, M. (2000). A hippocampal interneuron associated with the mossy fiber system. *Proceedings of the National Academy of Sciences of the United States of America*, 97(3):1275–1280.

Viney, T. J., Lasztoczi, B., Katona, L., Crump, M. G., Tukker, J. J., Klausberger, T., and Somogyi, P. (2013). Network state-dependent inhibition of identified hippocampal CA3 axo-axonic cells in vivo. *Nature neuroscience*.

Wilson, M. A. and McNaughton, B. L. (1994). Reactivation of hippocampal ensemble memories during sleep. *Science (New York, N.Y.)*, 265(5172):676–679.

Wulff, P., Ponomarenko, A. A., Bartos, M., Korotkova, T. M., Fuchs, E. C., Bähner, F., Both, M., Tort, A. B. L., Kopell, N. J., Wisden, W., and Monyer, H. (2009). Hippocampal theta rhythm and its coupling with gamma oscillations require fast inhibition onto parvalbumin-positive interneurons. *Proceedings of the National Academy of Sciences*, 106(9):3561–3566.

Wyszynski, M., Kharazia, V., Shanghvi, R., Rao, A., Beggs, A. H., Craig, A. M., Weinberg, R., and Sheng, M. (1998). Differential regional expression and ultrastructural localization of alpha-actinin-2, a putative NMDA receptor-anchoring protein, in rat brain. *The Journal of neuroscience : the official journal of the Society for Neuroscience*, 18(4):1383–1392.

Ylinen, A., Bragin, A., Nádasdy, Z., Jandó, G., Szabó, I., Sik, A., and Buzsáki, G. (1995). Sharp wave-associated high-frequency oscillation (200 Hz) in the intact hippocampus: network and intracellular mechanisms. *The Journal of neuroscience : the official journal of the Society for Neuroscience*, 15(1 Pt 1):30–46.

Young, W. S., Li, J., Wersinger, S. R., and Palkovits, M. (2006). The vasopressin 1b receptor is prominent in the hippocampal area CA2 where it is unaffected by restraint stress or adrenalectomy. *Neuroscience*, 143(4):1031–1039.

Zhao, M., Choi, Y.-S., Obrietan, K., and Dudek, S. M. (2007). Synaptic plasticity (and the lack thereof) in hippocampal CA2 neurons. *The Journal of neuroscience : the official journal of the Society for Neuroscience*, 27(44):12025–12032.

Appendix A

Statement of contribution

The projects discussed in this thesis have been conducted in a collaborative approach. In the following, I will state the respective contributions to the data presented.

Contribution: Chapter 2

The experiments were designed by me, Nikolaus Maier and Dietmar Schmitz. I have performed the majority of experiments presented in this Chapter. The experiments summarized in Figure 2.1 and Figure 2.2 were performed by Nikolaus Maier only and also some of the other experiments (3 of 27 datasets in Figure 2.3, 1 of 7 datasets in Figure 2.4, 1 of 13 datasets in Figure 2.5, 1 of 18 datasets in Figure 2.6 B, 1 of 7 datasets in Figure 2.6 C2 and D and 1 of 22 datasets in Figure 2.7, 2.8, 2.9 and 2.10) in this Chapter were performed by him. I have analyzed the majority of data using self-made code in Matlab. Nikolaus Maier also analyzed some of the data (Figure 2.1 and Figure 2.2). José R. Donoso and Richard Kempter developed all tools to analyze phase relationships and José R. Donoso performed the phase analysis and also the analysis of the input resistance (Figure 2.3, Figure 2.4, Figure 2.5, Figure 2.6, Figure 2.7 (C)).

Own contribution: 80%.

Contribution: Chapter 3

Anja Gundlfinger, Nikolaus Maier, Dietmar Schmitz and I designed and performed the experiments presented in this Chapter. Anja Gundlfinger and I analyzed the data. The immunocytochemistry was performed by Susanne Rieckmann and Anja Gundlfinger.

Own contribution: 50%.

Contribution: Chapter 4

Anja Gundlfinger, Nikolaus Maier, Dietmar Schmitz and I designed the experiments in this Chapter. Anja Gundlfinger and I performed the experiments. I did the majority of data analysis and also Anja Gundlfinger did some of the analysis. The immunocytochemistry was performed by Susanne Rieckmann and Anja Gundlfinger.

Own contribution: 65%.

Appendix B

Curriculum Vitae

Mein Lebenslauf wird aus datenschutzrechtlichen Gründen in der elektronischen Version meiner Arbeit nicht veröffentlicht.

Appendix C

Publications

Journal publication

Grauel MK*, Reddy S*, Maglione M, Brockmann MM, Bentz CG, Trimbuch T, Abo-Rady M, Rosenmund T, **Pangalos M**, Rost BR, Eickholt B, Haucke V, Schmitz D, Sigrist S and Rosenmund C. (2016): RIM-binding protein 2 is a regulator of short-term plasticity at mammalian glutamatergic synapses. Submitted

Gundlfinger G*, **Pangalos M***, Maier N, Schmitz D. (2016): Analysis of synaptic inputs in pyramidal neurons in area CA2 during SWRs. In preparation

Böhm C, **Pangalos M**, Schmitz D, Winterer J. (2015): Serotonin Attenuates Feedback Excitation onto O-LM Interneurons. Cereb Cortex. doi:10.1093/cercor/bhv098.

Pangalos M, Donoso JR, Winterer J, Zivkovic AR, Kempter R, Maier N*, Schmitz D* (2013): Recruitment of oriens-lacunosum-moleculare interneurons during hippocampal ripples. Proc Natl Acad Sci U S A. 110(11):4398-4403.

Günzel D, Zakrzewski S, Schmid T, **Pangalos M**, Wiedenhoeft J, Blasse C, Ozboda C, Krug SM (2012): From TER to trans- and paracellular resistance: Lessons from impedance spectroscopy. Ann N Y Acad Sci. 1257:142-151.

Bintig W, Begandt D, Schlingmann B, Gerhard L, **Pangalos M**, Dreyer L, Hohnjec N, Couraud JP, Romera AI, Weksler B, Ngezahayo A (2012): Purinergic receptors and Ca2+ signalling in the human blood-brain barrier endothelial cell line hCMEC/D3. Purinergic Signal. 8(1):71-80.

Pangalos M, Bintig W, Schlingmann B, Feyerabend F, Witte F, Begandt D, Heisterkamp A, Ngezahayo A (2011): Action potentials in primary osteoblasts and osteoblast like cell line MG 63. J Bioenerg Biomembr. 2011 43(3):311-322.

Conference contribution

Pangalos M, Donoso JR, Winterer J, Zivkovic AR, Kempter R, Maier N, Schmitz D: Investigation into O-LM cell recruitment during hippocampal ripples in vitro. (Poster, Neural Networks and Rhythm Generators, NWG Göttingen, March 2013).

Pangalos M, Bintig W, Dreyer L, Ngezahayo A: Action potentials in osteoblasts. (Oral Presentations, Ion channels I, DPG Regensburg, March 2011).

Appendix D

Deutsche Zusammenfassung

Im Hippokampus gibt es verschiedene Aktivitätsmuster, auch Netzwerkoszillationen genannt, mit unterschiedlichen Frequenzen, die an bestimmte Verhaltenszustände gekoppelt sind. Ein Typ dieser Netzwerkszillationen, die "Ripple" treten im Ruhezustand und im Tiefschlaf auf. Sie haben eine Frequenz von etwa 200 Hz und treten in Komplexen mit einer den ripple unterliegenden Aktivitätswelle, der "Sharp wave" auf. Sharp wave-ripple Komplexe (SWR) werden mit der Konsolidierung von Gedächtnis in Zusammenhang gebracht. Das Netzwerk, das den SWR unterliegt, hat bestimmte Mechanismen, von denen einige in der vorliegenden Arbeit näher untersucht werden.

Im ersten Teil der Arbeit (Kapitel 2 Recruitment of oriens-lacunosum moleculare interneurons during hippocampal ripples) wird untersucht, wie ein bestimmtes hemmendes Interneuron in der hippokampalen Region CA1, das "oriens-lacunosum moleculare" (O-LM) Interneuron, während der SWR in das Netzwerk eingebunden ist. Wir konnten zeigen, dass O-LM Interneurone während der SWR starke synaptische Exzitation erhalten. Die Exzitation tritt erst spät während des Ripples auf, der im lokalen Feldpotential gemessen wurde, und zeigt eine Ankopplung an die aufsteigende Phase der Ripple-Oszillation. In etwa der Hälfte der O-LM Interneurone konnten wir Aktionspotentiale während der SWR und damit eine aktive Beteiligung dieser Zellen an der Oszillation zeigen. Wie die Exzitation, sind auch die Aktionspotentiale an die Ripple-Phase im lokalen Feldpotential gebunden und treten erst nach dem Ripple-Maximum auf, spät während des Ripples.

Im zweiten und auch im dritten Teil dieser Arbeit untersuchen wir den synaptischen Eingang in exzitatorische Pyramidenzellen während Ripple-Oszillationen Kapitel 3 (Comparison of synaptic input in deep and superficial CA1 pyramidal cells during ripple oscillations) bezieht sich auf die hippokampale Region CA1 und vergleicht während SWR den synaptischen Eingang in zwei Untertypen von Pyramidenzellen, den tiefen, näher zum Stratum oriens und den oberflächlich, näher zum Stratum radiatum gelegenen Pyramidenzellen. Sowohl die tiefen, als auch die oberflächlichen Pyramidenzellen bekommen synaptische Eingänge während der SWR. Diese Eingänge sind eine Mischung aus exzitatorischen und inhibitorischen

Eingängen. In den von uns untersuchten Zellen beider Untertypen waren sowohl die inhibitorischen als auch exzitatiorischen synaptischen Eingänge in ihrer Stärke vergleichbar.

In Kapitel 4 (Analysis of synaptic inputs in pyramidal neurons in area CA2 during SWRs) untersuchen wir die Sharp wave-ripple Komplexe in der Region CA2 des Hippokampus und zeigen, dass Pyramidenzellen in CA2 in das Netzwerk während SWR eingebunden sind. Wir können sowohl exzitatorische als auch inhibitorische synaptische Eingänge in den Pyramidenzellen darstellen. In weitergehenden Analysen dieser Eingänge, konnten wir eine Phasenkopplung der synaptischen Eingänge an die SWR im lokalen Feldpotential zeigen. Die Phase der Eingänge ist an die aufsteigende Phase der Feld-Ripples gekoppelt. Aufgrund der Phasenverschiebung bei verschiedenen Haltepotentialen vermuten wir einen Oszillator für die Exzitation und einen für die Hemmung.

Acknowledgements

Diese Doktorarbeit wurde wesentlich durch ein produktives Klima im Schmitzlab unterstützt, das die Kooperation mit anderen Gruppen und die Zusammenarbeit und Beratung aller Kollegen fördert und von dem ich sehr profitiert habe.

Zunächst möchte ich Prof. Dr. Dietmar Schmitz danken, der mir die Möglichkeit gab, in seinem Labor zu forschen. Bei allen Freiheiten, die ich bei meinen Forschungsprojekten hatte, konnte ich immer auf seinen Rat und seine Unterstützung zurückgreifen.

Ganz besonders danke ich meinem Mentor Dr. Nikolaus Maier, der mich während meiner Doktorarbeit mit sehr viel Energie, wissenschaftlicher Erfahrung, Zeit und Geduld betreut hat. Er hat mir sowohl die elektrophysiologischen Techniken beigebracht, als auch mit mir die wissenschaftlichen Zusammenhänge diskutiert. Ich danke ihm auch herzlich für das kritische lesen dieser Arbeit.

Ich danke Prof. Dr. Richard Kempter für die Betreuung meiner Doktorarbeit, die sehr lehrreiche Zusammenarbeit und seine immer währende Hilfsbereitschaft.

I would like to thank José Donoso for the fruitful and instructive collaboration on the O-LM project and for sharing his developed analysis tools with me.

Ich danke Prof. Dr. Nikolai Axmacher für seine spontane Zusage, das externe Gutachten zu übernehmen.

Besonders danken möchte ich auch Dr. Anja Gundlfinger für die enge Zusammenarbeit bei den Projekten bezüglich der CA1 und CA2 Pyramidenzellen. Es war großartig, immer wieder positiv gestimmt und motiviert zusammen zu experimentieren.

Den exzellenten technischen Assistentinnen Susanne Rieckmann, Anke Schönherr, Karin Bloch und Lisa Züchner möchte ich für ihre Hilfe und Unterstützung bei allen Labor-Problemen danken. Susanne Rieckmann danke ich besonders für die ruhige und gelassene Art mit der sie mir die Präparation und Färbung beigebracht hat.

And I would like to thank all members of the Schmitzlab for the very friendly, helpful and warm working atmosphere.

Und ganz zum Schluss möchte ich meiner kleinen und großen, lieben Familie danken.

Eidesstattliche Erklärung

Ich erkläre, dass ich die vorliegende Arbeit selbständig und nur unter Verwendung der angegebenen Literatur und Hilfsmittel angefertigt habe.

Berlin, March 29, 2016 Maria Pangalos